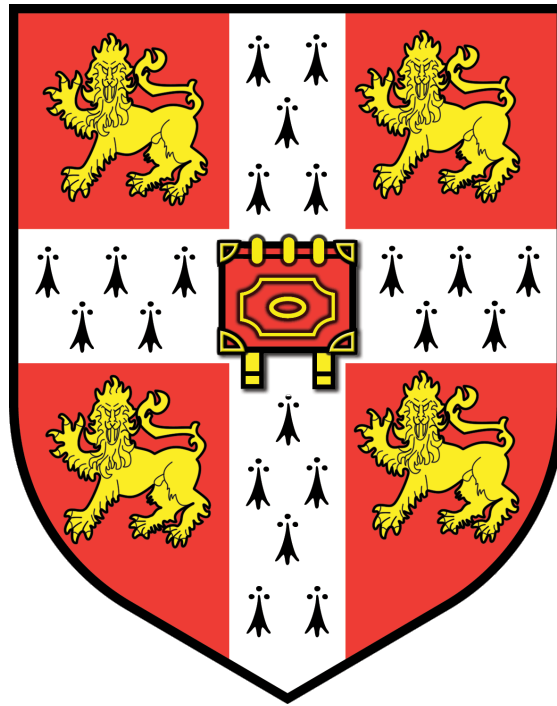


Superconductivity in the proximity of a quantum critical point



Peter Logg
Queens' College
University of Cambridge
Easter 2014

A thesis presented for the degree of
Doctor of Philosophy

Declaration

This dissertation is the result of my own work and includes nothing which is the outcome of work done in collaboration except where specifically indicated in the text and Acknowledgements. The total length of this dissertation does not exceed sixty thousand words.

Peter Logg

June 2014

Acknowledgments

The main portion of thanks for the completion of this thesis should be directed towards my supervisor, Dr F. Malte Grosche. His unswerving enthusiasm for the subject is very infectious, and his clarity of thought and description is - in my experience - unparalleled. I should also thank Swee K Goh and Patricia Alireza for their advice and assistance when I began the pressure work, and also to the late Sam Brown for his technical support when faced with bent pressure cells/pistons and so on. Thanks also to Dan Cross and Mariusz Naguszewski for keeping the magnetometer nice and cold for the last three and a half years, and Thomas Holubar and Jim Fowler at Cryogenic Ltd for help with the SQUID.

I should also extend my thanks to the many other members (and ex-members) of the Quantum Matter group, for either experimental help, or just chatting to me: Yang Zou, Pascal Reiß, Sven Friedemann, Hui Chang, Hong'En Tan, Beng Tan, Sitikantha Das, Phil Brown and everyone else who I have forgotten. Thanks also to my friend Anup Patel from the Applied Superconductivity group in the Department of Materials for answering all of my daft questions about type-II superconductors.

The majority of my time in Cambridge has been spent in Queens' college, a very happy place indeed. From Queens' I wish to extend my gratitude to all of the porters and the catering staff, along with Tim Cannings, Alec Plint, Gregor Stewart, Nick Töberg, Max Cooper, Sebastien Rivat, Ronnie O'Sullivan, David Bowie and the MCR pool table.

Finally, I should also like to thank Mark, Simon, Dom and Marnie for all of their brilliant help - none of this would have been possible without them.

Peter Logg

June 2014

Outline

In a many-body fermionic system, the suppression of continuous transitions to absolute zero can result in a low temperature quantum fluid which deviates strongly from typical metallic behaviour; unconventional superconductivity can be induced by the “strange metal” region surrounding the zero-temperature phase transition. In this thesis we focus on three systems which demonstrate a highly tunable phase transition, with the aim of pushing them toward the border of a zero-temperature phase transition, and potentially superconductivity.

CeAgSb₂ is a uniaxial 4*f* ferromagnet, where physical pressure or a transverse field may be used to tune the magnetic transition towards $T = 0$ K. Our investigations, however, did not reveal the presence of superconductivity. It is likely that the field tuned transition does not correspond to a “true” critical point, whilst the high pressure region may be occupied by an antiferromagnetic phase, with the true critical point at higher pressures. However, other interesting features emerge in the electrical resistivity and AC-susceptibility, along with novel thermodynamic signatures linking the magnetisation to the specific heat.

The doping series $Y_x\text{Lu}_{1-x}\text{Fe}_2\text{Ge}_2$ shows an antiferromagnetic transition which is suppressed to absolute zero at a critical concentration $x_c = 0.2$. YFe_2Ge_2 displays anomalous low temperature behaviour consistent with the proximity to quantum critical fluctuations, along with a superconducting transition which appears in the electrical resistivity beneath a critical temperature of $T_c \approx 1.7$ K. Using low temperature DC magnetisation measurements, we show that this is a bulk effect, and that the superconductivity in YFe_2Ge_2 is of type-II. The thermodynamic and BCS properties of the superconducting phase are analysed in line with the parameters we extract experimentally.

The superconducting 3-4-13 stannides $(\text{Ca},\text{Sr})_3\text{Ir}_4\text{Sn}_{13}$ show a high temperature structural transition which may be suppressed by the application of hydrostatic pressure or effective chemical pressure. A superconducting dome is found, which appears to peak near where the structural transition extrapolates to zero temperature. Anomalous exponents are seen in the electrical resistivity over a wide temperature range. We investigate the influence of pressure on the superconducting critical temperature in $\text{Ca}_3\text{Ir}_4\text{Sn}_{13}$ and the related compound $\text{Ca}_3\text{Co}_4\text{Sn}_{13}$, along with an analysis of the upper critical field and flux-line phenomena in $\text{Ca}_3\text{Ir}_4\text{Sn}_{13}$ and $\text{Sr}_3\text{Ir}_4\text{Sn}_{13}$.

Contents

1	Introduction	18
2	Theoretical Background	20
2.1	Phase transitions	20
2.1.1	Continuous and discontinuous phase transitions	20
2.1.2	Landau theory of the order parameter	24
2.2	Superconductivity	27
2.2.1	Overview	27
2.2.2	BCS result	28
2.2.3	Ginzburg-Landau theory	29
2.2.4	Critical fields and the superfluid density	31
2.2.5	Destruction of the superconducting state	33
2.3	Quantum Critical Superconductors	36
3	Experimental approach	42
3.1	DC magnetometry	43
3.1.1	S700X Susceptometer	43
3.1.2	Fitting the SQUID voltage	46
3.1.3	Sample mounting and background subtraction	48
3.1.4	³ He Insert	50
3.2	DMS	53
3.2.1	Adiabatic demagnetising refrigeration	53
3.3	Pressure	58
3.3.1	Miniature anvil cell	58

3.3.2	Manometry	62
4	CeAgSb₂	65
4.1	Ferromagnetism in a $4f$ system	65
4.2	Synthesis and characterisation	75
4.3	Pressure Tuning	77
4.4	Field Tuning	84
4.4.1	Transverse magnetisation	84
4.4.2	Resistivity	89
4.4.3	Transverse AC susceptibility	93
4.5	Discussion	99
5	YFe₂Ge₂	102
5.1	Fe-based superconductivity	102
5.2	Synthesis and characterisation	110
5.3	Diamagnetism in the magnetisation	115
5.3.1	Temperature dependence	115
5.3.2	Field dependence	122
5.3.3	Derived quantities	127
5.4	Discussion	129
6	R₃T₄Sn₁₃	136
6.1	Structural instability	136
6.2	Pressure dependence of T_c	143
6.2.1	Ca ₃ Co ₄ Sn ₁₃	143
6.2.2	Ca ₃ Ir ₄ Sn ₁₃	147
6.3	Upper critical field and the peak effect	150
6.4	Discussion	155
A	Determination of H_{c1}	158
A.1	$dM/dH \neq -1$	158
A.2	$\Delta M = H + M \neq 0$	159
A.3	$\sqrt{\Delta M}$ I.	159
A.4	$\sqrt{\Delta M}$ II.	159

B Pinning and irreversibility

162

List of Figures

2.1	Analytic properties of the derivatives of F at a phase transition. . .	21
2.2	First and second order antiferromagnetic transitions in MnS_2 and Pr_2I_5 , determined via neutron scattering.	23
2.3	Critical opalescence appearing in a methanol and cyclohexane mixture near its boiling point. (a) Single phase. (b) Onset of density fluctuations. (c) Critical opalescence.	24
2.4	(a) Form of the free energy $F(M)$ above and below the transition temperature. (b) Temperature dependence of the order parameter $M(T)$ given by the Landau theory.	25
2.5	Magnetic isotherms for superconductors with various values of κ , but identical thermodynamic critical fields, H_c . Inset shows the constitutive relation $B \equiv B(H)$ for a type-II superconductor.	31
2.6	Gapless superconductivity via the Abrikosov-Gor'kov mechanism. . .	35
2.7	Schematic of a generic phase diagram, showing the regions in which the classical and quantum fluctuations dominate.	37
2.8	Cartoon of the quasiparticle concept.	38
2.9	Non Fermi-liquid behaviour in $\text{Nb}_{1-x}\text{Fe}_{2-x}$ and YbRh_2Si_2	39
2.10	Phase diagrams of various “quantum critical” superconductors. . . .	40
3.1	Cross-section of the S700X susceptometer.	43
3.2	Superconducting isotherm from a sample of Sn used to determine the level of remanent field ≈ 0.5 mT.	44
3.3	Schematic of squid and coilset [1].	45

3.4	Comparison of the least-squares dipole fit and the multipole-expansion fit.	47
3.5	Carbon fibre reinforced epoxy resin sample holder (above) and plastic straw/gel capsule/PTFE sample holder (below).	49
3.6	Comparison of sample mounting methods.	50
3.7	Schematic showing the cycle by which the ^3He insert achieves 275 mK.	51
3.8	Cross-section schematic of the DMS.	54
3.9	Entropy profile of the salt pill during a demagnetisation cycle. . . .	55
3.10	Schematic of the sample and field arrangement in this four-point resistivity measurement.	57
3.11	Operating principle of the anvil cell.	58
3.12	Miniature anvil SQUID cell.	59
3.13	Preindented region of the gasket with a sample in the sample space. .	60
3.14	Main: Raw $M(T)$ data along with the empty cell run. Inset: Data following background subtraction - a clear superconducting transition is present.	61
3.15	Layout of the optical bench used for the ruby fluorescence technique. .	62
3.16	Pressure dependence of the characteristic spectra of a ruby chip. . . .	63
4.1	(a) Magnetic phase diagram of URhGe for two different field directions. A tricritical point can be seen at around 12 T as T_C is suppressed to 0 K, around which superconductivity grows. (b) Reemergence of superconductivity at high fields in the proximity of the tricritical point.	66
4.2	Signatures of ferromagnetic quantum criticality in the 1-dimensional system $\text{YbNi}_4(\text{P}_{1-x}\text{As}_x)_2$ at a critical doping $x_c = 0.1$	67
4.3	Crystal structure of CeAgSb_2 . Each unit cell contains two formula units, four unit cells are shown here.	68
4.4	Theoretical Fermi surfaces for CeAgSb_2 , matched against dHvA frequencies. The left hand figure corresponds to a hole sheet, whilst the other two are electron-like.	69
4.5	Spin-wave dispersion of CeAgSb_2 along high-symmetry directions. . . .	70

4.6	$d\rho/dT$ at a range of P , the pressure dependence of the A coefficient and the residual resistivity, and the proposed PT phase diagram. (b) PT phase diagram of CeAuSb ₂	72
4.7	Inelastic neutron scattering of CeAgSb ₂	73
4.8	Magnetic measurements to characterise single-crystal CeAgSb ₂ samples. Red traces correspond to <i>in-plane</i> measurements, whilst the blue ones are along the easy axis.	75
4.9	Transport measurements to characterise single-crystal CeAgSb ₂ samples. Inset shows the kink at T_C corresponding to the ferromagnetic transition.	76
4.10	Raw MAC data for CeAgSb ₂ . All traces swept down then up in temperature (bar 0 kbar and 33 kbar, which are downsweeps only). No appreciable hysteresis.	78
4.11	Pressure dependence of $M(T)$ in nominally zero (4 G) field. Inset shows how the transition temperature T_C was extracted.	81
4.12	Left: PT phase diagram showing the location of the ferromagnetic phase as a function of the applied pressure P . The dot-dash line is a fit to $T_C(P) \propto P - P_c ^\alpha$ with $P_c = 35.8$ kbar, and $\alpha = 0.35 \pm 0.05$. Right: Pressure dependence of the saturated moment, where the error bars reflect the change in pressure before and after the measurement.	82
4.13	Temperature dependence of the in-plane magnetisation at various transverse fields. M and H in SI units such that M/H is dimensionless.	85
4.14	Isothermal field sweeps for CeAgSb ₂ , measured in-plane.	86
4.15	(a) Specific heat of CeAgSb ₂ in a transverse field. The inset shows the crossing point at different fields as described in the text. (b) Second-derivative of the magnetisation M'' at various transverse fields, with an inset showing the corresponding feature to the crossover.	88
4.16	$\rho(T)$ data at various transverse fields. The dotted line is a low- T fit of $\rho(T) = \rho_0 + AT^2$ to the zero-field trace – as shown in the top left of figure 4.18 – to show the superquadratic dependence of the resistivity.	89

4.17	Semilog plot of $\rho(T)$ for zero and 6 T transverse fields, with a comparison of the fits to eqn. 4.9 (red) and 4.10 (blue), together with the Fermi liquid contribution - $\rho(T) = \rho_0 + T^2$ - determined as in the top left of figure 4.18.	90
4.18	Field dependence of the fitting parameters obtained by fitting the data to equation 4.9. Bottom figure shows the field dependence of the goodness-of-fit coefficient.	92
4.19	(a) Schematic of the coilset and its components. (b) Coilset on copper sample platform after measurement.	93
4.20	AC-susceptibility measured along the easy axis for CeAgSb ₂ in zero field. The peak at ~ 10 K corresponds to the magnetic transition, whilst the feature at low temperature is due to the superconducting transition of the aluminium cradle holding the coil. Inset: The imaginary part $\chi''_{ }$	94
4.21	AC-susceptibility of CeAgSb ₂ in zero field, inset shows the imaginary part $\chi'_{ }$	95
4.22	Comparison of the real part of the susceptibility $\chi^{ }$ in different ac excitation fields.	96
4.23	Complete <i>HT</i> phase diagram for CeAgSb ₂	97
4.24	Specific-heat data for the Ising-like ferromagnet CoNb ₂ O ₆ in a transverse field.	100
5.1	Generic phase diagram for the 122-iron arsenides and the high-temperature cuprate superconductors.	104
5.2	ThCr ₂ Si ₂ (I4/mmm) type structure shared by LuFe ₂ Ge ₂ and YFe ₂ Ge ₂	105
5.3	Composite doping and pressure phase diagram of YFe ₂ Ge ₂ and LuFe ₂ Ge ₂	106
5.4	Heat capacity of LuFe ₂ Ge ₂ and YFe ₂ Ge ₂	107
5.5	Non-Fermi liquid signatures appearing in the electrical resistivity and the heat capacity of YFe ₂ Ge ₂	109
5.6	RF induction furnace.	110
5.7	Powder XRD spectra from a typical sample of YFe ₂ Ge ₂	111

5.8	Temperature and field-dependent magnetisation measurements to characterise samples of YFe_2Ge_2	113
5.9	Comparison of $M(T)$ for bulk (a) and powdered (b) YFe_2Ge_2 . Clear flux exclusion is seen beneath a critical temperature $T_c \approx 1.5$ K. M and H are both expressed in SI units such that full diamagnetism would give $M/H = -1$	116
5.10	Schematic showing the spatial variation in the flux density $B(x)$ as the temperature is changed. Left: warming (ZFC). Right: cooling (FC). unimpeded, and by $T = T_{c1}$ we recover the Meissner condition $B = 0$ and	117
5.11	The anisotropy between FC and ZFC sweeps - f_M - as a function of the pinning strength - γ	119
5.12	Effects of sample size on magnetic response.	120
5.13	123
5.14	Low field $M(H)$ curves at various temperatures.	125
5.15	$H_{c2}(T)$ for YFe_2Ge_2 as determined from resistivity measurements [2]. The orange and green curves show the WHH result in the clean and dirty limits, and the blue dotted line is a fit to $T \sim H - H_{c2} ^\alpha$, with $\alpha=0.64$. The Pauli-limited field H_P is also shown.	126
5.16	Examples of ZFC/FC anisotropy appearing in the DC magnetisation a 1111 compound and MgB_2	129
5.17	Plot of the superconducting volume fraction against the ferromagnetic impurity level for YFe_2Ge_2	130
5.18	Heat capacity of YFe_2Ge_2 from a new batch of flux-grown samples. A clear anomaly can be seen below $T = 2$ K which disappears in the presence of a magnetic field.	134
6.1	Crystal structure of $(\text{Ca,Sr})_3\text{Ir}_4\text{Sn}_{13}$	137

6.2	Doping and pressure phase diagram of the $(\text{Ca}_x\text{Sr}_{1-x})_3\text{Ir}_4\text{Sn}_{13}$ series. My own contribution to this publication was to investigate the magnetic anisotropy in these compounds, in order to rule out the possibility that the phase transition taking place at T^* was a magnetic – rather than structural – one. Some of this data is shown in figure 6.4.	139
6.3	(a) Temperature evolution of the Sn(2) bond distances from the central Sn(1) site growing out of T^* . (b) Heat capacity of $\text{Ca}_3\text{Ir}_4\text{Sn}_{13}$, showing a clear anomaly at T^*	140
6.4	Magnetic susceptibility of $\text{Sr}_3\text{Ir}_4\text{Sn}_{13}$ and $\text{Ca}_3\text{Ir}_4\text{Sn}_{13}$ measured along a number of non-orthogonal orientations. There is a marked lack of magnetic anisotropy; the T^* transition is non-magnetic.	141
6.5	Raw data from the study of $\text{Ca}_3\text{Co}_4\text{Sn}_{13}$ in a miniature anvil squid cell. All traces shown have been zero-field-cooled, and then warmed in 0.4 mT of applied field. The top left figure shows the empty cell background run after the sample had been removed.	144
6.6	$M(T)$ data from $\text{Ca}_3\text{Co}_4\text{Sn}_{13}$ taken at various pressures in miniature anvil SQUID cell. Background has been subtracted. Glycerin used as pressure medium. Solid (open) symbols show points collected on pressuring (depressurising).	145
6.7	Phase diagram showing the pressure dependence of T_{sc} in $\text{Ca}_3\text{Co}_4\text{Sn}_{13}$, with the pressure determined by the ruby fluorescence technique. Solid (open) symbols show points collected on pressuring (depressurising). Error bars reflect the width of the transition appearing in $M(T)$	146
6.8	$M(T)$ data of $\text{Ca}_3\text{Ir}_4\text{Sn}_{13}$ at various pressures in a miniature anvil SQUID cell. The left figure shows the transition temperature <i>increasing</i> as the pressure is increased, whereas the right figure shows it <i>decreasing</i> with an increased P	147
6.9	PT phase diagram of $\text{Ca}_3\text{Ir}_4\text{Sn}_{13}$, constructed from a series of miniature anvil SQUID cell runs. Different coloured dots represent different cell runs. The size of the error bars reflect the width of the transition as shown in the inset of 6.7.	148

6.10	$M(H)$ data for $\text{Sr}_3\text{Ir}_4\text{Sn}_{13}$ and $\text{Ca}_3\text{Ir}_4\text{Sn}_{13}$ to determine the upper critical field $H_{c2}(T)$. Arrows show the direction of the field sweep.	151
6.11	Magnetic phase diagram for $(\text{Ca},\text{Sr})_3\text{Ir}_4\text{Sn}_{13}$ showing the temperature dependence of the upper critical field $H_{c2}(T)$. The lines of fit correspond to the WHH theory of the upper critical field in the clean limit.	152
6.12	Similar “fishtail”-type feature appearing in the magnetisation of $\text{Ca}_3\text{Rh}_4\text{Sn}_{13}$, along with the “peak” in the critical current J_c	153
6.13	Schematic of the FLL reorganisation which takes place at H_p	154
6.14	Composite phase diagram of the $\text{A}_3\text{B}_4\text{Sn}_{13}$ series, showing the $(\text{Ca}_x,\text{Sr}_{1-x})_3\text{Ir}_4\text{Sn}_{13}$ series and data from $\text{Ca}_3\text{Co}_4\text{Sn}_{13}$. $x = 0.4$ and $x = 0.5$ data.	155
6.15	Temperature dependent magnetisation $M(T)$ for $\text{Ca}_3\text{Ir}_4\text{Sn}_{13}$ showing the bulk superconducting transition at $T_c = 6.96$ K, along with the impurity phase transition at $T_{Sn} = 3.72$ K, with ZFC and FC traces shown.	156
A.1	Means of extracting H_{c1} from isothermal field sweeps.	161
B.1	Irreversibility in a type-II superconductor	165

List of Tables

2.1	Functional forms of $g(\varphi)$ for given pairing symmetries, a is a coefficient controlling the anisotropy.	33
5.1	Summary of magnetic measurements	114
5.2	Critical fields and κ values for other type-II superconductors.	132

Chapter 1

Introduction

The role of solid-state physics in the explosion of technological prowess which took place over the past century cannot be overstated. The entirety of modern computing rests upon the workings of the transistor, a component made possible due to a complete quantum band theory of materials. Significant strides forward in our technological capacity are crucially linked to the advances we make in our understanding of the most fundamental processes which take place within the solid.

In fact, more than just using the richness of solid-state phenomena to make our mobile phones faster, the struggle toward the understanding of the quantum mechanical many-body solid has generated many seminal contributions to modern physics along the way: for example the Anderson-Higgs mechanism [3,4] – by which photons in superconductors can become “massive” – or the Landau theory of continuous phase transitions [5].

For example, whilst the introduction of superconducting technology – which could transmit electromagnetic energy without loss – would be likely to transform the modern world, the current restriction to cryogenic temperatures means that they can not play much of a role in our everyday lives. For example, amongst the “classical” superconductors¹ the highest T_c found so far is MgB_2 , whose $T_c = 39$ K [6].

¹Those which are driven by an electron-phonon mechanism.

For a long time it seemed unlikely that a superconducting material would be found with a T_c even above liquid nitrogen temperatures ($T = 77$ K). However, the discovery of layered copper-based superconductors in the late 1980s by Bednorz and Müller [7, 8], which have since been found to give the highest critical temperatures yet, opened the door for superconductivity at room temperature. Tantalisingly, the recent discovery of superconductivity in layered iron-based systems [9] – which in some respects, are very similar to the copper oxide systems – has afforded us a new line of attack in our hopeful solution of the problem, whilst a full understanding of the microscopic picture is still lacking.

In this thesis, we investigate the physics of a zero-temperature phase transition. This occurs when a macroscopic phase transition is suppressed to absolute zero, inducing strong quantum-mechanical fluctuations which may profoundly affect the low-temperature ground state. This can result in novel phenomena which may be vastly differently to that seen normally. In particular, we focus on the appearance of *superconductivity* in this region, which is often found to be of an unconventional type. The superconductivity which appears in both the cuprate and iron-based systems is thought to emanate from such a region.

Experimentally, we will mainly use a magnetic probe to investigate the macroscopic properties of our systems, simultaneously tuning them with hydrostatic pressure, magnetic field and composition. We show the results of our investigation of the suppression of a structural phase transition, and two magnetic ones.

In 1959, Richard Feynman gave a lecture about the burgeoning field of nanotechnology titled “There’s plenty of room at the bottom!” [10], where he highlighted the wealth of possibility afforded by the proper study and manipulation of systems at the nanometer length-scale. The length-scales of the structures in the solid-state are even smaller still, and so proper understanding of the underlying mechanics and interactions, will be crucial to both our understanding of physics generally, and also the exploitation of it to our own ends.

Chapter 2

Theoretical Background

2.1 Phase transitions

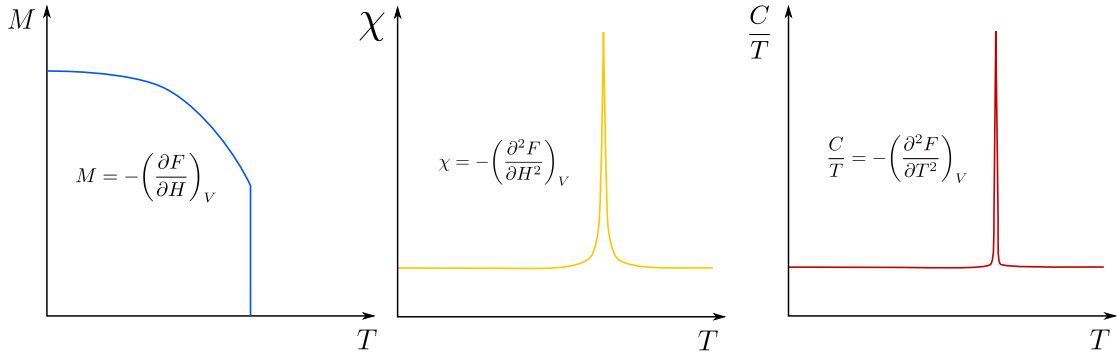
2.1.1 Continuous and discontinuous phase transitions

A physical system can be characterised by a series of well-defined macroscopic quantities: pressure, volume, internal energy and so on. A *phase transition* is said to occur when these properties transform from one well-defined set to another. Most typically this will occur as a function of one or more external parameters, such as temperature or pressure. We can classify the nature of the phase transition by the characteristic manner in which these macroscopic quantities transform into one another.

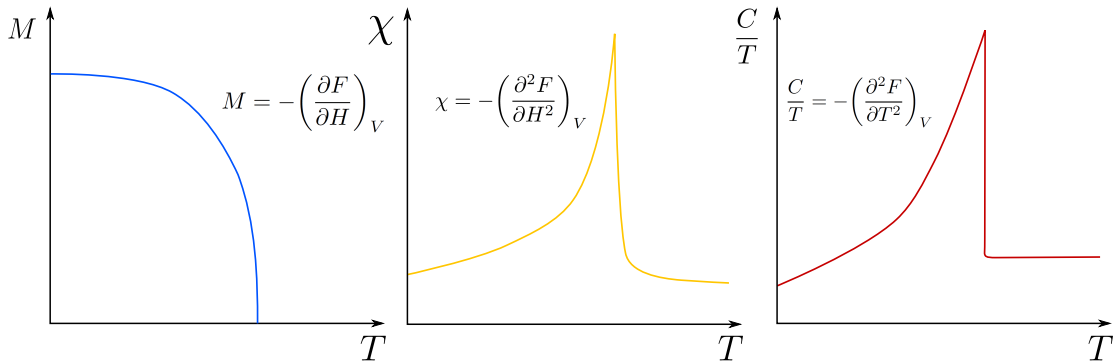
The Ehrenfest scheme gives the *order* of a phase transition based on the lowest-order derivative of the free energy F which shows a discontinuity with respect to some other thermodynamic variable, X . A *first-order* transition would be one in which $\partial_X F$ is non-continuous across the phase boundary¹, whilst a *second-order* transition would vary smoothly in $\partial_X F$, but show a discontinuity in $\partial_X^2 F$. The

¹Where we adopt the shorthand

$$\partial_X F = \frac{\partial F}{\partial X} \tag{2.1}$$



(a) Measurable quantities at a first-order transition.



(b) Measurable quantities at a second-order transition.

Figure 2.1: Analytic properties of the derivatives of F at a phase transition.

derivatives of F often correspond to physical quantities which can be determined through experiment². Consequently, the order of a phase transition seen in the lab can be deduced by examining the functional form of variables such as the specific heat or the magnetisation across the phase boundary. A schematic showing

²For example, in a magnetic system we have that the magnetisation, M -

$$M = -\left(\frac{\partial F}{\partial H}\right)_V \quad (2.2)$$

the specific heat C -

$$\frac{C}{T} = -\left(\frac{\partial^2 F}{\partial T^2}\right)_V \quad (2.3)$$

and the magnetic susceptibility χ -

$$\chi = -\left(\frac{\partial^2 F}{\partial H^2}\right)_V \quad (2.4)$$

the differences between variables derived from the free energy at first-order and second-order ferromagnetic (FM) transitions within the Ehrenfest scheme is shown in figure 2.1³

Another key concept in the theory of phase transitions is the idea of an *order parameter*. The order parameter is a variable - M , say - whose expectation value is zero above the phase transition, but non-zero below it⁴. The order parameter is commonly related to the first-derivative of the free energy with respect to another thermodynamic variable. As a consequence for a first-order transition at the critical temperature - where there is a discontinuity in the first derivative of F at T_c - the order parameter M must *necessarily* jump instantaneously from 0 to some finite value. In contrast, at a second-order transition, where all first derivatives of F vary smoothly, M is required to grow continuously from zero out of the critical temperature T_c .

Figure 2.2 shows real examples of first- and second-order behaviour at an *anti-ferromagnetic* (AF) transition, determined from neutron scattering [11, 12]. The order parameter in an AF transition is the magnetisation M_i of the sub-lattices i , which is determined experimentally by the appearance at the Néel temperature T_N of a magnetic Bragg peak at a finite wavevector \vec{Q}_{order} . In MnS_2 , the magnetic reflection appears suddenly at T_N - a first-order “discontinuous” transition - whilst at the transition in Pr_2I_5 , the peak grows continuously from zero - a second-order “continuous” transition.

The crucial difference between the two is that at a continuous transition, the critical temperature marks the boundary between two *totally degenerate macroscopic states*. As a result, thermal fluctuations - on the order of $k_B T_c$ - can “wobble” the system into and out of the ordered state; arbitrarily small energy variations

³It should be noted that such exact 2nd order transitions do not exist in nature. The Ehrenfest scheme represents a *mean field* approximation, whereby the complex interactions which appear between all of the microscopic components of a system are replaced with a single averaged effect, which all constituent particles feel. As will be discussed shortly, mean field theory in real systems breaks down near the critical temperature due to the presence of strong fluctuations. In the critical region, physical quantities such as the specific heat are found to diverge with universal exponents that are the same above and below T_c .

⁴When we say *above* and *below*, we are referring to the temperatures *above* and *below* the critical temperature T_c .

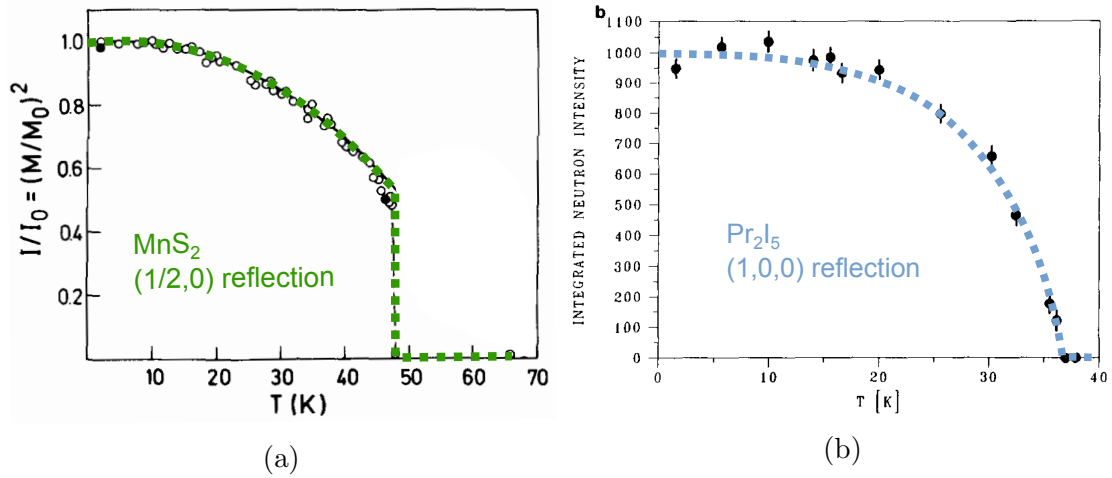


Figure 2.2: First and second order antiferromagnetic transitions in MnS_2 and Pr_2I_5 , determined via neutron scattering [11, 12]. Magnetic peaks which appear below T_N reflect the appearance of the AF order parameter at the phase transitions. In MnS_2 the peak appears discontinuously at T_N – a first order transition – whilst in Pr_2I_5 the peak grows smoothly from 0 – a second-order transition.

will induce microscopic fluctuations in the order parameter δM . This is not the case at a first-order transition, where the latent heat Q_L required (either absorbed or released) to push the system across the boundary acts a buffer, making the transition robust against the influence of the thermal fluctuations.

The correlation length $\xi(T)$ gives a measure of the length-scale over which the order parameter fluctuates. At a continuous phase transition, $\xi(T)$ diverges at T_c such that the system has no characteristic length scale: it is scale-invariant [13]. In the vicinity of T_c , fluctuations in the order parameter exist across all length scales. Physically, this means that on the approach to T_c , “bubbles” of incipient order appear throughout the system, whose size increase as $T \rightarrow T_c$. In a ferromagnetic system this would correspond to pockets of co-aligned spins, of all sizes, forming then breaking apart, whilst in the liquid-gas transition, nascent bubbles of liquid and gas fluctuate in and out of existence. The divergence of $\xi(T)$ at T_c results in the scaling laws which are found in the susceptibility or specific heat [13].

In fact, these fluctuations may persist over such large length scales that they can be seen with the naked eye. Figure 2.3 shows a methanol/cyclohexane mixture ex-

hibiting the phenomena known as *critical opalescence* [14]. Near the critical point large density fluctuations are found at all length scales, some of which coincide with the wavelength of light. This results in an enhancement of optical scattering through the fluid, which we see as a “milkyiness”.

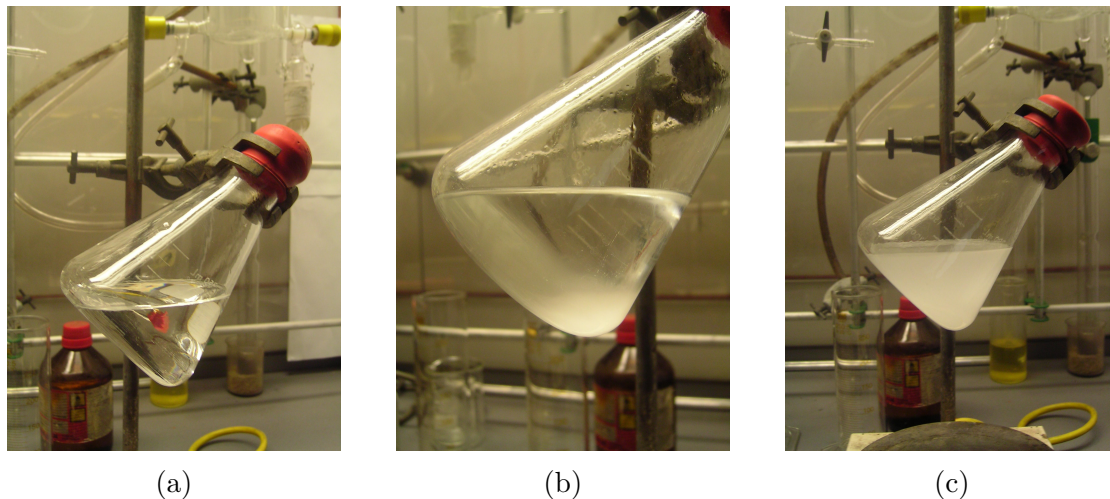


Figure 2.3: Critical opalescence appearing in a methanol and cyclohexane mixture near its boiling point [14]. (a) Single phase. (b) Onset of density fluctuations. (c) Critical opalescence.

2.1.2 Landau theory of the order parameter

The most ubiquitous framework used to describe the phenomenology appearing at continuous phase transition is *Landau theory*. The central pillar of Landau theory is that the free energy is a smoothly-varying function of the order parameter $F(M)$ such that we may expand it about its minimum. From previous definition of the order parameter, we would expect that in the high temperature state, $F(M)$ should have a minimum at $M = 0$, whilst upon moving through the phase transition, $F(M)$ would have minima at some finite value of $|M| = \tilde{M}$. The most simple

expression of the free energy is given by⁵:

$$F(M, T) - F(0, T) = a(T)M^2 + \frac{1}{2}b(T)M^4 + \dots \quad (2.5)$$

Upon inspection, we can see that $b(T) > 0$ as otherwise there would be no minimum in energy. Likewise it must be the case that $a(T)$ changes sign as we pass through the transition as otherwise we would not find an energy minimum at finite M .

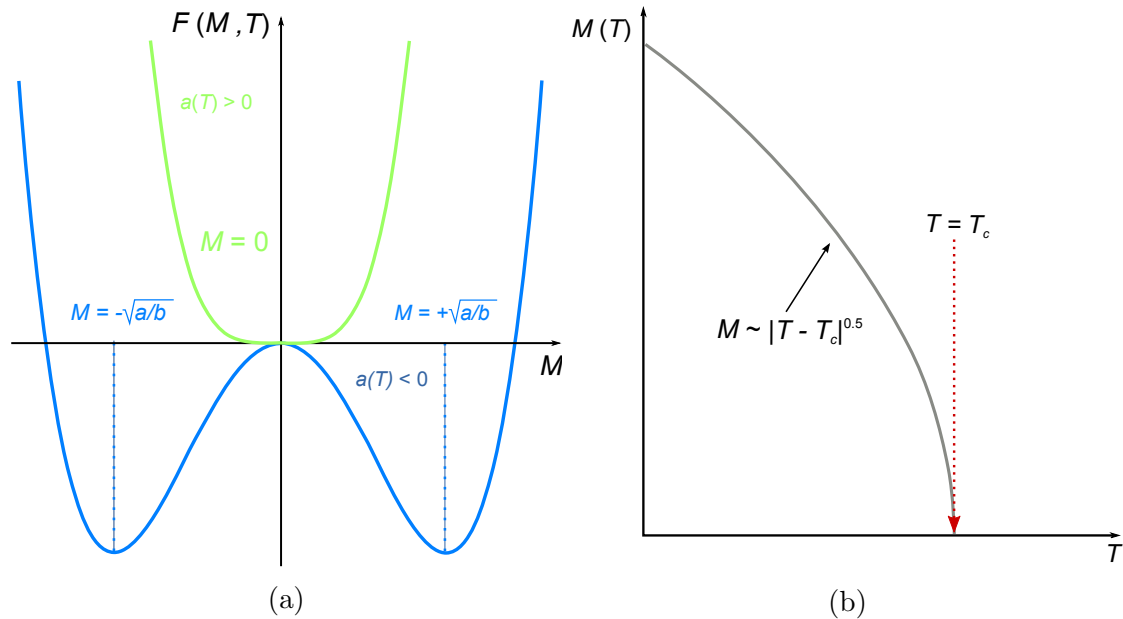


Figure 2.4: (a) Form of the free energy $F(M)$ above and below the transition temperature. (b) Temperature dependence of the order parameter $M(T)$ given by the Landau theory.

Expanding $a(T)$ in powers of T around T_c :

$$a(T) \approx a(T_c) + \dot{a}(T - T_c) + \dots \quad (2.6)$$

The constant $a(T_c)$ can be reabsorbed into our definition of $F_0(0, T)$, such that the

⁵The free energy should be symmetric with respect to the orientation of M , i.e. $F(M) = F(-M)$, and so only even powers of M are retained.

prefactor $a(T)$ in equation 2.5 is now

$$a'(T) = \dot{a}(T - T_c), \quad (2.7)$$

Consequently, by finding the minima in $F(M, T)$ at $T < T_c$ we find that close to the transition, the order parameter M grows as

$$|M| \sim |T - T_c|^{\frac{1}{2}} \quad (2.8)$$

Provided an order parameter can be identified, one may construct the Landau theory and analyse its phenomenology. As the mean-field Landau picture is not concerned with the microscopics of the problem – only the existence of some order parameter and its symmetries – it may be applied to manifold and diverse systems, revealing the universal nature of many seemingly disparate phase transitions. The form of the free energy given in equation 2.5 is only the very simplest one, whereas the theory can be augmented to take into account effects such as an inhomogeneous order parameter $M(\vec{r})$, coupling to external fields and/or the possibility of multiple order parameters.

2.2 Superconductivity

2.2.1 Overview

Superconductivity was born a century ago following the discovery by Heike Kamerlingh Onnes in 1911 that the electrical resistance of mercury dropped to zero beneath a critical temperature of 4.2 K⁶. It was subsequently found by Meissner and Oschenfeld that a “superconductor” (as named by Onnes) expelled any applied magnetic flux from its interior.

It took another fifty years for a successful microscopic theory to arrive, although a large phenomenological framework had been developed in the meantime. The London brothers were able to explain the magnetic flux expulsion and saw that the Meissner effect in a superconductor was distinct from the shielding which would be seen in a perfect conductor. Then, Ginzburg and Landau formulated a macroscopic, thermodynamic theory in terms of a complex-valued order parameter:

$$\psi = |\psi|e^{i\theta}. \quad (2.9)$$

The Ginzburg-Landau description was successful as it paid no heed to the (unknown) microscopics of the problem, only the symmetry of its order parameter, ψ . This meant that a great deal of the phenomenology could be accounted for, in spite of the lack of a full quantum mechanical description.

In his 1956 paper *Bound electron pairs in a degenerate Fermi gas* [15], Cooper showed how a Fermi surface is always unstable to the formation of pairs, when an attractive interaction V exists between pairs of electrons near the Fermi energy ϵ_F - this holds true even for an arbitrarily small V . This forms the basis of the microscopic solution: that the “pairing off” of electrons into integer-spin quasiparticles forms a bosonic fluid which is able to undergo a Bose-Einstein-type condensation into a collective, superfluid ground-state.

In conventional superconductors, the pairing interaction takes place through the

⁶An experiment made possible by Onnes’ successful condensation of liquid helium a few years before.

phononic modes of the crystal⁷. As a result of its electrostatic attraction to the screened positive charge at every atom, an electron moving through the solid pulls the lattice towards itself. The lattice responds far slower than the electrons travel – owing to the Fermi temperature greatly exceeding the Debye temperature: $T_F \gg \Theta_D$ – meaning that the electron has “whizzed off” long before the lattice relaxes back to its equilibrium position. The resulting temporary accumulation of positive charge is then seen by a second electron, which is attracted towards it, giving an effective attraction between the two electrons.

In its most simple form, this is the basis of the pairing mechanism between electrons taking place in a conventional superconductor.

2.2.2 BCS result

The BCS (Bardeen-Cooper-Schrieffer) picture [17] is a mean-field theory of the Fermi gas, whereby electrons of momenta \vec{k} and \vec{k}' , found within $\hbar\omega_D$ ⁸ of the Fermi surface feel a mutual interaction $V_{\vec{k}\vec{k}'}$ between themselves [18]. By construction of an appropriate ground-state wavefunction $|\text{BCS}\rangle$, and a *mean-field* hamiltonian \hat{H} which only considers attractive interactions between pairs of electrons with opposite spins, it is possible – via a canonical transformation of the single-electron operators $c_{\vec{k}}^\dagger$ – to diagonalise \hat{H} and determine the quasiparticle excitation spectrum.

Crucially, BCS found that the coherent superconducting groundstate was protected by an energy gap in the excitation spectrum – a prediction made already by experiment. The \vec{k} -dependent gap is given self-consistently by [18]:

$$\Delta_{\vec{k}} = - \sum_{\vec{k}'} \frac{\Delta_{\vec{k}}}{2E_{\vec{k}'}} V_{\vec{k}\vec{k}'}, \quad (2.10)$$

⁷The discovery of the isotope effect [16] was an important early clue on the path to the electron-phonon mechanism. These experiments found that the superconducting critical temperature T_c was affected by the replacement of lattice sites by their – electronically equivalent, but more massive – isotopes, showing that the appearance of superconductivity in some ways depended strongly on the mechanical or vibrational qualities of the crystal.

⁸Where ω_D is the Debye frequency of the lattice.

where $V_{\vec{k}\vec{k}'}$ is the attractive interaction between a spin-up and spin-down electron of momenta \vec{k} and \vec{k}' . The BCS approximation is made by assuming that this pairing interaction is only present within a thin shell of the Fermi-surface, and that it is constant within it and zero everywhere else. This removes the \vec{k} -dependence of equation 2.10, allowing it to be evaluated exactly. At finite T it follows that the critical temperature T_c is related to the excitation gap by:

$$\Delta_{BCS}(0) = 1.764k_B T_c, \quad (2.11)$$

which is found to hold true in a number of systems, namely those which are “weakly coupled”⁹.

2.2.3 Ginzburg-Landau theory

The Ginzburg-Landau approach focusses on the appearance of a minima in the electron free-energy which takes place at T_c , whereby the electron gas is able to lower its energy by a fraction of the electrons becoming superfluid. The order parameter is a complex field $\psi(\vec{r})$, whose modules squared gives the density of the superconducting electrons $n_s = |\psi|^2$.

Close to the transition temperature where n_s is small, and allowing for a spatial variation in the order parameter $|\nabla\psi|^2$, the free energy density takes the form:

$$f = \alpha|\Psi|^2 + \frac{\beta}{2}|\Psi|^4 + \frac{1}{2m}|(-i\hbar\nabla - 2e\vec{A})\Psi|^2 + \frac{|\vec{b}|^2}{2\mu_0}, \quad (2.12)$$

where coupling of ψ to the EM gauge field \vec{A} takes place through the covariant derivative $\nabla \rightarrow \nabla - \frac{2e}{i\hbar}\vec{A}$, and the last term gives the energy density of the magnetic induction field. Minimising f with respect to both the applied field and the field

⁹Weak coupling refers to the magnitude of the electron-phonon coupling parameter, λ

ψ , one arrives at the two *Ginzburg-Landau equations*:

$$0 = \frac{1}{2m}(-i\hbar\nabla + 2e\vec{A})^2\psi + (\alpha + \beta|\psi|^2)\psi \quad (2.13)$$

$$\vec{J}_s = \frac{ie\hbar}{m}(\psi^*\nabla\psi - \psi\nabla\psi^*) - \frac{4e^2}{m}\vec{A}\psi^*\psi \quad (2.14)$$

These equations generate a rich catalogue of phenomena and were able to account for many experimental results before the appearance of the BCS microscopic theory. Reexpression of each of the fields in equation 2.12 as dimensionless parameters reveals the two characteristic length scales which describe the physics: the *penetration depth* – λ , and the *coherence length* – ξ . The coherence length determines the distance over which ψ is allowed to change¹⁰, whilst the idea of a penetration depth had been found previously in the London brothers’ explanation of the Meissner effect, giving the length scale over which a magnetic field decays into the superconductor.

The relative sizes of κ and λ were found to have a profound influence on the properties of the superconducting fluid. The surface energy associated with a normal-superconductor (NS) boundary can be either positive or negative depending on the dominant length scale. For a *positive* NS surface energy (when $\lambda \ll \xi$) the boundary is stable and in tension, whilst a *negative* surface energy (which occurs when $\xi \ll \lambda$) is unstable - the system would tend to break up into areas which maximised the NS surface boundaries [18]. Superconductors are found to belong to two classes according the value of the dimensionless parameter

$$\kappa = \frac{\lambda}{\xi}. \quad (2.15)$$

For $\kappa < 1/\sqrt{2}$ the superconductor is classed as “type-I”, whilst for $\kappa > 1/\sqrt{2}$ it is “type-II”.

Abrikosov found solutions to the Ginzburg-Landau equations [19] whereby at a critical field H_{c1} , a type-II superconductor would admit a lattice of quantised flux lines – “fluxoids” – which arrange themselves periodically throughout the bulk.

¹⁰With reference to the BCS picture, the coherence length reflects the spatial extent of the bound Cooper pair.

The mutual repulsion between the fluxoids sets up the lattice structure, whereby within ξ of the centre of the fluxoid, the order parameter ψ is strongly suppressed, and the material is effectively normal.

2.2.4 Critical fields and the superfluid density

A type-II superconductor has two critical fields which can be seen directly through experiment. The first occurs at the point at which the quantised flux lines begin to move into the bulk of the superconductor (H_{c1}), and the second (H_{c2}) when the density of flux lines becomes too high, and the superconductor is driven normal again. Figure 2.5 shows the magnetisation curves expected below T_c , and the constitutive relation between B and H is given in the inset.

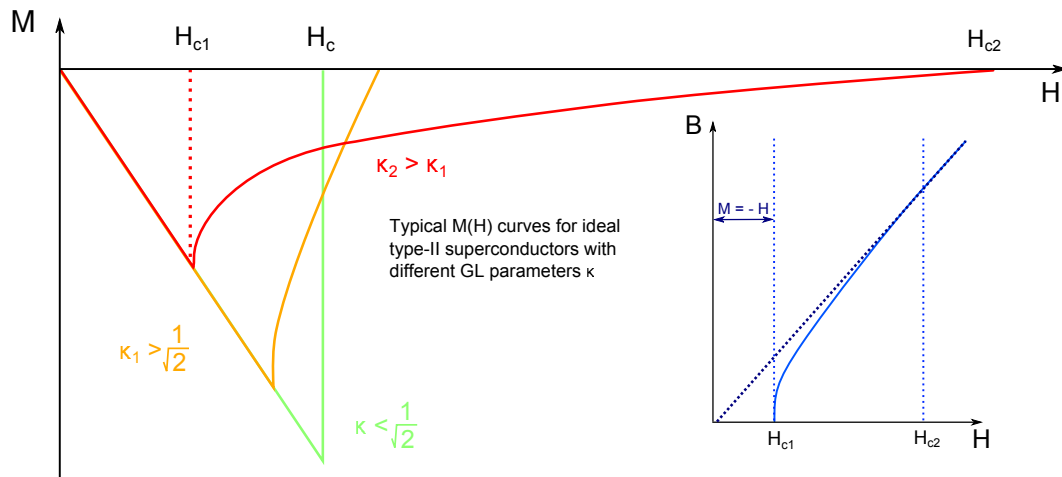


Figure 2.5: Magnetic isotherms for superconductors with various values of κ , but identical thermodynamic critical fields, H_c . Inset shows the constitutive relation $B \equiv B(H)$ for a type-II superconductor.

In the Meissner phase, $B = 0$ within the bulk of the superconductor, and so $M(H)$ is totally linear, with a gradient of -1: $M = -H$. Above H_{c1} the magnetisation is reduced as the field increases; the addition of every extra fluxoid to the bulk effectively “removes” more of the superconducting fluid, due to the introduction of more and more of the “normal” region at the centre of the core.

The traces shown in the main part of figure 2.5 correspond to an ideal, defect-free superconductor, where at every value of the applied field, the flux lines are distributed totally homogeneously throughout the sample such that B is constant and in equilibrium everywhere. In real systems, this is generally not the case, as *pinning sites* within the bulk – imperfections, such as crystal grain boundaries or impurities – tend to “hold on” to the fluxoids, resulting in deviations from the curves shown in figure 2.5. The influence of the pinning sites on the magnetic properties of the superconductor are detailed more fully in the appendix.

Establishing both the lower and upper critical fields from experiment reveals much about the superconducting state. From the upper critical field, we can estimate the coherence length ξ [20]:

$$B_{c2} = \frac{\Phi_0}{2\pi\xi^2}, \quad (2.16)$$

whilst the lower critical field H_{c1} provides valuable information about the gap structure, due to its relation to both the magnetic penetration depth λ_L and the superfluid density ρ_s .

From [21], the components of the inverse penetration depth, λ_i along the crystallographic axis i are given by:

$$\frac{1}{\lambda_i^2} = \frac{\mu_0 e^2}{4\pi^3 \hbar} \oint dS_F \frac{v_i^2}{|\vec{v}|} \left[1 + 2 \int_{\Delta(T,\varphi)}^{\infty} dE \frac{\partial f(E)}{\partial E} \frac{E}{\sqrt{E^2 - \Delta^2}} \right], \quad (2.17)$$

where dS_F is an element of area on the Fermi surface, v_i is the velocity at the Fermi level along the i axis, $f(E)$ is the Fermi function and $\Delta(T, \varphi)$ is the value of the energy gap at temperature T at an azimuthal angle φ along the Fermi surface¹¹. The first term is a constant determined by normal state parameters, whereas the second term describes the depletion of the superfluid by gradual thermal population of the excited Bogoliubov quasiparticle energy levels.

The superfluid density (normalised to its value at $T = 0$ K) is related the pene-

¹¹This is in the case of a quasi-2d Fermi surface.

Pairing symmetry	$g(\varphi)$
isotropic s -wave	1
anisotropic s -wave	$(1 + a \cos(4\varphi))/(1 + a)$
d -wave	$ \cos(2\varphi) $

Table 2.1: Functional forms of $g(\varphi)$ for given pairing symmetries, a is a coefficient controlling the anisotropy.

tration depth $\lambda(T)$ by

$$\frac{\rho^s(T)}{\rho^s(0)} = \frac{\lambda^2(0)}{\lambda^2(T)} \quad (2.18)$$

and also

$$\frac{\lambda^2(0)}{\lambda^2(T)} = \frac{H_{c1}(T)}{H_{c1}(0)} \quad (2.19)$$

such that the temperature dependence of $H_{c1}(T)$ is given directly by $\rho^s(T)$. Following the determination of $H_{c1}(T)$ experimentally, we can fit to the expression:

$$\frac{H_{c1}(T)}{H_{c1}(0)} = 1 + \frac{1}{\pi} \int_0^{2\pi} \int_{\Delta(T,\varphi)}^{\infty} d\varphi dE \frac{\partial f(E)}{\partial E} \frac{E}{\sqrt{E^2 - \Delta^2}}, \quad (2.20)$$

where the magnitude and symmetry of $\Delta \equiv \Delta(T, \varphi)$ represents the only degree of freedom. In general, $\Delta \equiv \Delta(T, \varphi)$ and may be written as [22]

$$\Delta(T, \varphi) = \Delta_0(T)g(\varphi), \quad (2.21)$$

where for different pairing symmetries the function $g(\varphi)$ takes on different forms – see table 2.1 [22]. The function $\Delta_0(T)$ corresponds to that of the weak-coupling, isotropic BCS model, and may be determined from the self-consistent gap equation, as in equation 2.10.

2.2.5 Destruction of the superconducting state

There are a number of mechanisms by which superconductivity may be destroyed, for example by the application of a sufficiently large magnetic field. This may

happen through one of two ways. Either, as the field is increased, the density of the magnetic flux lines within the superconductor becomes so great that the *normal* regions at the centre of the fluxoids begin to overlap. Or, the increased Zeeman-splitting of the up and down-spin electrons under the applied field eventually destroys all of the Cooper pairs. The first is the *orbital limit* whilst the second is the *Pauli limit*.

The theory of the upper critical field formulated by Werthamer, Helfand and Hohenberg considers the effect of the orbital limiting process [23], and they find that the expected orbital-limited critical field is given by:

$$H_{c2}^{orb.} = \gamma \left| \frac{dH_{c2}}{dT} \right|_{H=0} T_c \quad (2.22)$$

where the factor γ takes the values 0.69 and 0.73 in the dirty and clean limits, respectively. The Pauli limit is important when the condensation energy of the superconductor becomes comparable to the increase in energy associated with the Zeeman splitting of the bands. The Pauli-limited field is given by:

$$H_{c2}^P = \frac{\Delta_0}{\sqrt{2}\mu_B}, \quad (2.23)$$

where replacing the gap Δ_0 by the BCS expression given in equation 2.11 gives the Pauli limiting field in the weak-coupling limit as [20]:

$$H_{c2}^P = 1.84T_c(\text{T.K}^{-1}) \quad (2.24)$$

Abrikosov and Gor'kov [25] investigated the influence of the introduction of magnetic impurities into the superconducting bulk. They showed that as the magnetic impurity concentration n increases, there exists a region just before the SC state is totally destroyed in which the spectral gap in the density-of-states (DOS) $\Delta \equiv \Omega_G$ closes, whilst T_c and the gap-function $\Delta(r)$ remain finite¹². They found this to occur when n is at 91% of the critical concentration n_c required to fully quench the superconductivity. Figure 2.6 shows a schematic of the effect, taken from [18],

¹²Here we have to distinguish between the gap in the DOS, and the order-parameter – the *gap-function* $\Delta(r)$.

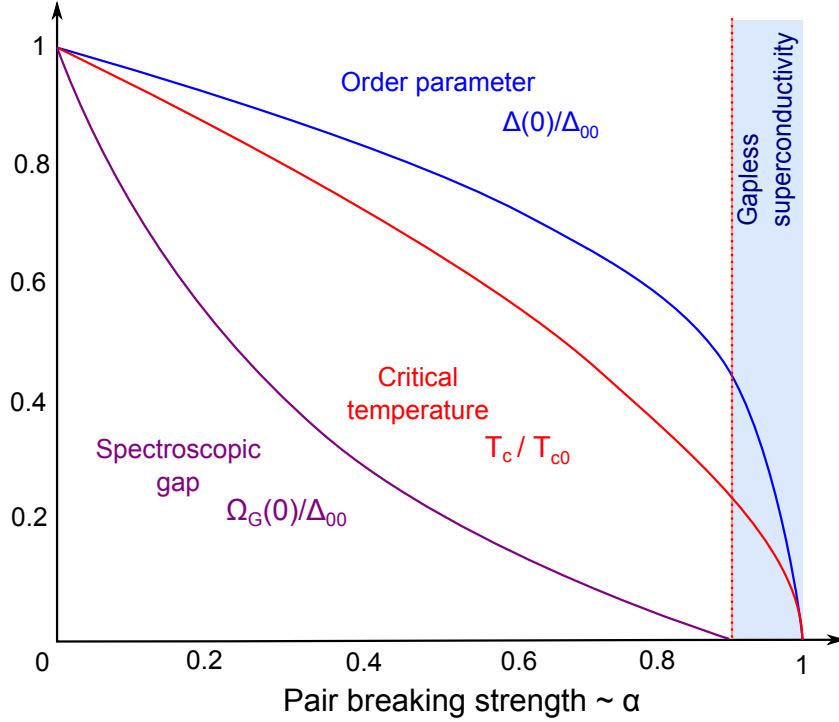


Figure 2.6: The dependence of the transition temperature T_c , the order parameter at zero temperature $\Delta(0)$, and the spectroscopic gap $\Omega_G(0)$ on the pair breaking parameter α . Δ_{00} is the value of Δ for $T = \alpha = 0$, and T_{c0} is the transition temperature at $\alpha = 0$. The shaded region shows the range of α values in which a supercurrent may still be supported whilst the spectroscopic gap $\Omega_G = 0$. Reproduced from [24].

where the magnetic impurity concentration is given by the pair-breaking parameter α . The same physics holds for other pair-breaking mechanisms, such that figure 2.6 is universal. In the case of magnetic impurities, α is given by

$$\alpha \approx \frac{nJ^2}{E_F}, \quad (2.25)$$

where J is the averaged exchange interaction.

2.3 Quantum Critical Superconductors

The phase transitions introduced at the start of this chapter took place as the temperature was reduced through a critical temperature T_c , or, at a fixed and finite temperature, a transition was induced by the tuning of some external parameter x through a critical value x_c . A phase transition at finite temperature is a “classical” phase transition¹³. We might imagine that the critical temperature of a “classical” transition could depend on the value of the tuning parameter x – pressure or transverse field, say – such that T_c can be suppressed to lower and lower temperatures by increasing x . If $T_c(x)$ drops monotonically as x increases, at a critical value of $x = x_c$ the ordering temperature T_c will be suppressed to 0 K. This means that were we to cool the system through $T_c(x = 0)$ to absolute zero and, and then slowly increase x from zero, at the critical value of the tuning parameter x_c the system would be driven from the ordered, broken symmetry state into a new disordered (or hidden ordered) state. This is a “quantum” phase transition, and for a continuous transition marks the location of a *quantum critical point* (QCP).

At the QCP there is a competition between two (or more) totally degenerate groundstates. At the classical critical point, the degeneracy of the competing phases resulted in critical behaviour induced by *thermal* fluctuations – scaling laws and so on – whilst at absolute zero, in the absence of thermal fluctuations, it is the *quantum* fluctuations which are relevant. Quantum fluctuations stem from the zero-point motion of the vacuum, a consequence of the uncertainty principle. Crucially, the quantum fluctuations at the QCP show scale invariance in both space *and* time [26], and as such their influence may be felt over a wide region of the phase diagram – at finite temperatures above the true QCP. The quantum critical region “fans out” as the temperature is increased from absolute zero - see the schematic in 2.7.

Whilst the critical end point found at absolute zero is beyond the scope of real experiment, the influence of the associated fluctuations across wide portions of the

¹³A phase transition at finite temperature is *always* classed as being “classical”, even when the new state is an inherently quantum-mechanical one, such as a superconductor or a ferromagnet.

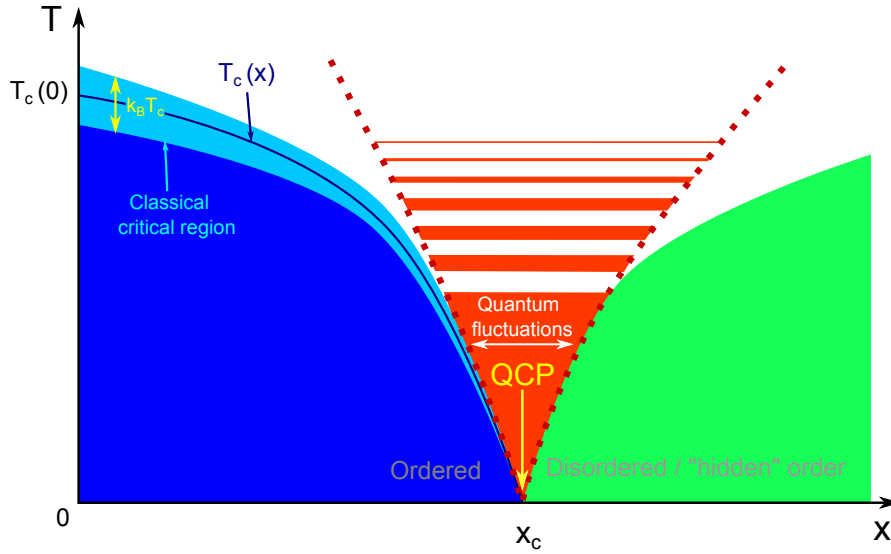


Figure 2.7: Schematic of a generic phase diagram, showing the regions in which the classical and quantum fluctuations dominate.

phase diagram elevates the QCP beyond a novel theoretical abstraction, and into something tangible which can be seen (and is seen) in real systems and across a wide temperature range.

To understand the influence of quantum critical fluctuations upon the ground-state of the system, we must introduce the “standard model” for our understanding of (typical) metallic systems – *Fermi liquid theory*. The work of Soviet physicist Lev Landau, Fermi liquid theory maps the insurmountably complicated interactive many-body problem¹⁴ onto a system of weakly scattering fermionic quasiparticles, which are electron-like in nature, but with dynamical properties – mass, magnetic moments and so on – which due to the presence of interactions, may be strongly renormalised from the bare electron values. In the interacting system, the low-lying excitations then do not correspond to the “bare” electrons or holes,

¹⁴A metallic system contains $> 10^{23}$ freely propagating electrons, each of which interact mutually through their own long-range Coulombic repulsion, as well as with the host lattice. Evidently, this is quite a complicated many-body problem, a notoriously difficult task which has provoked consternation for the theoretician for many centuries. This was initially a problem in classical mechanics - the late 19th century King of Sweden, Oscar II, offered substantial prize money for the analytic solution for the motion of “...arbitrarily many mass points that attract each according to Newton’s law ...” [27]. Although the task was found to be insoluble, the prize was finally awarded to Henri Poincaré for his contribution (but not solution) to the $n = 3$ problem.

but “quasiparticles” which behave *like* bare electrons, but whose properties are subtly affected (or “dressed”) by the influence of their own interactions. The quasiparticles themselves are no longer *true* eigenstates of the system such that the quasiparticles have a finite lifetime. This is given by the spectral width of the quasiparticle distribution, which disappears as one approaches the Fermi energy, meaning that the quasiparticles at ϵ_F are well-defined and long-lived.

Richard Mattuck offers a (somewhat) helpful analogy in his book - *A Guide to Feynman Diagrams in the Many Body Problem* [28] - by casting the “dressed” electron/quasiparticle picture in terms of horses and dust-clouds - see figure 2.8. As the horse moves rapidly along a dusty road, it interacts with the ground beneath its feet and kicks up a dust cloud which conceals it, slightly. What you see – what you measure – is then not the real *bare* horse, but a kind of composite, due to the interaction of the horse with its environment – a *quasihorse*.

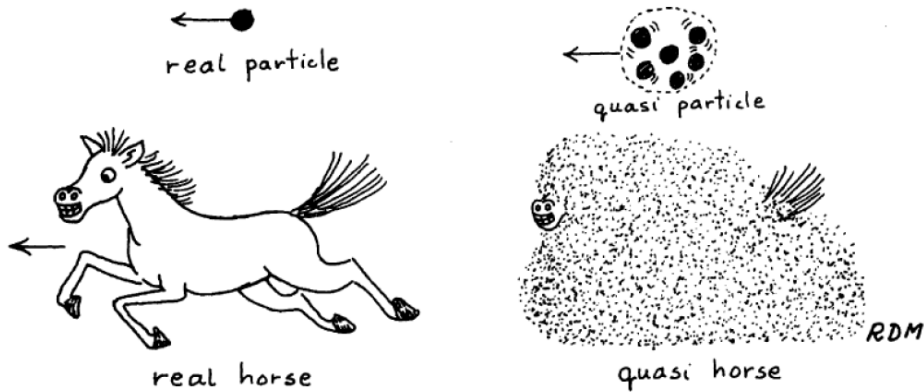


Figure 2.8: Cartoon of the quasiparticle concept, from [28].

Fermi liquid theory set the paradigm for our understanding of the interactive many-body state within the solid. For example, at its very limit, it is able to account for the so-called “heavy fermion” materials, whereby the strong correlations between itinerant *s*- and *p*-states with highly-localised *f*-electron states result in a groundstate whose low-lying excitations are electron-like, but with effective masses which may be up to 1000 times that of a bare electron [29].

Fermi liquid theory relies on the presence of short-range, repulsive interactions.

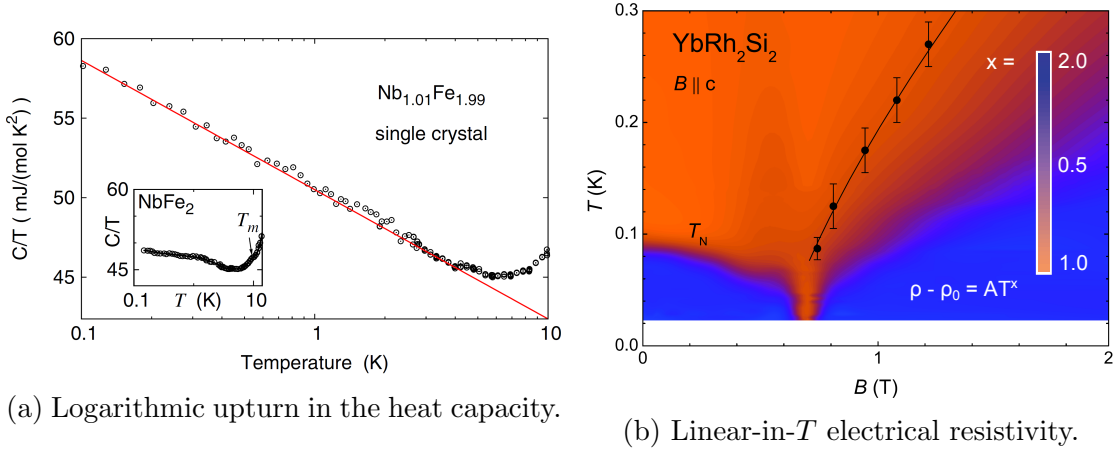


Figure 2.9: Non Fermi-liquid behaviour in $\text{Nb}_{1-x}\text{Fe}_{2-x}$ [30] and YbRh_2Si_2 [31].

When these are not present¹⁵, the Fermi liquid picture breaks down. This is commonly found on the border of the quantum critical region, whereby the divergence of the magnetic coherence length at the QCP results in a long-range quasiparticle interaction. Deviation from Fermi-liquid behaviour is therefore taken as a hallmark of the presence of quantum critical behaviour, most commonly seen as anomalous temperature dependences in the resistivity¹⁶ or specific heat (see figure 2.9).

The most striking manifestation of non-Fermi liquid behaviour is the appearance of a superconducting phase on the border of a zero-temperature transition. A generic phase diagram is seen in many systems whereby an ordered (typically magnetic) state is suppressed to near absolute zero by some external tuning parameter, but then rather than the phase diagram showing the “bare” critical point, a “bubble”

¹⁵As in the BCS superconductor, where the metallic state Fermi gas collapses into a coherent superfluid groundstate in the presence of the attractive V

¹⁶A Fermi-liquid is expected to display an electrical resistivity which varies quadratically with temperature $\rho_{FL} \sim T^2$ – a consequence of the quasiparticle scattering pathways available for excited states at the Fermi level [32]. In real systems, we have to amend this slightly by adding a constant term which takes into account scattering from impurities and defects, this is the *residual resistivity* ρ_0 which becomes apparent as $T \rightarrow 0$. The quality of a sample is then reflected in the magnitude of the ρ_0 term. We define a measure – the RRR value, which is given by the ratio of the resistivity at room temperature to that at the lowest temperatures

$$\text{RRR} = \frac{\rho(T = 300\text{K})}{\rho(T \approx 0\text{K})}. \quad (2.26)$$

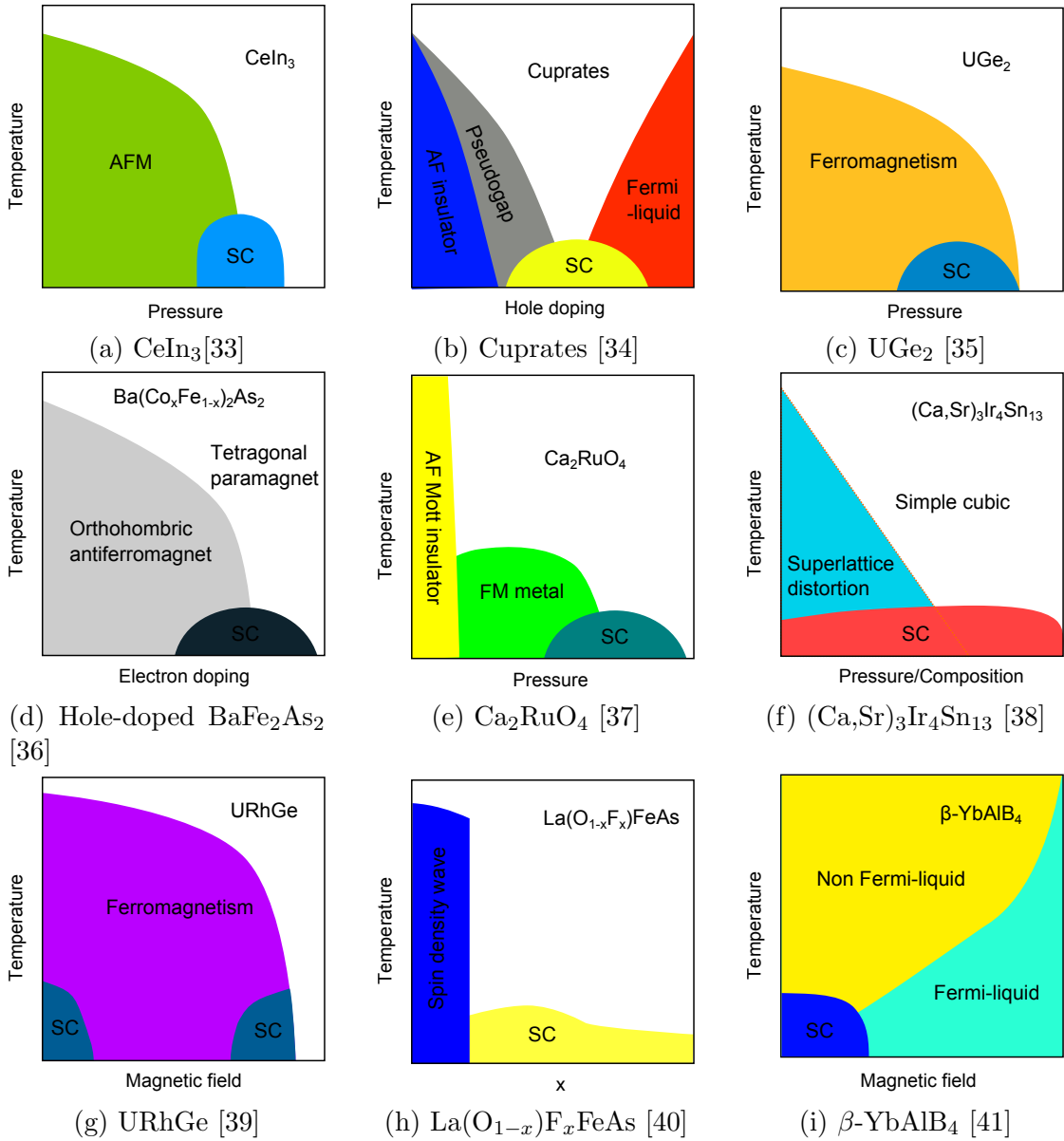


Figure 2.10: Phase diagrams of various “quantum critical” superconductors.

of superconductivity is found around the extrapolated zero-temperature transition; the QCP is “hidden” by a dome of superconductivity, whose critical temperature often peaks around the extrapolated zero-temperature phase transition. Figure 5.16 shows various phase diagrams from real systems where this structure appears, generally as a function of the applied field, pressure or composition.

The presence of strong magnetic fluctuations associated with a (magnetic) QCP would be anathema to a conventional, phonon-mediated superconductor, and so the appearance of superconductivity in such an environment is all the more intriguing. It is likely that the electronic pairing mechanism in many of these systems takes place via *magnetic* degrees of freedom rather than through the lattice [42, 43], and as a result we describe them as “unconventional” superconductors. For instance, in the high-temperature ceramic superconductors – where superconductivity has been found to persist up to 133 K [44] – the dome of SC is thought to be related to the suppression of a high-temperature antiferromagnetic transition, although the true microscopic description of the pairing is not yet known.

For the rest of this thesis we will focus on systems which display a particular phase transition – structural or magnetic – which can be suppressed with an external tuning parameter, and focus on the region at which the ordering temperature is suppressed to absolute zero.

Chapter 3

Experimental approach

Most of the data presented in this thesis are magnetic measurements. The magnetic behaviour of a solid-state system arises due to the collective interaction of its electrons, each of which behaves on its own somewhat like a microscopic magnet. We define the magnetisation of the sample \vec{M} as being the average magnetic moment per unit volume, and the magnetisation induced in reaction to an applied field \vec{H} is given by:

$$\vec{M} = \chi\vec{H}, \tag{3.1}$$

where χ is the response function - the *magnetic susceptibility*. As $\chi = dM/dH$, it is more sensitive to small changes of flux than \vec{M} . Both \vec{M} and χ may be established experimentally, and so with knowledge of how these variables should respond to field and/or temperature for different magnetic phases, we can interpret experimental data accurately and usefully.

3.1 DC magnetometry

Here we detail the means of determining the macroscopic \vec{M} of a sample, using a highly-sensitive superconducting detection system.

3.1.1 S700X Susceptometer

All of the DC magnetisation data presented within this thesis were collected using a Cryogenics Ltd S700X susceptometer, capable of performing DC susceptibility measurements - a schematic cross-section of which is shown in figure 3.3. It can collect data across a temperature range 300 K - 1.6 K, extendable down to <280 mK using the ^3He insert option.

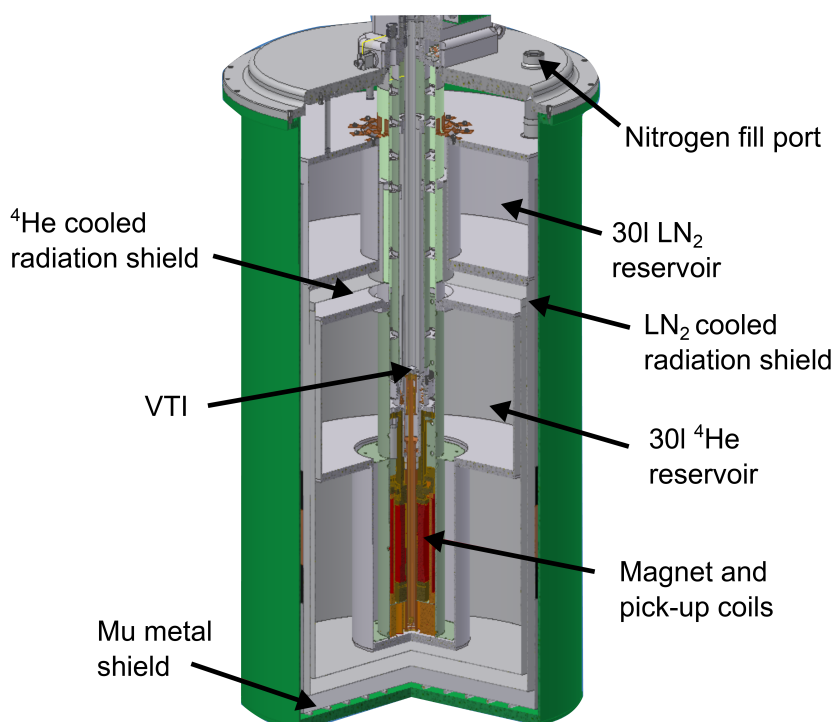


Figure 3.1: Cross-section of the S700X susceptometer, from [1].

The sample sits within a variable temperature insert (VTI), which is connected to the ^4He reservoir via a fine impedance - the *needle valve*. By vacuum pumping

on the VTI, liquid helium is drawn through the needle valve towards the sample. Upon meeting the low pressure within the insert, the liquid helium rapidly expands and boils back to gas, which flows over the sample and cools it. A heater controls the temperature of the ^4He gas such that the whole temperature range may be covered. By adjusting the needle-valve one can reduce the “base temperature” down to ≈ 1.5 K, although in practise it is not straightforward to operate at $T < 2.1$ K, as this is when ^4He undergoes a superfluid transition, making it difficult to control the temperature. Temperature control takes place through a Lakeshore 336 temperature controller, which monitors two thermometers and drives a PID controlled heater. Thermometer “A” gives the temperature of the helium flowing into the VTI, whereas thermometer “B”, is the sample temperature.

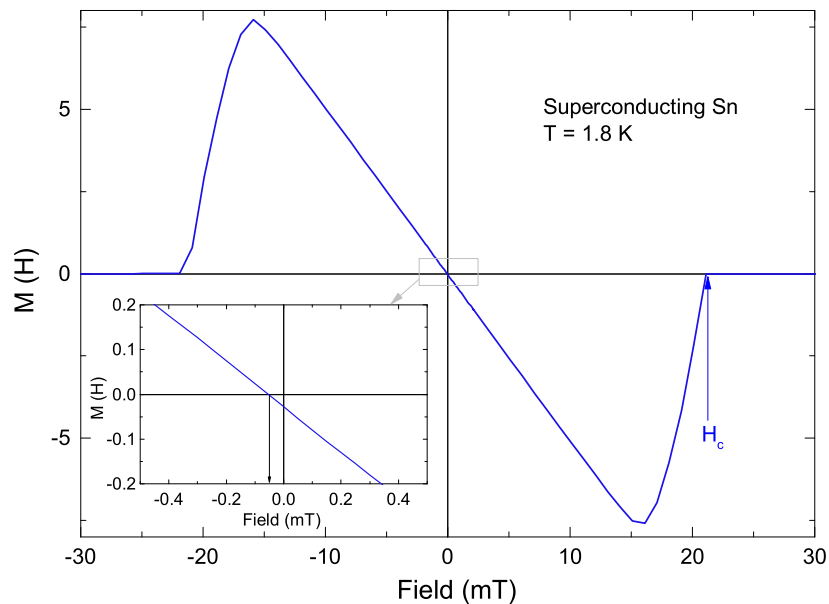


Figure 3.2: Superconducting isotherm from a sample of Sn used to determine the level of remanent field ≈ 0.5 mT.

A superconducting magnet can apply fields of up to ± 7 T. There are two operating regimes for the applied field, using more or less sensitive power supplies for the “low field” and “high field” regimes, respectively. For low fields, it is possible to operate at a field spaced resolution of ~ 0.05 mT, where the remanent field is on the order of 0.5 mT when the system is at its “zero-field” setting. This was tested

by measuring the superconducting response of a sample of tin and identifying the offset in $M(H)$ at the notionally zero field - see figure 3.2.

The superconducting detection coils are arranged in a *second-order gradiometer* configuration, whereby two wound-coils are sandwiched between two single counter-wound-coils (seen in the left-hand side of figure 3.3.) This arrangement makes the pick-up coils robust against any relaxation in the applied field from the magnet, as the flux changes in the central coils is cancelled by those on the outside. The introduction of additional coils would make the detection even more robust, although there is a tradeoff between the added stability and the increased complexity in interpreting the shape of the signal.

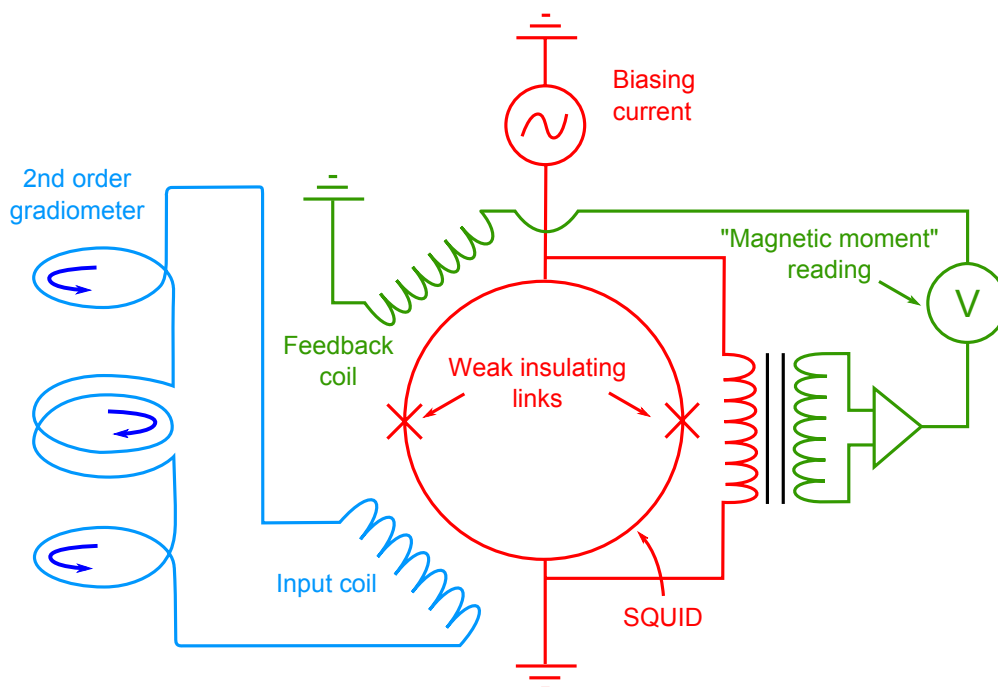


Figure 3.3: Schematic of squid and coilset [1].

The pick-up system is coupled to a SQUID, a particular arrangement of Josephson junctions¹, whose IV characteristics are very sensitive to the local magnetic flux. As in the schematic shown in figure 3.3, a superconducting loop is formed which

¹The Josephson junction is named after Brian Josephson, who won a Nobel prize for his prediction of the mechanism by which a supercurrent may tunnel across a weak insulating link - the junction - in the absence of an applied voltage.

is broken in two places by weak insulating links. The magnitude of the Josephson currents passing through the links depends on the difference in superconducting phase across the junctions, which in turn is dependent on the flux enclosed by the loop.

During a measurement, the sample is tracked up and down through the gradiometer, which induces supercurrents to flow within the coils. The pick-up circuit is coupled inductively to the SQUID via another coil (shown in the dotted blue line of figure 3.3) such that this other coil generates a flux which is injected into the SQUID loop. This “secondary” magnetic flux then affects the Josephson currents which tunnel through the insulating links². Above a critical current I_c such an arrangement of junctions will show a voltage across it. In operation, a biasing current with $I > I_c$ is applied through the SQUID, such that a voltage appears across its ends. The magnitude of this voltage is related to the flux passing through the SQUID, and therefore the sample in the pick-up coils. By measuring this voltage we can ascertain the corresponding magnetic moment of the sample.

The ultimate sensitivity of such a device is ultimately governed by the magnitude of the flux quantum $\Phi_0 = h/2e$, although for such a magnetometer as this we can in practice typically measure signals down to around 10^{-9} emu.

3.1.2 Fitting the SQUID voltage

For an ideal dipolar point-like sample, the output voltage of the SQUID as a function of the sample’s vertical position $V^I(z)$ can be modelled exactly [1]. Hopefully, in performing a scan with a real sample, the voltage put out by the SQUID $V^R(z)$ would bear some resemblance to $V^I(z)$, such that we can fit to $V^R(z)$ with $V^I(z)$ and determine the magnetic moment of the sample μ . Typically - in the case of the Quantum Design MPMS, for example [45] - this is done by the fitting algorithm within the software identifying a feature in the total scan $V^R(z)$ which most resembles $V^I(z)$, and then least-squares fitting the function around this point, thereby establishing $\vec{\mu}$.

²The SQUID itself is highly shielded from the field of the magnet, and as such only sees the flux associated with the pick-up coils.

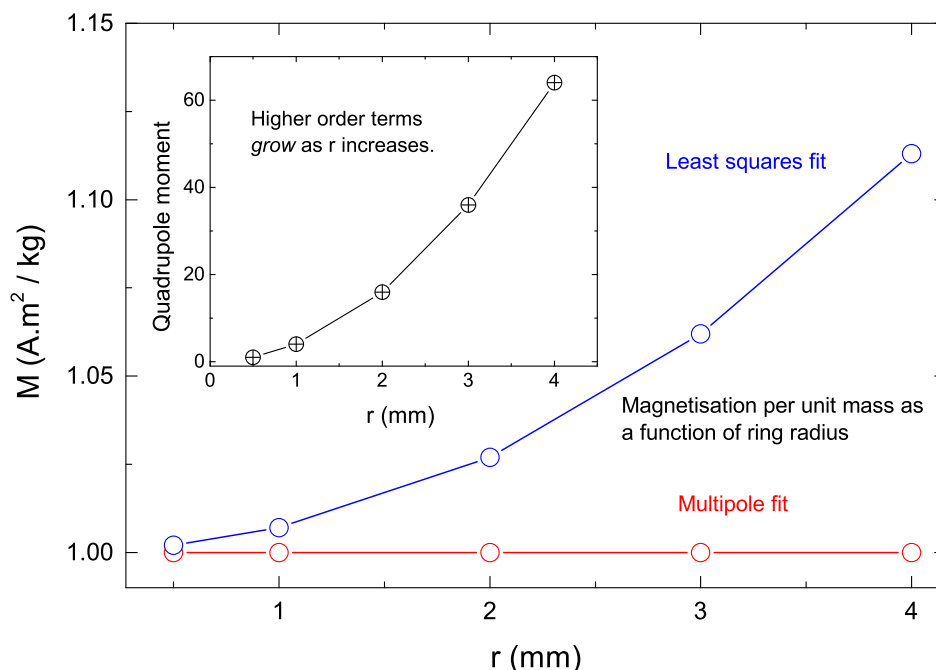


Figure 3.4: Comparison of the magnetisation per-unit-mass for conducting rings of varying radii r , for a least-squares dipole fit and the multipole-expansion fit. The multipole method is far less sensitive to the sample geometry than the least-squares fit. The inset shows how the first-order term of the expansion subsumes the influence of the geometry, growing as r is increased.

The S700X susceptometer does not fit the moment in this way. Instead of *choosing* an arbitrary portion of $V^R(z)$ to fit to, it *always* assumes that the sample is centred in the middle of the scan. Next, the output voltage $V^R(z)$ is fit not only to $V^I(z)$, but also a weighted summation of its derivatives. This is known as a “multipole” fit, and is given by:

$$V(z) = \sum_{i=0}^n c_i \frac{d^i V^I(z)}{dz^i}, \quad (3.2)$$

where the coefficients c_i are determined via *singular value decomposition*. The benefit of this method is two-fold. In the first case, it is far less sensitive to the influence of sample geometry due to demagnetising fields [1], or samples not properly centred in the coils [46]. The pick-up coils are sensitive to both of these effects and without careful treatment of $V^R(z)$, artifacts can arise in data. The extra terms in equation 3.2 represent the higher-order moments of the sample -

quadrupole, octopole and so on - which may change with sample geometry, but should not affect the dipole contribution³.

The benefit of this procedure is shown in figure 3.4, which shows the calculated moment from a series of conductive loops, using the least-squares fit and the multipole method. The main figure shows the magnetisation per unit mass for loops of different size, which - one would expect - should remain constant for any sized loop. As can be seen, the multipole method is not sensitive to the changing geometry of the rings, whereas the least-squares fit is. In contrast, the inset shows how the first-order term of equation 3.2 changes as r increases, which does seem to grow. The $i > 1$ terms in the summation *absorb* the influence of the sample geometry and/or mislocation, resulting in a better fit of the dipole contribution.

3.1.3 Sample mounting and background subtraction

Given the extreme sensitivity of the pick-up coils, it is crucial any background magnetic signals are minimal, and as such great care must be taken in choosing a sample holder. For three “up/down” scans, the susceptometer should achieve a standard error of around 0.01% on the calculated moment. Whilst it is true that the overall influence of the sample holder can be subtracted after the measurement, the level of scatter in the final data will remain unaltered.

The most common sample holder in SQUID measurements tends to be a plastic straw, where the sample is wrapped in PTFE tape and held within a gel capsule. Whilst this method is not unreasonable, weak diamagnetic contributions from each of the straw, the capsule and the PTFE still remain in the measured signal [47]. Whilst for strongly ferromagnetic materials, or superconductors, the magnetic response of these materials are irrelevant, they can become significant when measuring samples with low magnetic susceptibilities and/or in large applied fields.

³Obviously, the influence of these multipole effects is diminished as the radius of the pick-up coils increases. As the sample becomes more “point like” with respect to the gradiometer, the particular shape of the sample has less influence, and the higher-order terms in such an expansion will become attenuated and the dipole contribution will dominate.

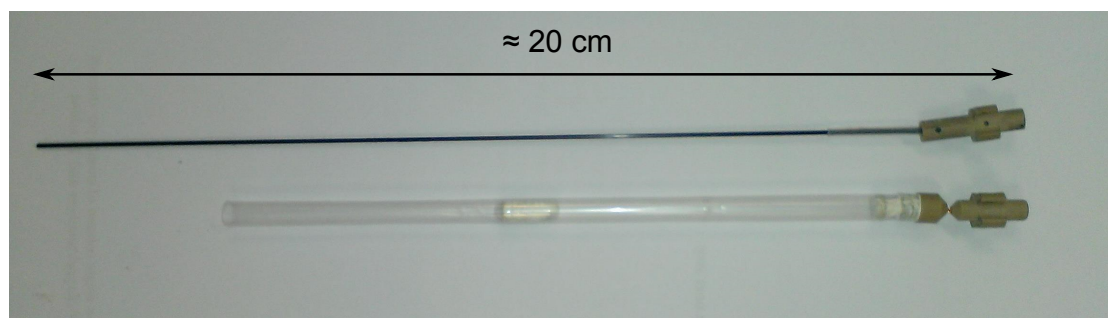


Figure 3.5: Carbon fibre reinforced epoxy resin sample holder (above) and plastic straw/gel capsule/PTFE sample holder (below).

For example, in figure 6.4 from chapter 6, some DC magnetisation measurements are shown from the system $(\text{Ca,Sr})_3\text{Ir}_4\text{Sn}_{13}$, made to investigate magnetic anisotropy. These compounds have very low magnetic susceptibilities⁴, such that it was necessary to apply around 1 T of field to induce a measurable signal. In this case, the straw proved totally inadequate, as by 1 T the signal from the sample was wiped out completely by the sample holder. Instead, a carbon fibre reinforced epoxy resin rod was used, with the sample stuck on with superglue⁵. This has proven itself to be a far superior sample holder.

Figure 3.6 shows the magnetic response of the carbon fibre stick and the plastic straw/capsule/PTFE as a function of temperature and applied field. Quite evidently, the carbon fibre rod gives a magnetic response which is *orders of magnitude* less than the straw/PTFE/capsule⁶. The advantage rests not only with the enormously reduced magnetic background, but also in the ability to orient the sample on the stick with precision, making studies involving sample orientation with respect to the field/pick-up system far easier.

⁴ $\chi_m \approx 10^{-4} \text{emu.mol}^{-1}$ [38]

⁵Cryanoacrylate.

⁶As described in the caption of figure 3.6, the carbon fibre rod in this test had a film of superglue at its centre, similar to the amount used during a run, and the plastic straw contained the 39 mg gelatin capsule and 140 mg of PTFE tape, also similar to that which would be used in a run

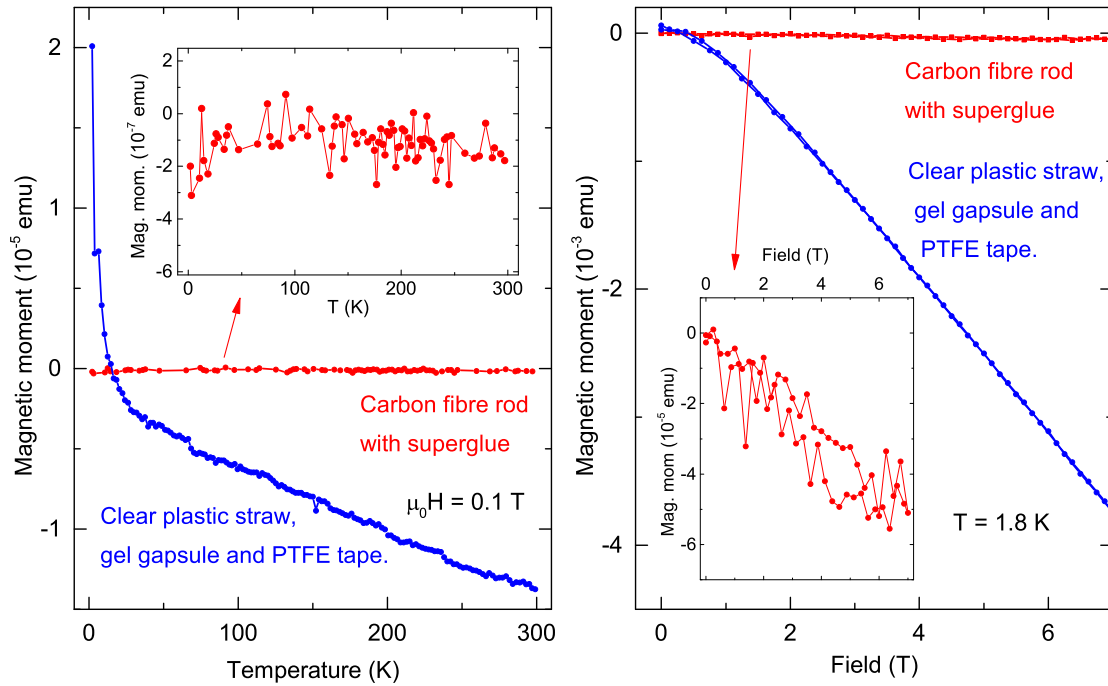


Figure 3.6: Comparison of sample mounting methods. The blue traces are from the straw shown in figure 3.5 which has length 15cm, and is holding a 39 mg gelatin capsule 7 cm along its length, containing 140 mg of PTFE tape. The red traces correspond to the carbon fibre sample holder, also shown in 3.5, which has had a film of superglue coated onto it, a similar amount to that which would be used in measurement.

3.1.4 ^3He Insert

To extend the temperature range of our measurements down to 275 mK, the system is equipped with a ^3He insert. ^3He has an odd number of nuclei, meaning that its atoms obey *fermionic* rather than *bosonic* statistics. The lower mass of the nucleus gives a lower boiling point, and the differing quantum statistics avoid the superfluid transition - at least not until *very* low temperatures [48] - both of which render it more useful as a coolant. Unfortunately, owing to its scarcity and cost we cannot use it with as much abandon as ^4He , so more subtle experimental approaches are necessary.

The ^3He probe for the magnetometer consists of an enclosed ^3He space, which couples thermally to the sample via a silver sample holder, which is held in an

evacuated copper can, as shown in figure 3.7. The ^3He space is coupled to the VTI via a weak thermal link, such that we are able to cool the gas to 1.7 K, whilst the sample is totally decoupled from the cryostat (except indirectly through the ^3He). The sample is held in place with a small amount of apiezon “N” grease, which improves the thermal link with the ^3He bath. Care must be taken when measuring samples which are strong thermal insulators, as the lack of exchange gas within the sample space means that all of the cooling takes place through the contact with the silver sample holder. When this becomes an issue, samples can be crushed, mixed with Ag powder and then sintered into a pellet with an improved thermal conductivity.

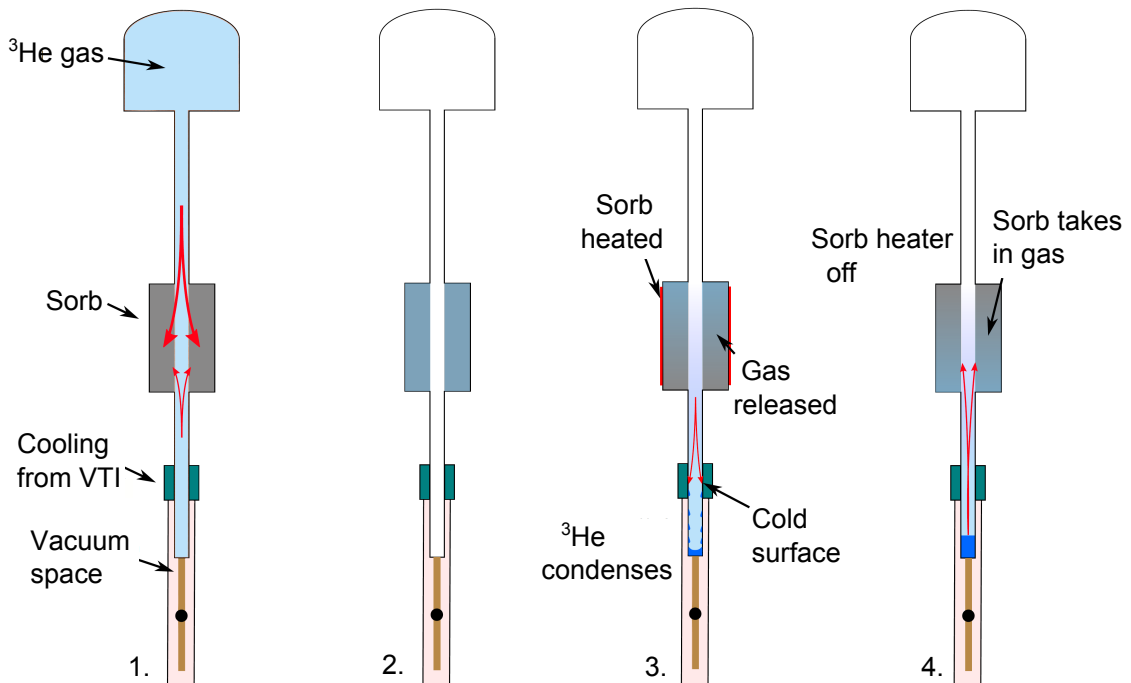


Figure 3.7: Schematic showing the cycle by which the ^3He insert achieves 275 mK.

Cooling within the insert occurs evaporatively, as in the main cryostat, except here we use a *sorption pump* rather than an external mechanical one. The pump comprises activated charcoal which adsorbs gas particles onto the surfaces of its internal microstructure. The charcoal acts somewhat like a sponge, albeit one whose ability to “sponge-up” ^3He gas is dependent on its temperature. At low

temperatures, the charcoal draws the gas inside itself until it reaches saturation, and as the temperature increases it gradually “gives up” more and more of the gas back to the ^3He space. A schematic showing the operating procedure to reach 275 mK is given in figure 3.7 which comprises the following steps:

1. After the sample is mounted and the can evacuated the probe is inserted to cool. As the insert cools (through the cold surfaces shown in turquoise), ^3He is drawn from the inner space onto the internal surfaces of the charcoal.
2. At base temperature, the sorbs become fully saturated with ^3He , having drawn in most of the gas.
3. Heaters ramp up the temperature of the charcoal, resulting in ^3He being rereleased. The gas subsequently condenses onto the cold surfaces, which are at the VTI temperature $T = 1.8$ K. A puddle of liquid ^3He forms at the bottom of the insert.
4. The sorb heaters are ramped back down to base temperature, such that the charcoal readsorbs the remaining ^3He gas back inside itself. This results in a reduction in pressure within the probe, causing the boiling point of the ^3He to drop: the puddle and by extension, the sample, drop to a temperature of 275 mK.

The probe is able to maintain its base temperature (275 mK) for around 2.5 - 3 hours before it begins to warm again. The hold time is dictated by the size of the ^3He puddle obtained in stage 3 before the sorbs are ramped back down. A three hour wait on stage 3 appears to provide an almost optimal hold time, which is crucial when performing field sweeps at base temperature. Once the liquid has boiled off completely, the insert cannot get any lower than the VTI temperature, and so the process must be repeated again.

3.2 DMS

A cryogen-free demagnetising cryostat was used to carry out the transport and AC-susceptibility measurements.

3.2.1 Adiabatic demagnetising refrigeration

The DMS (Dryogenic Measurement System) is a commercial cryogen-free cryostat which uses adiabatic demagnetisation refrigeration (ADR) to cover a measurement range from room temperature down to 100 mK. A two-stage cryocooler driven by a compressor is able to precool the system to 4 K, before the ADR cycle which achieves base temperature. The probe sits within an evacuated can which is placed inside the cryostat tube. The tube is held at a slight over pressure of ^4He such that it remains “dry” - free of air which would otherwise freeze onto the surfaces of the interior. This actually results in a build-up of liquid ^4He at the bottom of the tube, which helps anchor the can thermally to the base temperature of the cryostat. The probe itself is coupled thermally to the can via spring-loaded “buttons”, which push against its interior when the probe is twisted into position. The sample and demagnetising magnets can both provide up to 7 T of field. A cross-section of the cryostat is shown in figure 3.8. [49].

A paramagnetic salt pill which is attached to the very bottom of the probe draws out the remaining heat to reduce the temperature of the sample from 4 K to 100 mK. The salt pill is a paramagnet, containing an ionic lattice of highly degenerate local moments. In zero magnetic field, the moments are fully randomised which results in a full magnetic entropy per site of $S_m = k_B \ln(2J + 1)$, whilst in the presence of an applied magnetic field, more and more moments will tend to coalign along the direction of the field, which *quenches* the magnetic entropy. The salt pill and sample stage may be coupled or decoupled to the cryostat - which acts as a reservoir held at 4 K - via a mechanical *heat switch* which may be closed (coupled) or opened (decoupled).

Figure 3.9 shows the entropy profile as a function of the temperature during the

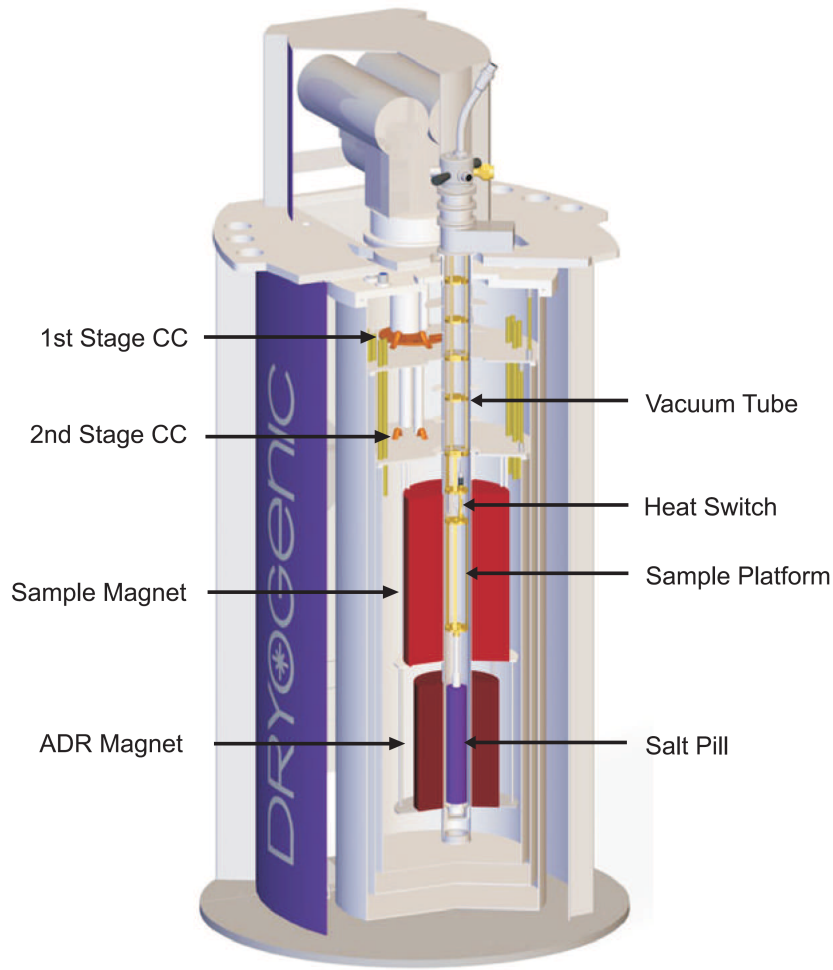


Figure 3.8: Cross-section schematic of the DMS [49].

demagnetising cycle. The salt-pill and low-temperature stage (LTS) are cooled to 4 K with the heat switch closed, before the demagnetising field is ramped up. The field is increased to its maximum (typically ~ 6.5 T), and the salt pill moments become aligned. The heat switch is then opened - decoupling the LTS from the reservoir - and the demagnetising field is ramped back to zero, re-randomising the spins. As the pill/LTS is now effectively isolated, its entropy must remain constant throughout the ramp. Consequently, as the local moments randomise, their increase in entropy is matched by a *reduction* in the entropy associated with their thermal motion - they slow down, and the system cools to 100 mK. The ability of the LTS/salt pill to stay at base temperature is dictated by how well we can

decouple it from the “universe”, and so both are protected from thermal radiation by reflective shields, along with LTS being suspended by thermally insulating Kapton supports once the heat-switch has been opened. In practise, we can hold the sample below 500 mK for around 7 hours before the system begins to warm up. Low temperature thermometry takes place via a semiconducting ruthenium oxide sensor, whilst a Cernox sensor covers the high temperature range.

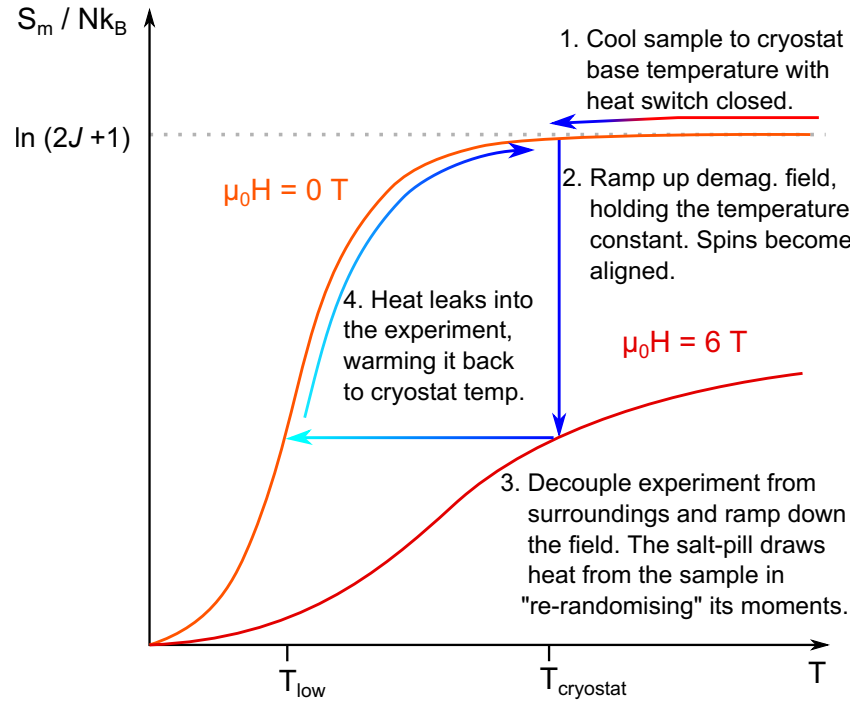


Figure 3.9: Entropy profile of the salt pill during a demagnetisation cycle.

Experimentally, the resistive and AC-susceptibility measurements are very similar. In both cases, an AC excitation current is driven through a part of the set-up, and the corresponding in-phase (or out-of-phase) AC voltage response is measured.

Figure 3.10 shows the arrangement for a “four-point” resistivity measurement. Four contacts are made to the sample, approximately in a line, with the outer two contacts passing a current I through the sample, and a potential difference V measured across the inner two contacts.

The current density \vec{J} within the sample along the i -axis is given by Ohm's law:

$$J_i = \sigma_{ij} E_j \quad (3.3)$$

where σ_{ij} is the conductivity tensor and E_j is the electric field within the sample along the j -axis. For the geometry in figure 3.10 - if the sample is taken as homogeneous and we assume a totally uniform electric field between the voltage contacts - this relation reduces to⁷:

$$V = \frac{\rho IL}{A}, \quad (3.6)$$

where the resistivity ρ is the inverse of the conductivity σ . So, to maximise the measurable signal - and consequently the signal-to-noise ratio - we can either increase the excitation current I or make our sample thinner and longer (reduce A/L). Increasing the excitation current is helpful, but this must be matched against the resulting ohmic heating which takes place within the sample, growing as I^2 . Samples are ideally as long as possible - although the length is generally dictated by the original dimensions of the crystals themselves - and then polished down to a very fine thickness⁸

In an AC susceptibility measurement the sample is placed within a measurement coil, and is driven by a small AC magnetic field. By Faraday's law of induction, the voltage V measured across the ends of the coil is dependent on the permeability $\mu = \mu_0(\chi + 1)$ of the volume it encloses, such that we can determine the magnetic susceptibility χ from the magnitude of V . From an excellent review of AC-susceptibility measurements by Nikolo [51] - a driving field of frequency f and

⁷In the uniform field case, the current density reduces to:

$$J = I/A, \quad (3.4)$$

and the electric field to -

$$E = V/L, \quad (3.5)$$

such that a simple rearrangement of equation 3.3 produces equation 3.6.

⁸Focussed Ion Beam (FIB) lithography techniques have recently been exploited to make miniature four-point measurements [50] such that samples with dimensions on the order of $1 \mu\text{m}$ may be measured, where the signal from such a small sample can be boosted by precisely cutting them into novel shapes which maximise the geometric factor L/A .

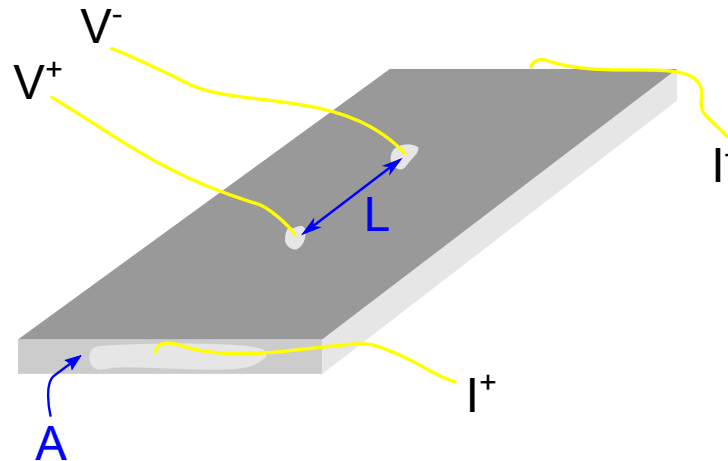


Figure 3.10: Schematic of the sample and field arrangement in this four-point resistivity measurement.

an amplitude H_{ac} should produce a voltage V across the coil given by:

$$V = \frac{vfH_{ac}\chi}{\alpha}, \quad (3.7)$$

where v is the sample volume and α is the coil constant, which is dependent on the dimensions of the coil. Generally, due to the lagging of the magnetisation behind the driving field, χ will have both real and imaginary components:

$$\chi = \chi' + i\chi'', \quad (3.8)$$

where the real part of χ reflects the actual magnetic susceptibility, whereas the imaginary part describes energy losses within the sample due to eddy currents and other irreversible processes.

In both cases we use *phase-sensitive* detection, whereby a lock-in amplifier provides an excitation signal⁹ at frequency f , and then is able to detect the corresponding component of the response at the same frequency. The lock-in acts somewhat like a band-pass filter centred on the frequency f with a quality factor Q which is determined by the time constant setting.

⁹The “reference signal”.

3.3 Pressure

When applying pressure to a crystal lattice, the lattice shrinks in accordance with its bulk modulus, which can have a profound influence upon the electronic structure of a material.

3.3.1 Miniature anvil cell

An anvil cell generates a hydrostatic pressure environment by the compression of a small volume of fluid, which is held within the walls of a metal chamber. The “chamber” comprises a hole which has been drilled through the centre of a disc of a ductile metal - the *gasket* - which holds the pressure fluid, and forms the sample space. The “anvils” consist of two blocks of very hard material, each of which have a smooth flat face known as the “culet”. The hole in the gasket is then pinched between the culets, such that their walls flow inwards, reducing the volume of the sample space and resulting in a build-up of pressure within the fluid. One anvil is held fixed, whilst the other is attached to the end of a “piston”, and they are driven towards the other by a hydraulic ram. A schematic of this process is shown in figure 3.11:

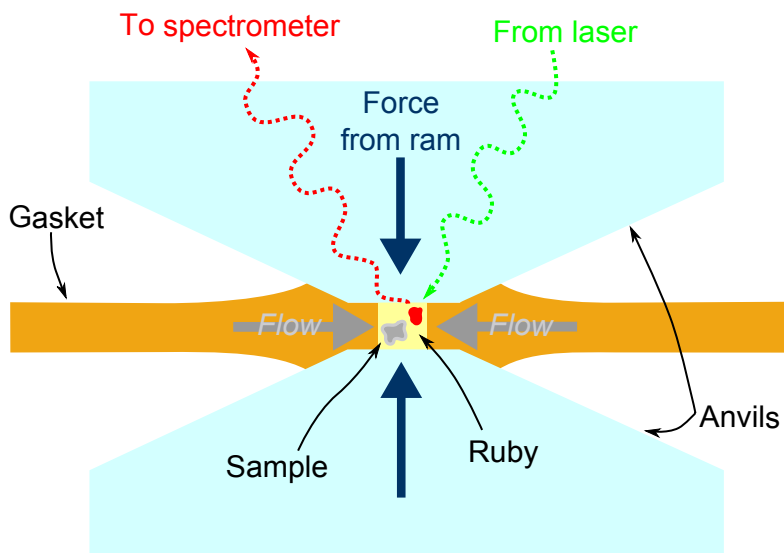


Figure 3.11: Operating principle of the anvil cell.

Dunstan [52–54] has given a complete and comprehensive discussion of the operation of the anvil cell, with considerable focus on gasket design/preparation. He finds that whilst the material used for a gasket must be sufficiently ductile that it may flow in a way which creates an insulated and stable environment, it must also be tough enough to withstand the enormous forces being generated by the pistons. As the central portion of the gasket - see figure - flows into the centre, compressing the “hole”, the portion of the gasket which sits just outside the central region provides *massive support* to the material in the centre. This is shown in fig. 3.11 as a build-up of material outside of the central gasket region. The cumulation of gasket material around the centre acts as a buffer, forcing the interior of the gasket to extrude inwards, pressurising the fluid (and sample) within.

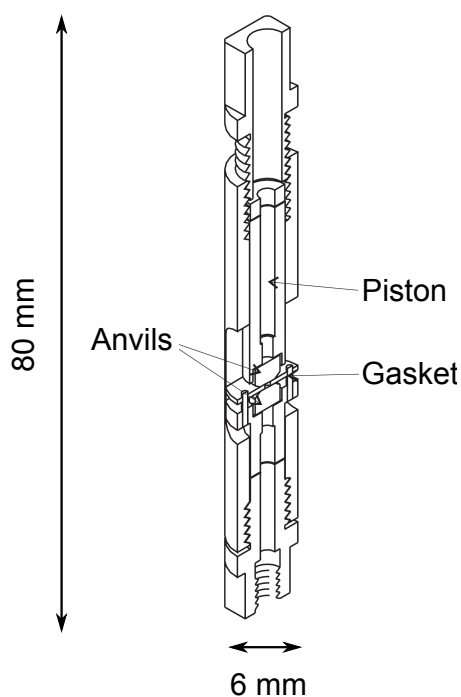


Figure 3.12: Miniature anvil SQUID cell, from [55].

Whilst diamond anvil cells have been commonly used in transport [37], AC-susceptibility [56] or NMR measurements[57], in this thesis we present DC susceptibility data from a miniature anvil cell (MAC). This cell was designed within the Quantum Matter group with the expressed purpose of use with a commercial

SQUID magnetometer [55] - it is shown in figure 3.12.

As the pick-up coils in the magnetometer see the total flux from both the pressure cell *and* the sample, it is crucial that the magnetic background from the cell is as low as possible. In fact, it is somewhat amazing that such a set-up is able to give any useable data at all, given the orders-of-magnitude difference between the mass of the ≈ 20 g cell and the $< 0.1 \mu\text{g}$ sample. Yet, with a suitable choice of materials for the cell components, such cells have been shown to be effective in studies of superconductors [58] and ferromagnets [59]. A high-purity copper titanium alloy (97% Cu, 3% Ti) is used for the cell body, due to its very low magnetic response. The alloying ratio is chosen such that the *paramagnetic* susceptibility of the titanium matches the *diamagnetic* susceptibility of the copper over a wide temperature range. Another alloy of copper - BeCu - is used for the gaskets, owing to its superior mechanical strength. The anvils themselves would ideally be made of ultra-high-purity diamond, whose strong covalent structure gives it an unmatched “hardness”. In reality, there is always a tradeoff between the benefit of the robustness of diamond and the significantly lower cost of a synthetic alternative. Consequently, our SQUID cell uses Moissanite (SiC) anvils, rather than diamond, and are more than adequate for the pressure region < 100 kbar [60].

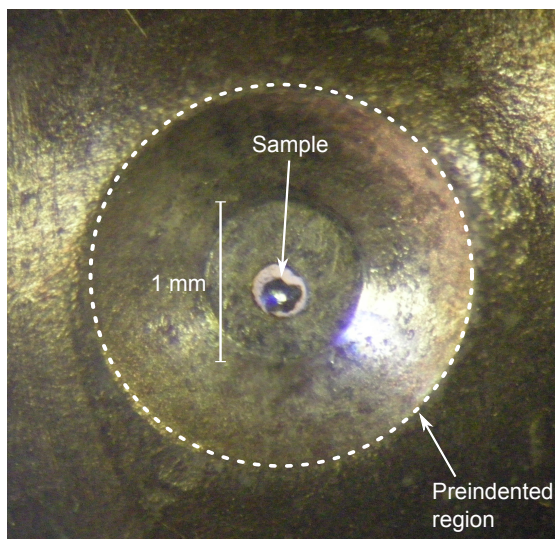


Figure 3.13: Preindented region of the gasket with a sample in the sample space.

Prior to operation, the gasket undergoes a preindentation process, whereby the thickness of the central portion of the gasket is reduced to an appropriate thickness. A gasket which is too thick at the beginning of the run must change dimension considerably during the course of an experiment, which can make the gasket prone to failure¹⁰. For our gaskets, the final thickness is typically on the order of $100\mu\text{m}$, with a $400\mu\text{m}$ diameter hole drilled through its centre. Every effort must be made to ensure that the walls of the drilled hole are as sharp and as clean as possible, as any irregularities or asymmetries can serve as the nuclei for structural instability. After preindentation, the gasket is cleaned ultrasonically in ethanol before being heat-treated at 370°C for 15 minutes to harden it.

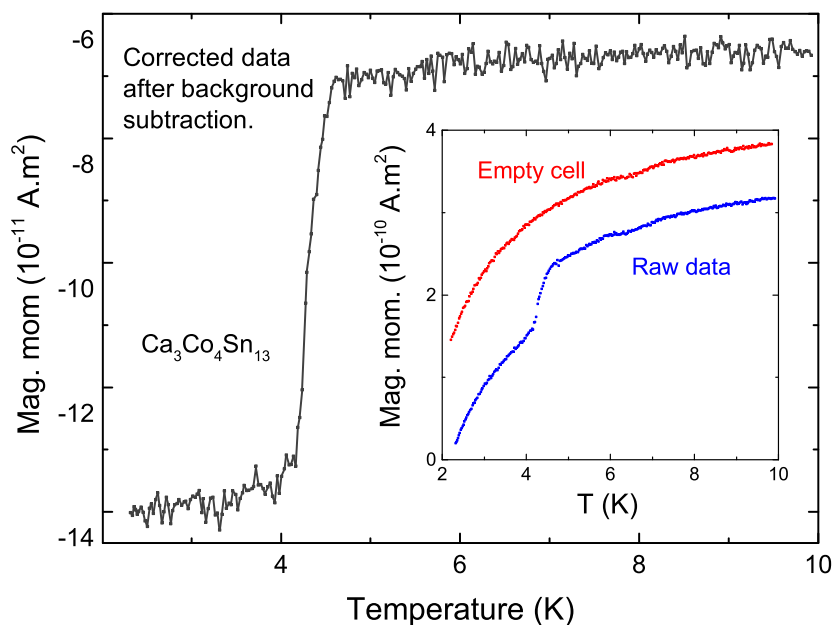


Figure 3.14: Main: Raw $M(T)$ data along with the empty cell run. Inset: Data following background subtraction - a clear superconducting transition is present.

The gasket sits upon the lower anvil in the cell and is held in place with small blobs of “Double Bubble” epoxy. Once dry, the sample and manometer can be placed within the sample space along with the pressure medium. Figure 3.13 shows a gasket after preindentation with a sample loaded. Consideration must also be made in

¹⁰“Failure” here means that the walls of the sample space collapse, or the gasket splits slightly causing pressure fluid to leak out, or in the worst scenario the complete destruction of the anvils.

the appropriate choice of pressure medium. There are numerous review articles on this subject [61, 62], and generally there is a balance between pressure media which are easy to load experimentally, but may result in non-hydrostatic conditions at high pressure - glycerin, Daphne 7474, say - or more technically challenging fluids which give better pressure conditions in the high pressure limit - nitrogen, argon and so on. For the pressure studies in this thesis, glycerin was used as a pressure medium, which is adequate for the pressure regime < 50 kbar [61].

As a brief side-note, figure 3.14 shows how the magnetic background from the cell is subtracted after a measurement. Namely, by removing the sample from the cell, remeasuring the empty cell, and then subtracting this from the raw data. As can be seen, this can work quite well.

3.3.2 Manometry

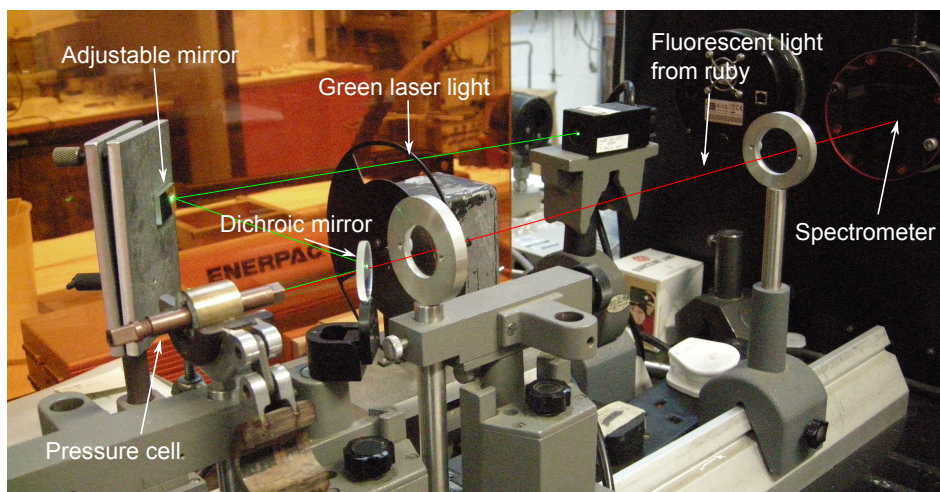


Figure 3.15: Layout of the optical bench used for the ruby fluorescence technique.

For pressure to be a useful tuning parameter we must be able to determine it with convenience and accuracy. A manometer is always included in the high pressure space to give out information about the pressure conditions within. For cells with optical access to the sample space, a ruby chip is included, and its optical properties as a function of the pressure can be tracked. Where no optical access is possible - in the case of a piston-cylinder cell, say - a superconducting element (usually

tin or lead) is included, whose pressure dependence of $T_c(P)$ is well-known. Given the bulk nature of the SQUID cell measurement, the tin or lead method is far from ideal. A large magnetic background becomes present in the data beneath the critical temperature of the manometer, which can spoil data - particularly if one is looking for features in the vicinity of the manometer transition¹¹.

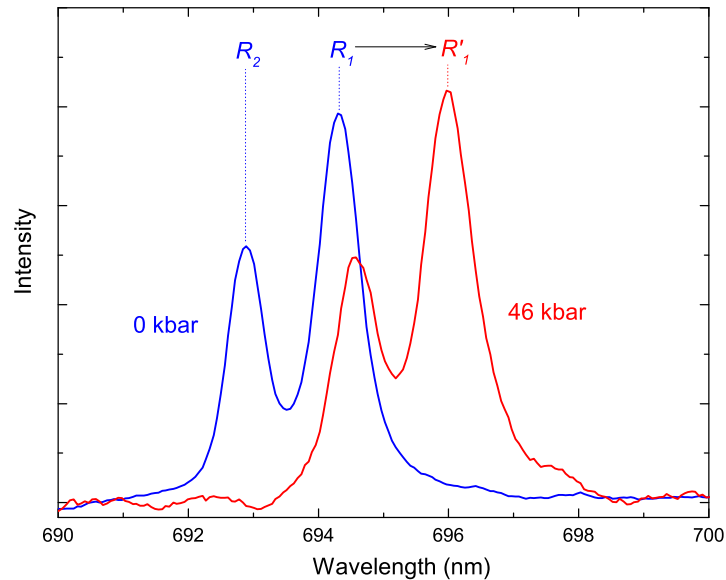


Figure 3.16: Pressure dependence of the characteristic spectra of a ruby chip.

The MAC cell allows for optical access, and the ruby technique is used in preference. This allows for rapid adjustment of pressure, by successively moving between the ram and the optical bench. It also allows for the pressure to be determined at room temperature, rather than having to cool the sample in a cryostat to find the tin/lead transition.

Due to the presence of chromium (IV) impurities, the fluorescent spectra of ruby shows two characteristic peaks at specific wavelengths R_1 and R_2 . The location of these peaks is strongly pressure dependent [63], shifting to higher wavelengths as it is increased. The optical bench which is used for pressure determination is shown in figure 3.15, whereby green laser light is directed by a series of adjustable mirrors

¹¹This is *not* the case in a resistive measurement, where the tin or lead is totally decoupled from the sample measurement, such that they can be both measured totally independently and without interference

to the interior of the cell, causing the ruby chip to fluoresce. The fluorescent light then leaves the cell, passing back through one of the mirrors - which is *dichroic* such that it reflects the green light, but transmits the red - and is focussed by two lenses into the eye of the spectrometer. The signal from the ruby is optimised by successive adjustment of each of the controls moving the cell and mirrors, before the spectra is recorded. A Matlab function is then used to extract the corresponding pressure from the peak location. An example of real spectra at ambient pressure and at 46 kbar is shown in figure 3.16.

Chapter 4

CeAgSb₂

Here we investigate the ferromagnetic $4f$ system – CeAgSb₂ with the aim of driving it towards a ferromagnetic quantum critical point. We detail the pressure and field dependence of the magnetic order, with particular focus on the critical fields and pressure required to suppress the ferromagnetism totally.

4.1 Ferromagnetism in a $4f$ system

The experimental realisation of the ferromagnetic quantum critical point (FMQCP) has been made difficult due to the reluctance of many FM transitions to remain second-order down to the lowest temperatures. Initial focus on the behaviour of weakly ferromagnetic d -electron systems such as MnSi [64] and ZrZn₂ [65] found that whilst magnetic order could be suppressed towards absolute zero by the application of hydrostatic pressure, in both compounds the FMQCP was evaded by the transition by becoming weakly first-order whilst still at finite temperature. This crossover marks the existence of a tri-critical point, from which sheets of metamagnetic transitions extend, accessible by the application of a finite applied field [66].

Perhaps the most dramatic example of such a scenario is found in the $5f$ ferromagnet URhGe. URhGe is a coexistent ferromagnetic superconductor with Curie

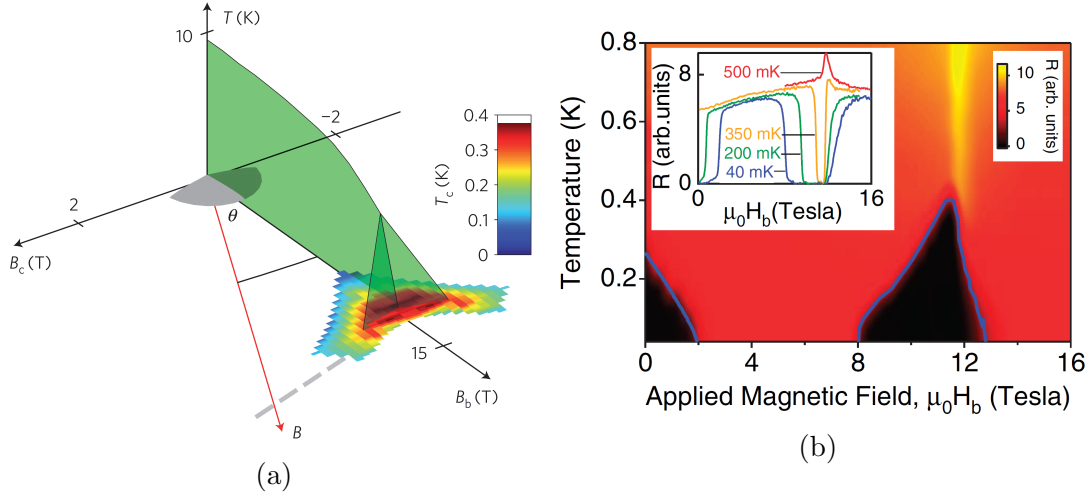


Figure 4.1: (a) Magnetic phase diagram of URhGe for two different field directions. Tricritical point can be seen at around 12 T as T_C is suppressed to 0 K, around which superconductivity grows, from [67]. (b) Reemergence of superconductivity at high fields in the proximity of the tricritical point, from [39].

and superconducting critical temperatures of $T_C = 9.5$ K and $T_c = 0.25$ K, respectively [68]. Both transition temperatures may be suppressed with a magnetic field applied along the crystallographic \vec{b} direction. As in the d -electron systems just mentioned, the line of second order transitions corresponding to $T_C(B_b)$ terminates at a tricritical point at around 12 T – shown in figure 4.1 (a) – from which two metamagnetic wings extend into B_c phase space¹ [67]. Amazingly, superconductivity is found to *reemerge* around this tricritical point, as shown in figure 4.1 (b) [39]. The applied field initially “kills off” SC at low B_b , before inducing it again at much greater fields! Although the origin of this effect is not known for certain, it has been suggested to be the result of a complicated interplay between the critical fluctuations stemming from the end-points of the sheets, and a small pocket of heavy quasiparticles whose size shrinks to zero at a topological Lifshitz transition [67].

There has been evidence of a Yb based $4f^{13}$ system showing behaviour consistent with ferromagnetic criticality². $YbNi_4P_2$ is a quasi-one-dimensional ferromagnet,

¹This corresponds to field applied in the \vec{c} direction

²Yb-based systems are analogous to Ce-based compounds: instead of having a nearly empty

with isolated chains of Yb ions coaligning below a Curie temperature of $T_C = 0.17$ K [69]. Here, a linear-in- T dependence of the electrical resistance is found over many decades, along with a logarithmic dependence of the heat capacity. Doping on the phosphorus site with isovalent arsenic (effective negative chemical pressure) suppresses T_C [70], and at a critical concentration the magnetic Grüneisen ratio is found to diverge, consistent with the approach of the FMQCP and strong associated ferromagnetic fluctuations. This is shown in figure 4.2.

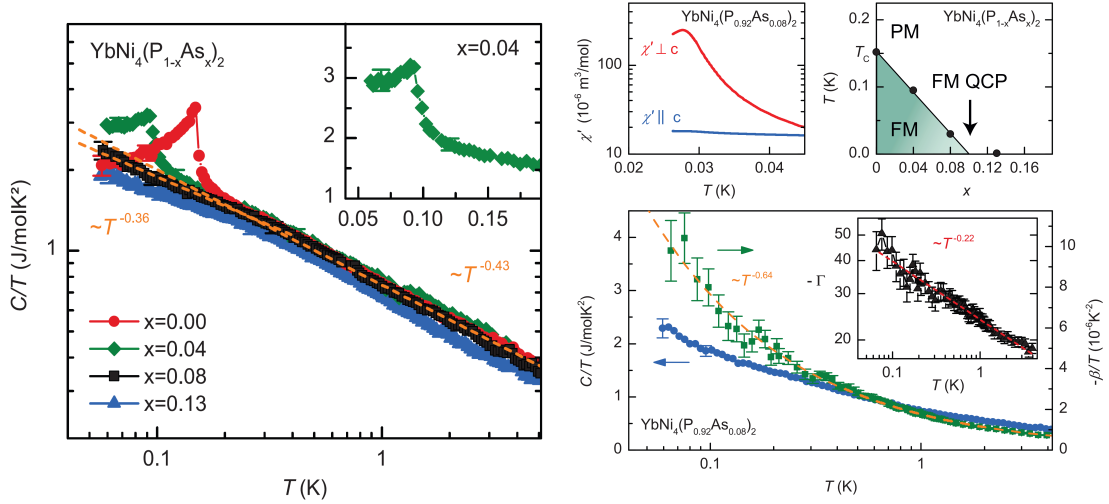


Figure 4.2: Signatures of ferromagnetic quantum criticality in the 1-dimensional system $YbNi_4(P_{1-x}As_x)_2$ at a critical doping $x_c = 0.1$, taken from [70].

It is likely that the difficulties faced by 2-D or 3-D ferromagnets as $T \rightarrow T_c$ are circumvented due to the effective low-dimensionality of the system. It is known that quantum fluctuations become enhanced as the dimensionality of a system is reduced, also becoming more prone to electronic or structural instability³. For example, in a purely theoretical limit, the Mermin–Wagner theorem [72] shows that no phase transition exists into a magnetically ordered, spontaneously-symmetry-broken state for any system with $D \leq 2$, due to the strong influence of the quantum fluctuations.

³ f shell, containing a single electron (Ce^{3+} ion: $4f^1$), they have a nearly full $4f$ shell containing a single hole (Yb^{3+} ion: $4f^{13}$.)

³See - for example - the “Peierls instability” in 1-D [71]

CeAgSb₂ is an interesting system to study in that it offers a unique possibility of realising the FMQCP in a $4f$ ferromagnet. Whilst there are now a wealth of “classical” quantum critical antiferromagnets – CeCu₂Si₂, CeIn₃, CePd₂Si₂ and so on [73] – there are as of yet no instances of a $4f$ ferromagnetic system showing critical behaviour as its magnetic order is tuned to zero temperature.

This is partially due to most intermetallic Ce-based Kondo-lattice systems ordering antiferromagnetically at low temperatures, making CeAgSb₂ somewhat unusual. It has been shown to order ferromagnetically below a Curie temperature T_C of 9.6 K⁴ and belongs to a broader family of Kondo-lattice systems forming as Ce T Sb₂, where $T = \text{Au, Ag, Pd, Cu, Ni}$ [74, 75], all of which crystallise in the ZrCuSi₂-type structure (space group $P4/nmm$ [76]) – this structure is shown in figure 4.3.

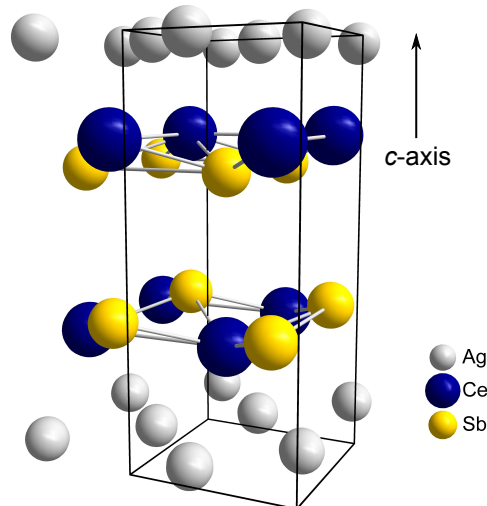


Figure 4.3: Crystal structure of CeAgSb₂. Each unit cell contains two formula units, four unit cells are shown here.

The tetragonal symmetry of the crystalline electric field (CEF)⁵ acting upon the

⁴Coincidentally, CeAgSb₂ shares the same transition temperature and ordered moment as URhGe, although whilst URhGe is orthorhombic, CeAgSb₂ is tetragonal. Also, $4f$ and $5f$ states are not exactly analogous, as can be seen from their radial distribution functions – $5f$ states are more delocalised than $4f$ states, such that they are on the boundary between local and itinerant states.

⁵In crystalline solids, the electrostatic influence of neighbouring atoms may act so as to lift the degeneracy of their sub-shells. The particular point symmetry of the site in question then

Ce³⁺ ion lifts the 6-fold degeneracy of the $J = 5/2$ ground state multiplet, creating three Kramer's doublets. The crystal field scheme has been well described from thermodynamic measurements [77] and via inelastic neutron scattering [76]. The neutron measurements have also identified the magnetic order as being unequivocally ferromagnetic, with each Ce moment oriented uniaxially along the \vec{c} -axis, albeit coupled via anisotropic exchange interactions [76, 78]. The new $|J_z = \pm \frac{1}{2}\rangle$ CEF ground state accounts for the reduced saturated moment observed in the FM phase. The excited levels (Δ_1, Δ_2) sit far from the transition temperature T_C – at 60 K and 140 K [76–78] – and as such the ordered moments in the magnetic ground-state are of an Ising-type⁶.

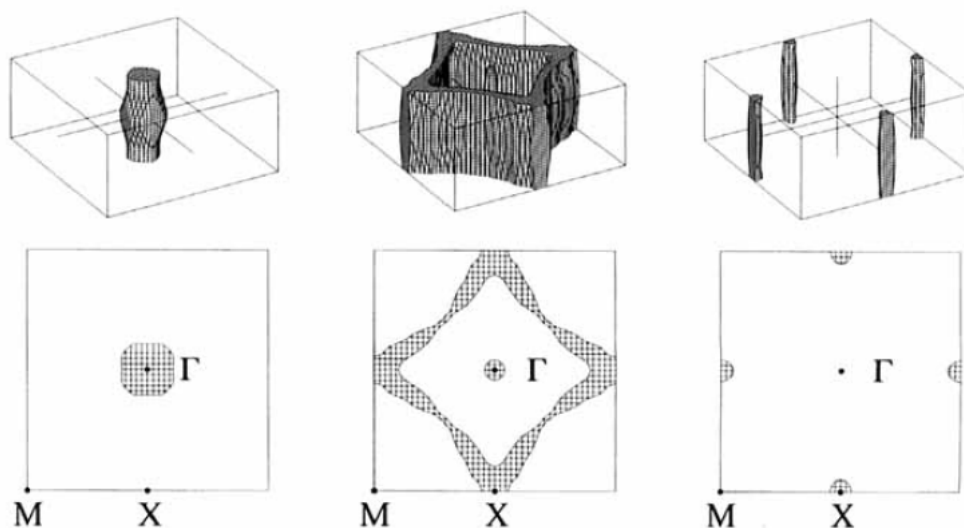


Figure 4.4: Theoretical Fermi surfaces for CeAgSb₂, matched against dHvA frequencies from [79]. The left hand figure corresponds to a hole sheet, whilst the other two are electron-like.

The Fermi surface has been probed via de Haas-van Alphen (dHvA) [79] and Shubnikov-de Haas [77, 80] measurements, revealing the presence of a large and hollow, corrugated cylindrical Fermi-surface, with a mass enhancement of around 20-30 m_e , along with smaller hole and electron pockets - these are shown in figure

determines the characteristics of the newly split levels.

⁶In the Ising model a lattice of spins are made to point in one of two directions, with an exchange interaction between neighbours which can be ferro- or anti-ferromagnetic in character.

4.4. The comparison of the Fermiology with LaAgSb₂ suggests that the 4*f* electron remains localised in CeAgSb₂; we are not yet in the heavy Fermi-liquid regime. Thermopower measurements in the literature suggest that the Kondo temperature T_K in this system may be around 60 K [81], although this seems to be at odds with the fact that the full magnetic entropy $R \ln 2$ is retained by T_C [82]. Kondo screening setting in so far above the transition temperature would be expected to have begun to quench the magnetic degree of freedom on the local moment at T_C , whereas this is not seen in thermodynamic data.

The ordered phase is populated by thermally activated ferromagnetic spin waves, which – owing to the uniaxial nature of the ordered state – are necessarily gapped. The magnons are the Goldstone bosons corresponding to the symmetry breaking which takes place at T_c [83]. This is made manifest in an exponential $e^{-\Delta/k_B T}$ dependence of the heat capacity and electrical resistivity [77, 78, 84], and can be seen explicitly in the magnon dispersion as determined from inelastic neutron scattering [76].

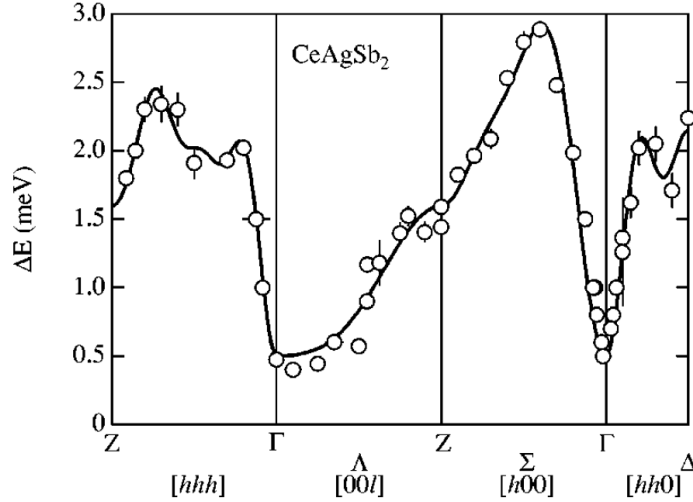


Figure 4.5: Spin-wave dispersion of CeAgSb₂ along high-symmetry directions, taken from [76].

Previous studies have attempted to drive the magnetic transition to zero temperature through application of hydrostatic pressure [84–86] and an *in-plane* tuning

field [76, 78, 84, 87]. Resistivity and specific-heat measurements found that T_C is suppressed with pressure, and appears to extrapolate to 0 K by 35 kbar. The A coefficient to the quadratic term of the electrical resistivity – which reflects the quasiparticle scattering cross-section [28] – becomes greater near the critical pressure P_c [84], a feature commonly associated with the enhanced scattering due to critical fluctuations. The residual resistivity ρ_0 is also affected in the proximity of P_c , jumping by two orders of magnitude at pressures beyond 35 kbar [86].

A magnetically ordered ground state in a Kondo lattice system means that the RKKY interaction [88] has precedence over Kondo screening at low temperatures. RKKY coupling is an indirect exchange interaction between local spins via itinerant states which promotes magnetic order. The exchange interaction takes the form –

$$\mathcal{J}(R) \sim \frac{\sin(2k_F R) - 2k_F R \cos(2k_F R)}{(k_F R)^4} \quad (4.1)$$

where k_F is the Fermi wavevector and R is the separation between local spins, meaning that it may favour co-parallel or antiparallel spins depending on the value of $k_F R$ [89]. The oscillatory nature of the RKKY term means that as $k_F R$ changes under the influence of an external tuning parameter, a ferromagnetic phase could turn antiferromagnetic before the FMQCP is reached. Indeed, this may be the case in CeAgSb₂ – Sidorov et al [84] report that the transition becomes first-order at around 27 kbar, at which point a new *antiferromagnetic* ground state sets in. It is not, however, so clear that the transition truly does turn first-order from their data as they infer this only from a change in the nature of the anomaly in $d\rho/dT$, rather than from a thermodynamic quantity such as the magnetisation or specific-heat – see figure 4.6.

The AF phase is said to persist to up to a second critical pressure P_c at around 50 kbar, although it could be that the features tracked in $\rho(T)$ become too indistinct to follow to higher pressures. A similar scenario arises in the sister compound CeAuSb₂, which is AF below $T_N = 6.8$ K [90], and cascades through a series of high- P magnetic states as the pressure is increased – see figure 4.6.

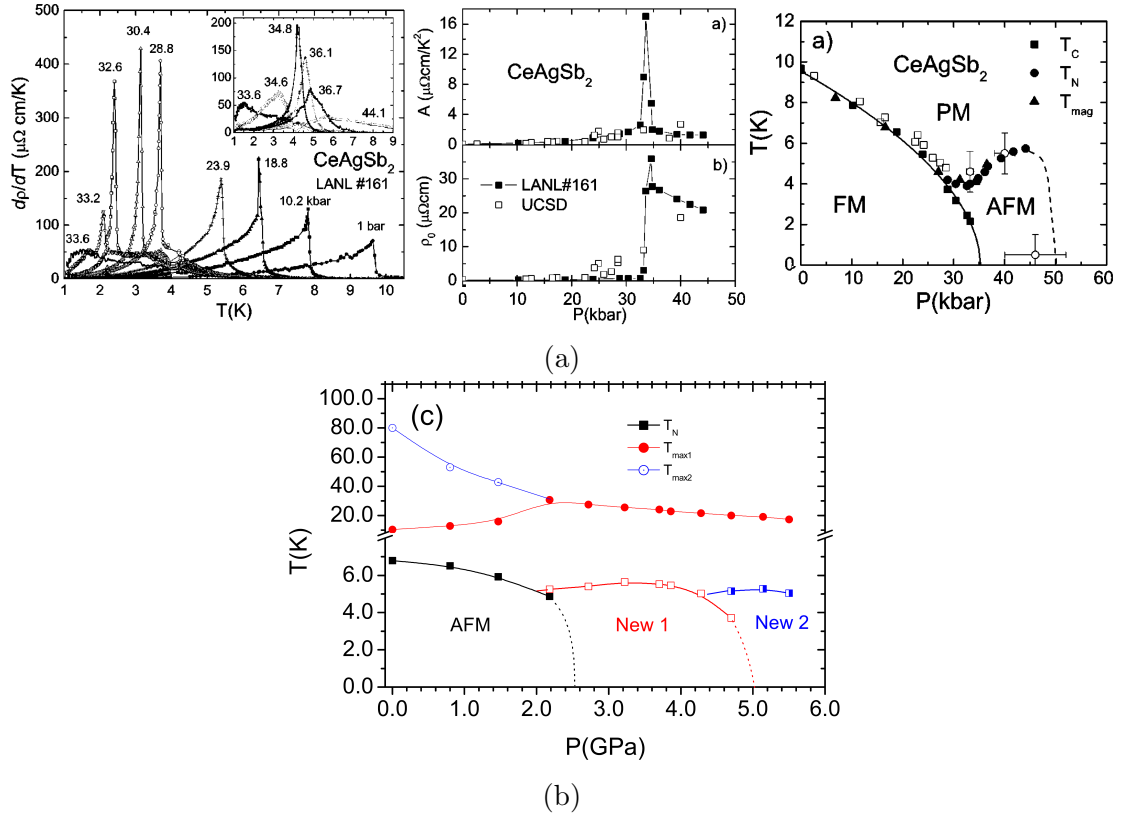
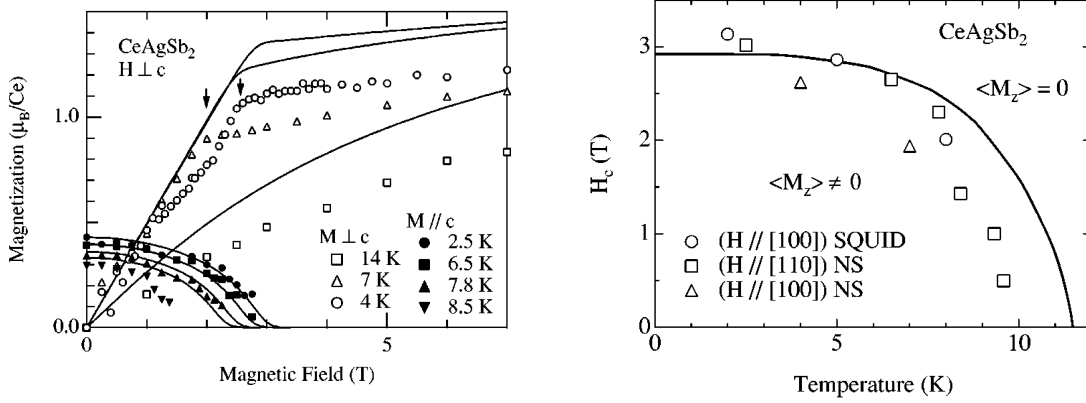


Figure 4.6: (a) From [84] - $d\rho/dT$ at a range of P , the pressure dependence of the A coefficient and the residual resistivity, and the proposed PT phase diagram. (b) PT phase diagram of $CeAuSb_2$ from [90].

$CeAgSb_2$ is made more attractive still by the sensitivity of its magnetic order to a transverse applied field. A critical field H_c of around 3 T [76] applied *in-plane* is sufficient to destroy the magnetic phase. This has been tracked via the magnetisation [87], transport [77] and most revealingly through neutron scattering measurements [78]. No critical behaviour has yet been reported near the critical field, although there is a lack of focussed low-temperature study around H_c .

Inelastic neutron scattering [76] has shown that the ordered moment along the \vec{c} -axis is suppressed continuously to zero as the transverse field is increased to H_c . They claim that the critical field corresponds to the switch from a $|+\frac{1}{2}\rangle$ ground state to a linear combination of $|\pm\frac{1}{2}\rangle$ and are able to reproduce the magnetic behaviour of $CeAgSb_2$ – shown as solid lines in figure 4.7 – via a Hamiltonian which



(a) Field dependence of the *in-plane* and *easy* moments as determined from neutron scattering.

(b) HT phase diagram showing the boundary between the ordered and the paramagnetic/spin-polarised states.

Figure 4.7: Inelastic neutron scattering of CeAgSb₂, [76].

takes into account the CEF splitting, the Zeeman interaction, and an anisotropic exchange interaction between neighbouring Ising-like moments. Again, under the influence of a transverse field, CeAuSb₂ has been shown to display non-Fermi liquid characteristics consistent with critical fluctuations at its in-plane field induced QCP [91, 92].

The motivation and approach we adopted in studying CeAgSb₂ can be summarised as follows:

1. Using a miniature-anvil SQUID cell, study the pressure dependence of the ferromagnetic phase via the magnetisation: reproduce the pressure dependence of the Curie temperature $T_C(P)$ given in the literature [84], and determine the pressure dependence of the saturated moment $M_{sat}(P)$.
2. Investigate the purported AF phase which may appear above 27 kbar – determine the pressure dependence of $T_N(P)$ and the critical pressure P_{c2} .
3. On approach to the critical pressure $P_c = 35$ kbar, look for diamagnetic signatures in the magnetisation consistent with the appearance of superconductivity (and around P_{c2} if the high pressure phase exists).
4. Using a transverse field, map out the phase boundary separating the FM and

PM states as described in [76–78] via DC/AC-susceptibility and the electrical resistivity.

5. With the DMS, make careful low-temperature measurements of the region of the HT phase diagram near the critical field H_c , to look for signatures of critical fluctuations in the AC-susceptibility and the electrical resistivity.

4.2 Synthesis and characterisation

Samples were grown in-house by Zhuo Feng from the Quantum Matter group and Prof. Takao Ebihara of Shizuoka University [93]. They were flux-grown in an excess of Sb, using high purity Ce chips (99.9%), Ag powder (99.99%) and Sb shots (99.99%). The mixture is loaded into an alumina crucible, vacuum sealed in a quartz ampoule and then melted together in the furnace. The molten mixture is heated to 1200 °C and then cooled slowly to 720 °C at 5-6, °C.h⁻¹. The excess Sb is removed by turning over the ampoule at 750 °C when the Sb is still liquid. The dimensions of the synthesised single-crystals are on the order of 1 mm × 1 mm × 0.5 mm.

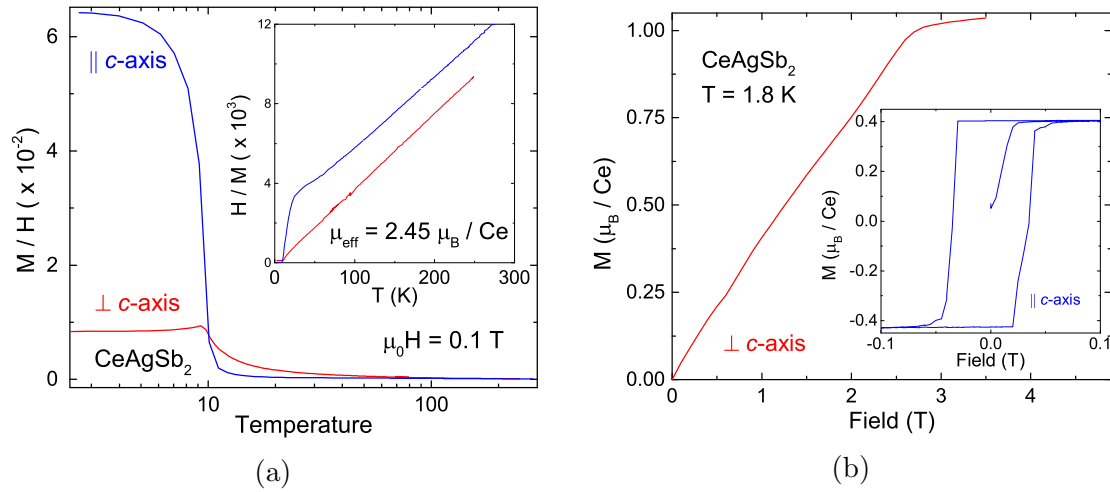


Figure 4.8: Magnetic measurements to characterise single-crystal CeAgSb₂ samples. Red traces correspond to *in-plane* measurements, whilst the blue ones are along the easy axis.

The samples cleave into platelets lying in the *ab*-plane, meaning that it is very straightforward to identify their orientation [82]. Magnetic characterisation of the samples – see fig. 4.8 – reveal a magnetic transition appearing at $T_C = 9.6$ K, whose character differs between the easy and hard directions. Isothermal field sweeps measured along the *c*-axis reveal a sharp, clear hysteresis, consistent with ferromagnetism in this direction.

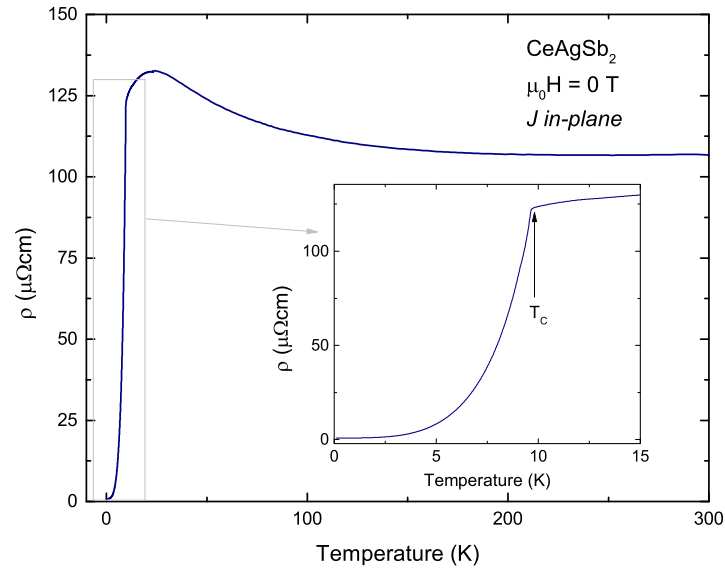


Figure 4.9: Transport measurements to characterise single-crystal CeAgSb₂ samples. Inset shows the kink at T_C corresponding to the ferromagnetic transition.

Figure 4.9 shows the temperature dependence of the electrical resistivity from room to base temperature. The trace was normalised to the values in the literature. It is weakly temperature dependent at high temperatures before an upturn, which has been attributed to the onset of the Kondo screening [77]. This Kondo screening achieves coherence at the start of the downturn shown in the inset of figure 4.9 before the sample becomes magnetic and the resistivity drops exponentially from the kink at T_C , as thermally activated magnons become frozen out [94]. The high-quality of these samples is reflected in their RRR values, in this case $RRR = 130$.

4.3 Pressure Tuning

Firstly, we investigate the influence of hydrostatic pressure upon the magnetisation $M(T, P)$ with a miniature anvil cell. The cell was set up as described in chapter 3, with glycerin used as the pressure-transmitting medium. The magnetic moment is measured along the easy c -axis, which is convenient experimentally due to the platelet-like nature of the samples. The sample was placed in the cell before the ruby, such that it lay as flat as possible on the bottom surface of the culet.

The MAC cell gives the most reproducible signal between different pressure points when the condition and position of the cell in the pick-ups remains unchanged, and also that the cell has experienced the same magnetic history prior to each experimental run. Due to the cell giving a magnetic signal which may be of the same (or far greater) magnitude than the sample, it is very easy to produce a series of pressure points which cannot be readily compared, due to care being taken in preparing the cell properly after every increase of pressure.

This was particularly pertinent in this study, as a key aim was to chart the change in the saturated moment – M_{sat} – with pressure, as well as the transition temperature T_c . As T_c usually reveals itself as quite a strong feature in the trace, it can almost always be extracted – even in relatively “low quality” experimental data. To ensure consistency between pressure points, the cell was washed thoroughly in solvent after each pressure change. This is to try and eliminate contamination of the cell from the ram, and other pressure-applying paraphernalia. Also, the position of the locknut on the sample rod was not adjusted whatsoever, and similarly the applied field (0.4 mT) remained unchanged in the susceptometer during the investigation⁷

The raw data from this study is shown in figure 4.10 and the background-subtracted data is shown in figure 4.11. Even in the raw data, the ferromagnetic transition at T_C is very apparent. All plots in figure 4.10 are given on the same scale, such that

⁷It is worth noting that after six different runs with the MAC to measure CeAgSb₂, all yielded a reasonable T_C vs. P relation, only a single data-set was sufficiently “internally consistent” between each trace that the pressure dependence of the saturated moment could be inferred with any conviction.

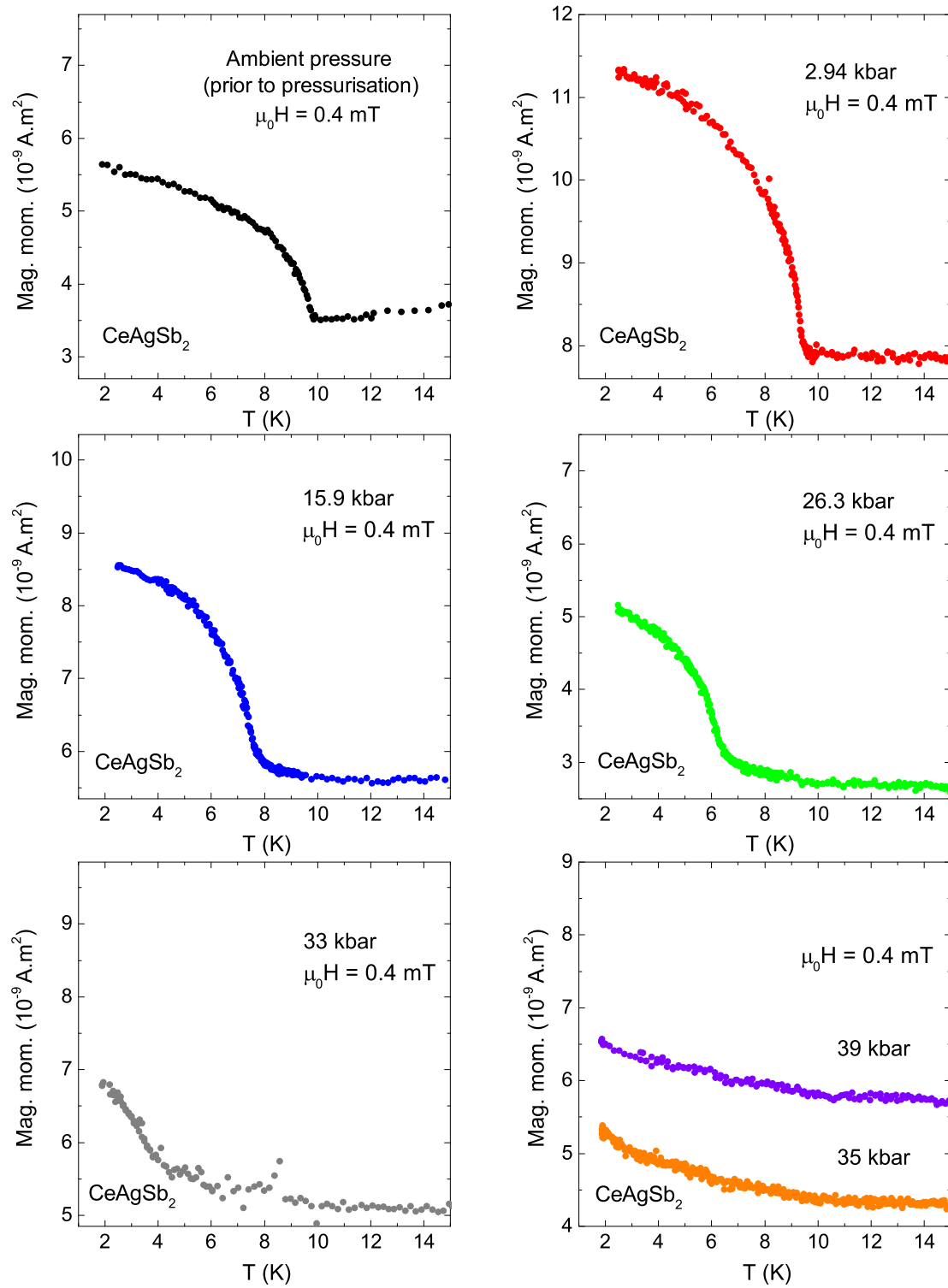


Figure 4.10: Raw MAC data for CeAgSb₂. All traces swept down then up in temperature (bar 0 kbar and 33 kbar, which are downsweeps only). No appreciable hysteresis.

the difference between them in the FM state can be compared directly. Looking at the top left plot, which corresponds to the ambient pressure data before the cell has been properly closed and tightened, it seems strange that the saturated moment then increases after the application of a relatively modest pressure (2.94 kbar), and then reduces successively after the pressure increases further. It is likely that during the initial application of pressure, the position of the sample within the cell changed slightly⁸, and then remained consistent throughout the rest of the study. Alternatively, the condition of the cell may have been slightly different during the ambient pressure run, and then remained consistent throughout the other pressure points. This is evidenced by the similarity between the character of each of the traces at temperatures above T_C , except that at ambient pressure which appears to have a slightly different gradient. As this is a region in which the sample signal is effectively zero, we can use this temperature range to compare the cell backgrounds.

To extract the influence of the cell from the data, traces at pressures beyond the critical pressure were used as a background. Ideally, the cell background is obtained by removing the sample from the cell and then measuring it empty. As already discussed, the susceptometer is highly sensitive to subtle changes in the condition of the cell. For this run, the gasket became contaminated during the removal of the sample and a background run was not possible. The bottom right plot shows two traces at pressures beyond that which fully destroy the FM phase. The choice of these traces as an appropriate background corresponding to the cell is justified by looking at figure 4.9 and also the similarity of the data for $T > T_C$ for all pressures. The characterisation data shows that the signal from the sample above the transition temperature is many orders of magnitude less than that below it. Consequently, the shape of the trace above T_C must (at least in a very major way) correspond to the response of the cell.

The background was estimated by making a quadratic fit was made through the 35 kbar trace, whose 1st and 2nd order contributions of $(1.41 \pm 0.4) \times 10^{-10} \text{A.m}^2.\text{K}^{-1}$ and $(4.9 \pm 2) \times 10^{-12} \text{A.m}^2.\text{K}^{-2}$. The zeroth-order constant is left free for each fit -

⁸For example, that it was at a slight angle and was pushed flat as the gasket came under force.

as the MAC will very rarely gives a consistent initial signal size after the pressure has been increased⁹ - and then adjusted such that all traces overlap for $T > T_C$.

The Curie temperature T_C is extracted from our temperature sweeps at a nominally zero field. Here, we use 4 G to encourage the formation of a single magnetic domain. T_C is defined – as shown in the inset of figure 4.11 – as the point of intersection between two straight lines drawn through $M(T)$ on either sides of the turning point. An Arrott-type analysis [95] would provide a more rigorous determination of T_C , although in the present case is not suitable given the strong influence of the cell in $M(H)$ measurements. Due to the uncertainty in determining the mass and/or dimensions of such a small sample, the plot has been left in the raw units of the measured moment.

The application of pressure reduces the ordering temperature and saturated moment. It is possible to track T_C down to temperatures of around 3 K. A plot of $T_C(P)$ is given in figure 4.12, with pressure points shown from three different anvil cell runs using the same pressure cell and parent sample. Pressure was determined for the second and third cell runs via the ruby fluorescence technique, whereas the superconducting transition of Sn was used for the first. The lack of discrepancy between the two methods highlights their equivalence, although the ruby method is more suited to bulk magnetisation measurements.

The curve shown on figure 4.12 is a power-law fit to $T_C(P) = A|P - P_c|^\alpha$. This yields a critical pressure P_c of 35.8 kbar, along with the exponent $\alpha = 0.35 \pm 0.05$. Both of these numbers agree well with those previously reported in the literature [84, 86]. The pressure dependence of the saturated moment (normalised to the moment at zero pressure) is shown in the right of figure 4.11. The moment remains roughly constant up to around 10 kbar, beyond which it begins to fall, dropping roughly linearly to zero by the critical pressure. The low pressure dependence – from 0 kbar to ~ 7 kbar – of M_{sat} was independently checked with a piston cylinder SQUID cell, which confirmed its approximate constancy in this pressure range.

As a result, the saturated moment is likely to have a highly non-trivial dependence

⁹Whilst there may be an arbitrary offset in the signal size between pressure points, provided care has been taken in increasing the pressure the temperature dependence should remain identical.

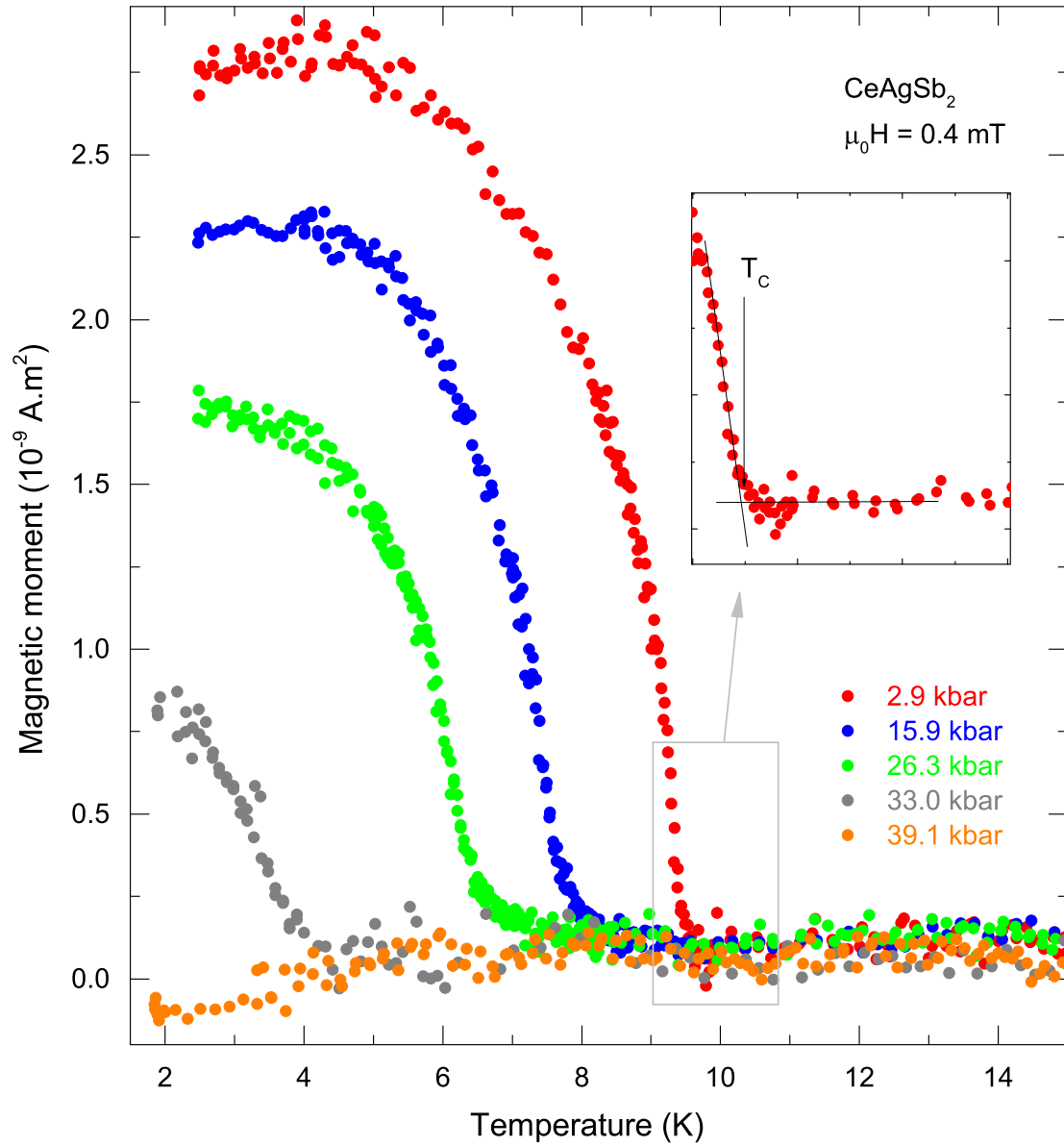


Figure 4.11: Pressure dependence of $M(T)$ in nominally zero (4 G) field. Inset shows how the transition temperature T_C was extracted.

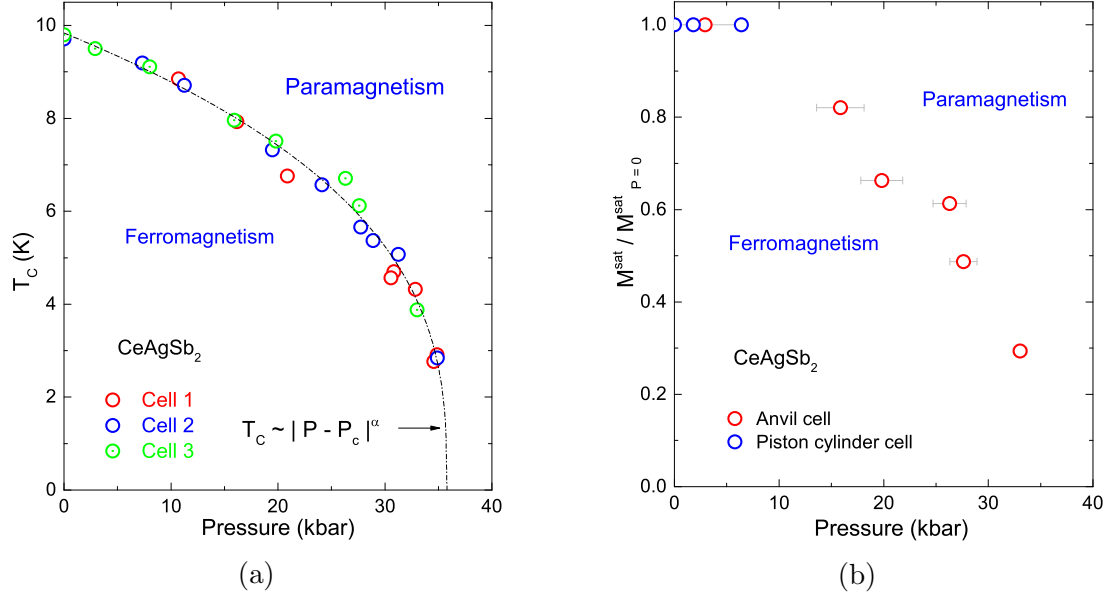


Figure 4.12: Left: PT phase diagram showing the location of the ferromagnetic phase as a function of the applied pressure P . The dot-dash line is a fit to $T_C(P) \propto |P - P_c|^\alpha$ with $P_c = 35.8$ kbar, and $\alpha = 0.35 \pm 0.05$. Right: Pressure dependence of the saturated moment, where the error bars reflect the change in pressure before and after the measurement.

on the applied pressure. The simple Landau theory would predict that the moment should follow a power law dependence - $M_{sat} \sim |1 - P/P_c|^{0.5}$, although this is evidently not the case here¹⁰. The benefit of the piston cylinder cell is that in admitting a much larger sample, the influence of the cell on the data is far less significant. Consequently it is more suited to the saturated moment study than the MAC cell, whose sample space (and as a result sample signal) is many orders

¹⁰Assuming that the free energy as a function of P and M takes on the form

$$F = a(P)M^2 + b(P)M^4 + \dots, \quad (4.2)$$

then, at equilibrium where $dF/dM = 0$ and a finite magnetisation M_{sat} we have that

$$M^2 = -\frac{a}{2b} \quad (4.3)$$

and assuming $a(P) = a_0(P - P_c)$, it follows that

$$M_{sat} \sim |P - P_c|^{\frac{1}{2}}. \quad (4.4)$$

of magnitude smaller. To investigate the apparently unusual dependence of M_{sat} on P in this region it would be desirable to use a piston cylinder cell which is able to withstand pressures of up to 15 kbar.

The high pressure ($P > 35$ kbar) data did not show any signatures consistent with the existence of antiferromagnetism. Following the removal of the FM state, the traces became flat and remained so up to the highest measured pressures (≈ 55 kbar). This is not, however, particularly revealing. Unlike a superconducting or ferromagnetic transition, the system does not undergo an abrupt increase (or decrease) of its M at the Néel temperature T_N . This means that a DC measurement such as this (which couples to the magnitude of M) may not have the sensitivity to resolve T_N , whereas a differential measurement coupling to dM/dH – such as AC-susceptibility – might. For a DC measurement, an AF transition may be made sharper in the data by applying a suitably strong field; this is not beneficial here due to the increasing background of the cell in higher fields. Similarly, no diamagnetism indicative of superconductivity was found around 35 kbar, nor at higher pressures.

4.4 Field Tuning

Previous studies in the literature have shown that the ferromagnetic state is sensitive to the application of a transverse applied field, which we will examine here through the electrical resistivity, and both AC- and DC-susceptibility measurements. Whilst the low temperature critical region of the PT phase diagram has been investigated in the literature somewhat already, the same measurements do not exist for the analogous field-induced zero-temperature transition..

4.4.1 Transverse magnetisation

To track the field dependence of the ordered phase we would, ideally, simultaneously measure along the easy ($M_{\vec{c}}$) axis, whilst tuning with a transverse field applied in the \vec{ab} -plane. Unfortunately, owing to the arrangement of the pick-up and external field-applying coils within the Cryogenic Ltd SQUID this is not possible. Instead, we are forced to track $T_C(H)$ indirectly, by identifying the corresponding signature in the \vec{ab} magnetisation and seeing its response to the field. As shown in the characterisation measurements previously, the in-plane DC response shows a sharp peaked feature at T_C , and so it is this feature which will be followed.

For this study, a sample with mass 6 mg – fixed with superglue to a graphite stick – was measured in the susceptometer. The flat surfaces of the platelet-like samples are normal to the easy-axis, making it relatively straightforward to orient them with precision. The quality of the orientation can be checked further by monitoring the sharpness of the features appearing in $M_{\vec{ab}}$, as components of the tuning field which are directed along the c -axis break the symmetry of the magnetic state above T_C , resulting in a *softening* of the feature in $M_{\vec{ab}}$.

Figure 4.13 shows $M_{\vec{ab}}(T)$ at a number of fields. No hysteresis was found on any trace at any field or temperature. Unfortunately, we cannot take this as an indication that the transition has remained second-order, as we are not probing the FM moment directly. The feature which we identify as corresponding to the ferromagnetic transition becomes suppressed to lower temperatures as the applied

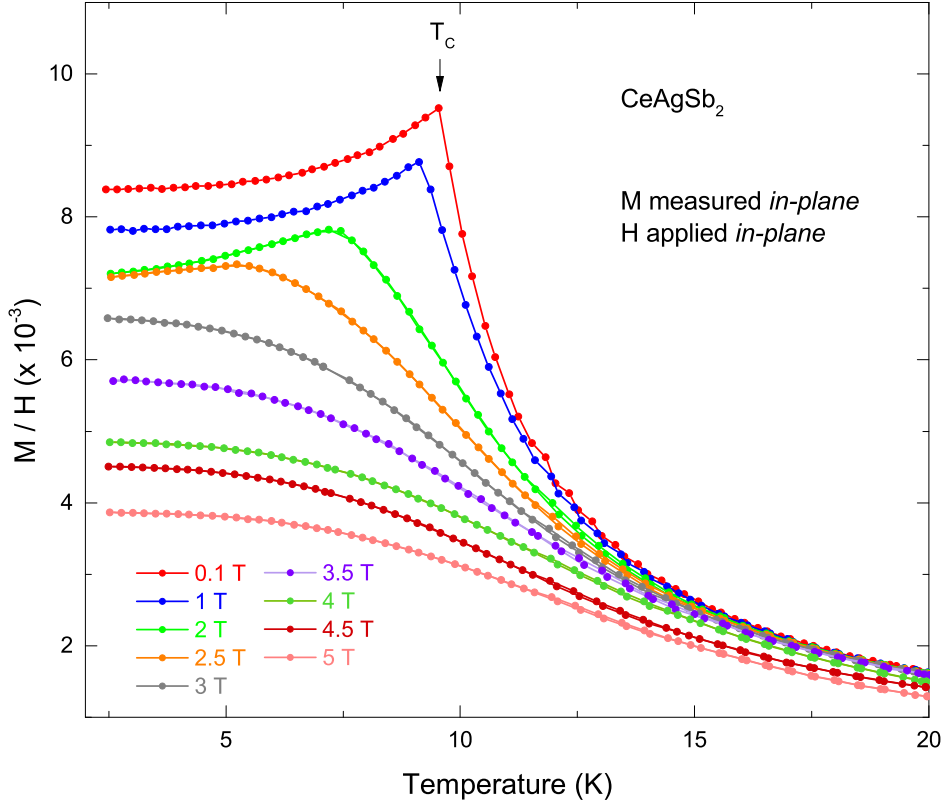


Figure 4.13: Temperature dependence of the in-plane magnetisation at various transverse fields. M and H in SI units such that M/H is dimensionless.

transverse field is increased, although it becomes difficult to resolve the anomaly in $M_{ab}(T)$ at fields above 2.5 T. Consideration of the phase diagrams given in the literature [76–78] suggests that this may be due to T_C dropping away rapidly towards 0 K as the critical field approaches.

At this point, it becomes useful to approach the phase boundary in an orthogonal direction by holding the temperature constant and sweeping the field. Some of these sweeps may be seen in figure 4.14. The disappearance of the \vec{c} -axis component of the magnetisation is identified as the change in slope of $M(H)$. As shown in figure 4.14, H_c is extracted by drawing two straight lines on either side of the corner and finding the intersection. As in the temperature sweeps, the isotherms exhibit no hysteresis, and the character of $M(H)$ remains consistent down to 280 mK. This suggests that the nature of the transition remains constant from zero

up to the critical field.

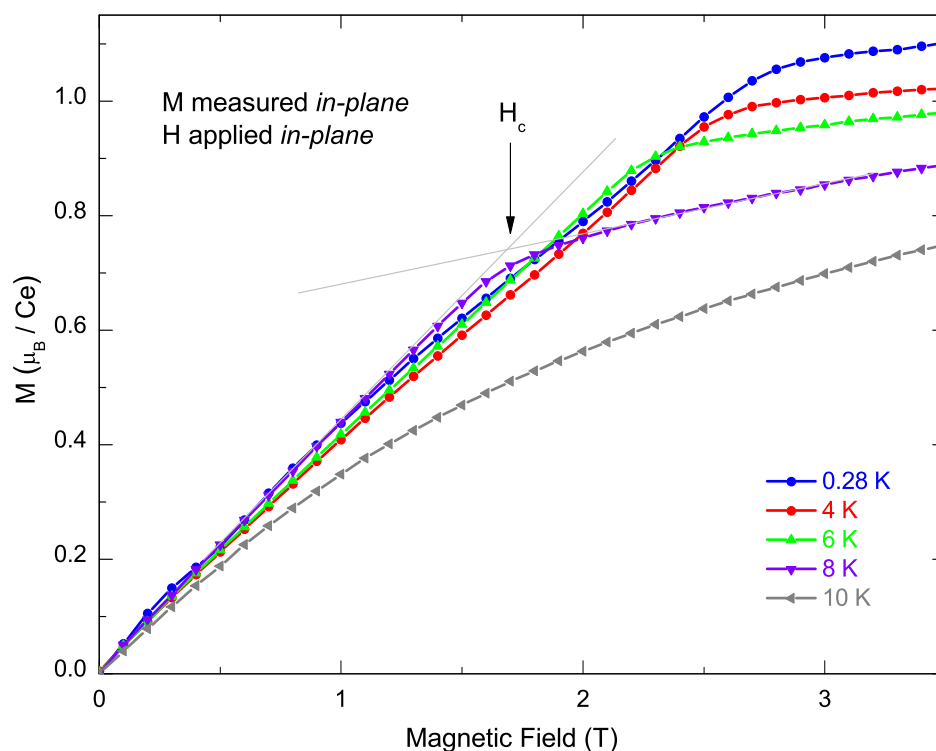


Figure 4.14: Isothermal field sweeps for CeAgSb₂, measured in-plane.

The critical fields and temperatures for both of these studies are included on the phase diagram shown later on in this chapter.

A very useful Maxwell relation exists which relates the magnetisation M to the entropy S :

$$\left(\frac{\partial M}{\partial T}\right)_H = -\left(\frac{\partial S}{\partial H}\right)_T. \quad (4.5)$$

This offers a pathway toward other thermodynamic measurements, which can be used to corroborate the results of our DC-susceptibility study.

Specific heat measurements of CeAgSb₂ in a transverse field – made by Yang Zou, a PhD student in the Quantum Matter group – are shown in figure 4.15. In zero-field, C/T increases as T_C is approached from above and shows a sharp peak at the transition. This is what we would expect for a continuous phase transition in the

presence of critical fluctuations. With increased field, the anomaly broadens and shifts to lower temperatures. Interestingly, up to a field H^* there exists a crossing point at a temperature T^* , through which all curves intersect almost exactly i.e. $C(T^*, H') = C(T^*, H'')$ for all $H', H'' < H^*$, as shown in the inset. As can be seen, the curve corresponding to 7 T does not intersect at this point, and the rest of the data (not shown) suggests that $H^* \approx H_c$.

Provided that $C(H)|_{T=T^*}$ does not contain any peculiar wiggles up to $H = H^*$, the existence of the crossing point means that we can infer:

$$\left(\frac{\partial C}{\partial H} \right) \Big|_{T=T^*, H < H^*} = 0. \quad (4.6)$$

Then, equipped with the Maxwell relation (eqn. 4.5) we can examine the consequences of this condition on the magnetisation M . Substituting into equation 4.6 for the heat capacity C in terms of the entropy S , we find

$$\frac{\partial}{\partial H} \left\{ C = T \left(\frac{\partial S}{\partial T} \right) \right\} \Big|_{T=T^*, H < H^*} = \frac{\partial}{\partial T} \left(\frac{\partial S}{\partial H} \right) \Big|_{T=T^*, H < H^*} = 0 \quad (4.7)$$

$$\Rightarrow \left(\frac{\partial^2 M}{\partial T^2} \right) \Big|_{T=T^*, H < H^*} = 0. \quad (4.8)$$

Thus, the crossing point in the specific heat ought to correspond to a point of inflection in the magnetisation. The right-hand side of figure 4.15 shows the second derivative of the magnetisation with an inset showing the point at which $M'' = 0$, corresponding to the crossover in the specific heat. Also in the specific heat, as the field moves beyond the critical field the point at which $M'' = 0$ begins to shift, in this case moving to higher temperatures.

These appearance of such crossovers has been discussed in the literature by Vollhardt [96, 97] who highlighted and analysed their presence in a number of systems; the term *isosbestic point* was borrowed from spectroscopy as a moniker for the crossover due to the similarity with an optical effect found in chemical systems. The intersection of specific heat curves under the influence of a thermodynamic variable X – here, the applied field H – was shown to be related to a sum rule involving the entropy at high T . Moreover, the presence and width of the crossing

window is determined by the properties of the higher-order-moments of the generalised susceptibility associated with the variable X – in our case, $\partial^n M / \partial H^n$. Similar crossing points have also been found in heavy fermion compounds CeCu_{5.5}Au_{0.5} in a transverse field [98] and CeAl₃ under pressure [99], along with the skyrmion-lattice system MnSi [100] in an applied field.

A more complete analysis of the $M(T, H)$ and $S(T, H)$ data, not simply the crossing points, using equation 4.5 is currently in progress.

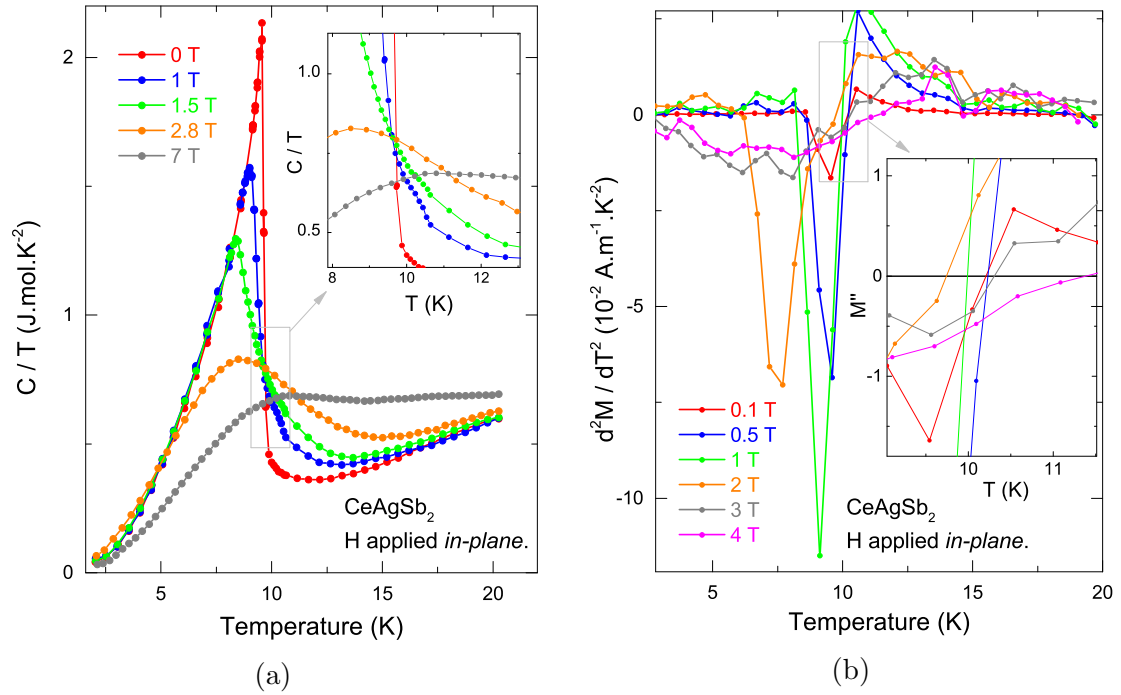


Figure 4.15: (a) Specific heat of CeAgSb₂ in a transverse field. The inset shows the crossing point at different fields as described in the text. (b) Second-derivative of the magnetisation M'' at various transverse fields, with an inset showing the corresponding feature to the crossover.

4.4.2 Resistivity

The in-plane resistivity was also measured in a transverse field using the DMS to allow measurement down to 100 mK. The single-crystal sample was cut into shape with a wire-saw before being polished to a suitable thickness, final dimensions $\approx 2 \times 1 \times 0.2$ mm. An AC excitation current of 1 mA and $f=23$ Hz was applied in-plane, with the external field applied across the sample.

Example traces are shown in Fig. 4.16. An anomaly corresponding to T_C can be seen in the zero-field data, although is rapidly washed as the field is increased, consistent with reports elsewhere [77]. Figure 4.16 includes a $\rho(T) = \rho_0 + AT^2$ fit to the zero-field data, which is fitted up to 500 mK (as shown later in figure 4.18). Quite evidently, this is not a good description of the data; there is a clear higher-than-quadratic contribution.

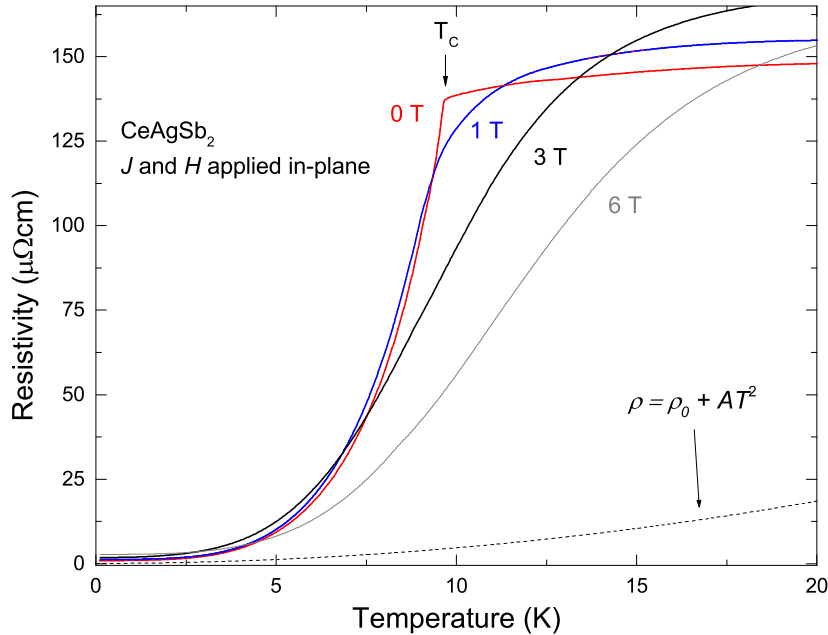


Figure 4.16: $\rho(T)$ data at various transverse fields. The dotted line is a low- T fit of $\rho(T) = \rho_0 + AT^2$ to the zero-field trace – as shown in the top left of figure 4.18 – to show the superquadratic dependence of the resistivity.

Looking at the low temperature data, as in the top left of figure 4.18, the resistivity only returns to the T^2 dependence expected of a simple Fermi-liquid at the lowest

temperatures. This was previously attributed to scattering from thermally activated spin-waves [77, 79, 84] which become frozen out at the lowest temperatures. In particular, the existence of a gap Δ in the magnon dispersion results in an exponential dependence of $\rho(T)$, rather than a simple power law¹¹. The resistivity then has the form $\rho = \rho_{FL} + \rho_m$, where in addition to the usual quadratic T term ρ_{FL} , the contribution from magnon scattering ρ_m is given by [94]:

$$\rho_{FM} = BT\Delta \left(1 + \frac{2T}{\Delta}\right) e^{-\Delta/T} \quad (4.9)$$

$$\rho_{AFM} = C\Delta^5 \left\{ \frac{1}{5} \left(\frac{T}{\Delta}\right)^5 + \left(\frac{T}{\Delta}\right)^4 + \frac{5}{3} \left(\frac{T}{\Delta}\right)^3 \right\} e^{-\Delta/T}, \quad (4.10)$$

corresponding to scattering from FM or AFM magnons.

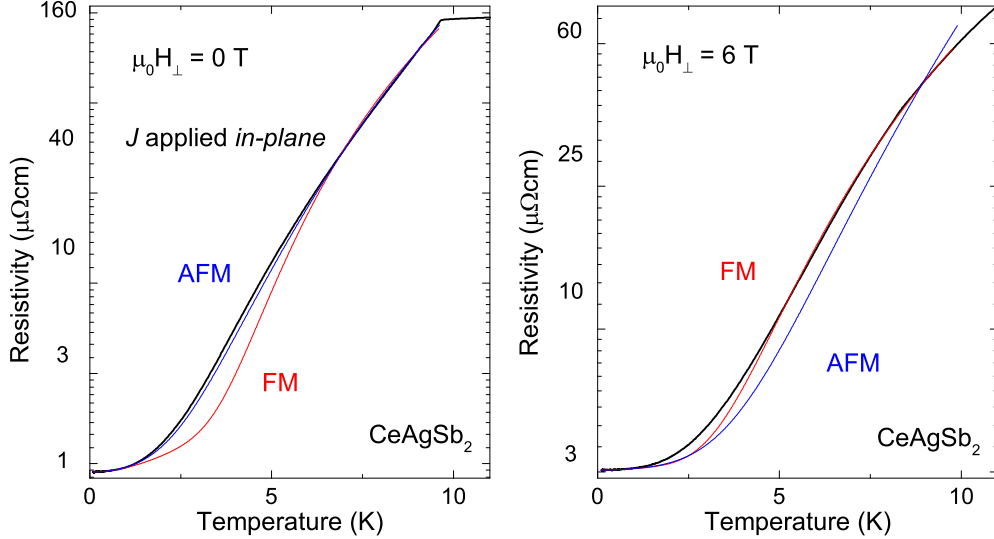


Figure 4.17: Semilog plot of $\rho(T)$ for zero and 6 T transverse fields, with a comparison of the fits to eqn. 4.9 (red) and 4.10 (blue), together with the Fermi liquid contribution - $\rho(T) = \rho_0 + T^2$ - determined as in the top left of figure 4.18.

In figure 4.17 the results of the zero-field and 6 T fit to equations 4.9 and 4.10 are shown¹² Equation 4.9 provides the better fit in zero-field, although upon applica-

¹¹Scattering from AFM / FM ferromagnetic spin-waves results in a $T^2/T^{1.5}$ dependence of $\rho(T)$ [94].

¹²This is done by first fitting the low-temperature data - 100 mK to 500 mK - to $\rho = \rho_0 + AT^2$, and then fixing ρ_0 and A , before fitting the one of the full expression above up to ≈ 9 K.

tion of a transverse field, the FM fit becomes superior. The field dependence of the coefficients from the FM fit are shown in figure 4.18, along with the goodness-of-fit parameters R^2 .

The dotted lines on the figures show the location of the zero-temperature critical field, as determined from the magnetic measurements, and each of the parameters shows some sort of a change at H_c . For example, the A -coefficient - obtained via a low temperature (100mK - 500mK) fit to $\rho(T) = \rho_0 + AT^2$ - appears to become enhanced in the critical field region ~ 2.8 T. A naive interpretation of the system at H_c as a gapless FM state would result in a quadratic T dependence of the electron-magnon scattering. Therefore it is unclear whether the increase in A reflects changes in the electron-electron, or electron-magnon scattering. The gap obtained by the FM fit is suppressed by the transverse field, although remains finite above H_c ¹³. In the high-field *paramagnetic* (PM) region the resistivity retains a higher-than-quadratic temperature dependence for intermediate $T > 1$ K.

¹³It is difficult for us to say exactly what happens at H_c with this data-set for lack of field points. At the time the data was collected, the critical field was taken as that which was quoted in the literature - around 3 T - whereas our own subsequent measurements revealed it to be slightly lower.

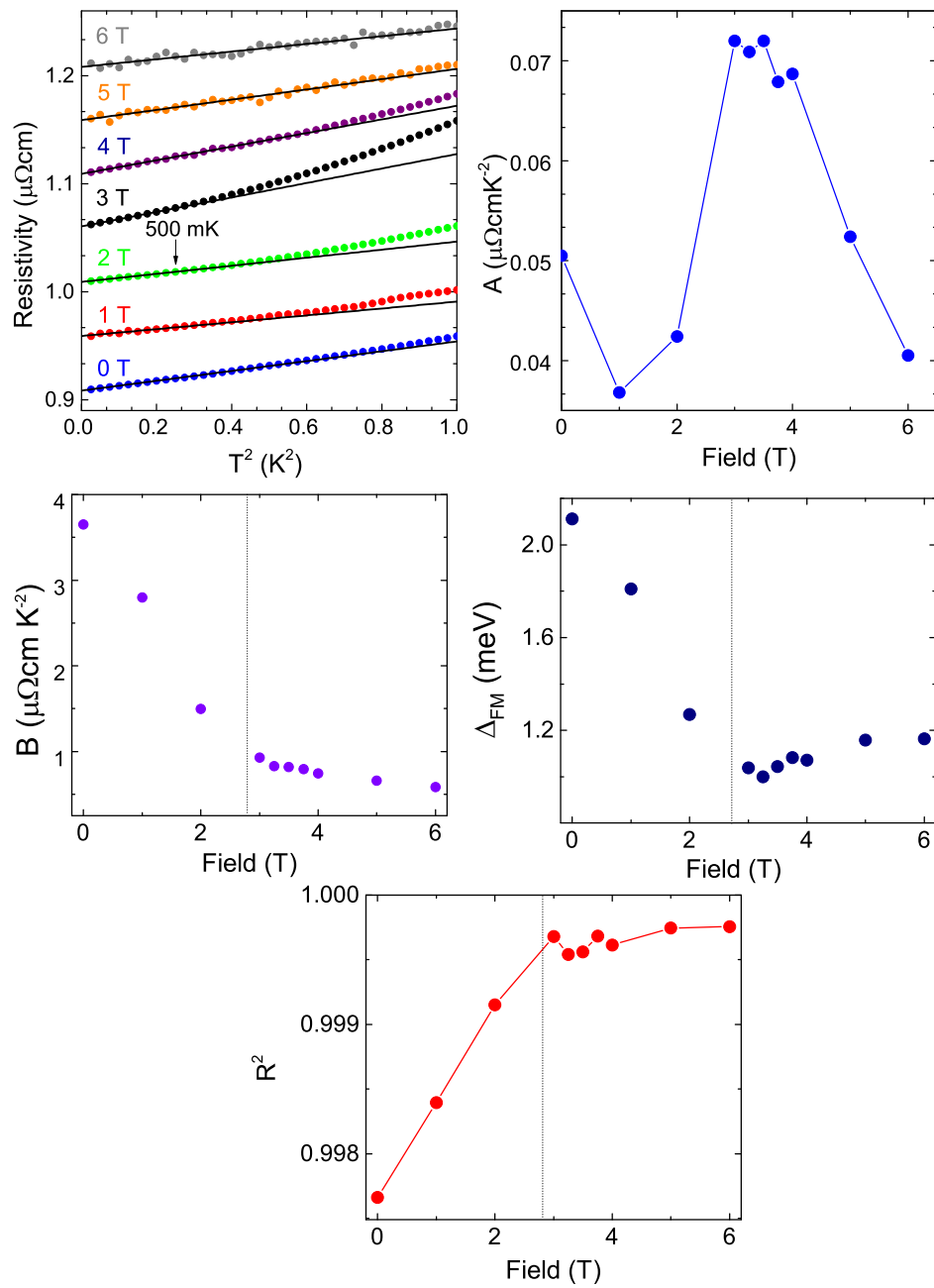


Figure 4.18: Field dependence of the fitting parameters obtained by fitting the data to equation 4.9. Bottom figure shows the field dependence of the goodness-of-fit coefficient.

4.4.3 Transverse AC susceptibility

An AC-susceptibility experiment was designed in such a way to allow simultaneous detection along the *easy* axis and transverse field tuning along the *hard* axis. A schematic of the set-up which went into the DMS is given in figure 4.20. The susceptometer itself was made by Dr F. Malte Grosche, and comprises of three mutually wound coils – two pick-up coils and one modulation coil - held in place with two nylon bolts, which are then screwed into an aluminium bracket. The sample is affixed to one of the ends of the bolts by a residue of GE varnish. Thermalisation to the sample stage takes place via a $500\mu\text{m}$ silver wire, attached to the sample with silver epoxy. The wire is fed out of the bracket via a groove cut into one of the bolts, and then screwed firmly beneath a washer mounted on the copper sample platform. The device was assembled by Hong'En Tan, another PhD student in the Quantum Matter group.

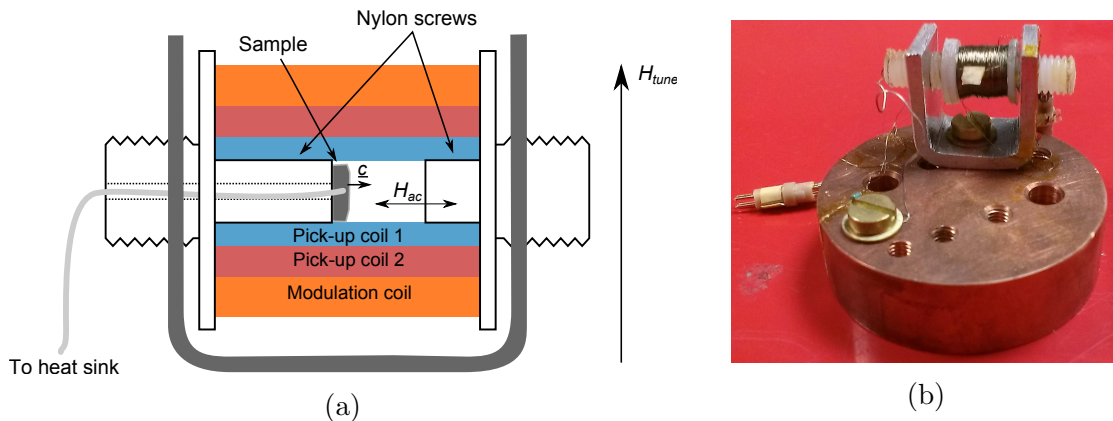


Figure 4.19: (a) Schematic of the coilset and its components. (b) Coilset on copper sample platform after measurement.

The sample itself was the same sample as was used for the transverse DC-magnetisation study shown in section 4.4.1, with mass 6 mg and dimensions on the order of $1 \times 1.5 \times 0.5 \text{ mm}^3$.

A lock-in amplifier in conjunction with a balanced current source [101] provides the AC signal at 29 Hz for the drive-coil. The frequency is chosen to optimise the performance of the transformers, and to avoid multiple or rational fractions

of 50 Hz. Initially, an excitation current of 1 mA was used, although this was varied later on in the experiment to investigate the dependence of our signal on the amplitude of the driving field. An estimate of the field likely to be generated by our coil using Ampère's law predicts that an excitation current of 1 mA will generate a driving field with amplitude 1 Oe.

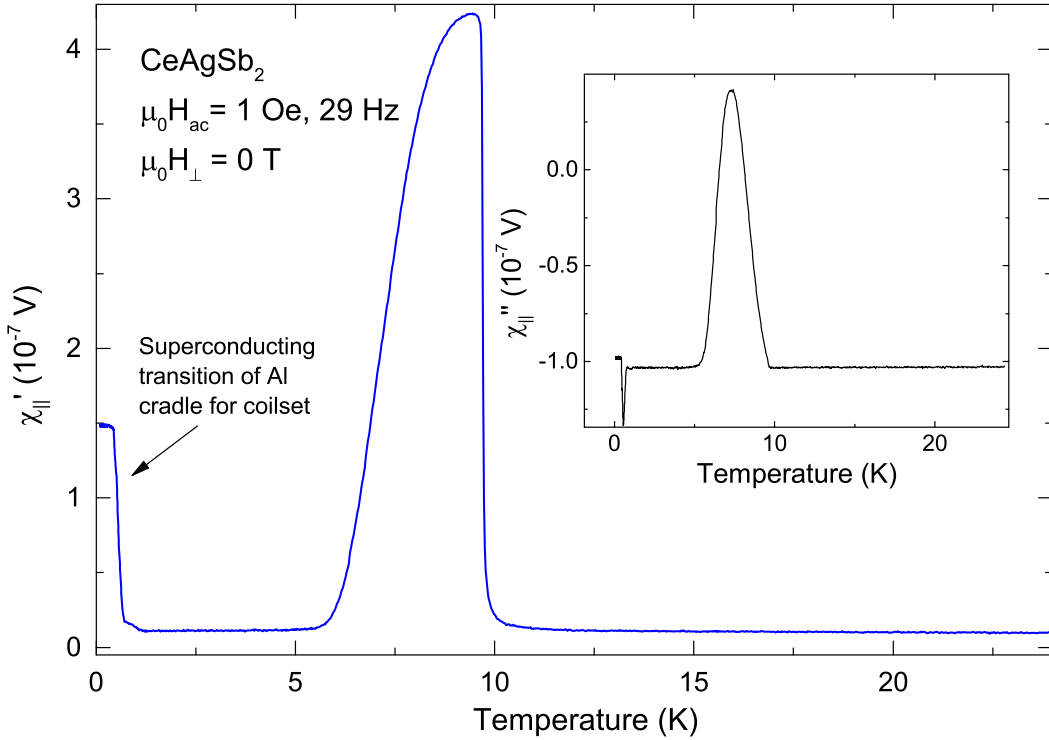


Figure 4.20: AC-susceptibility measured along the easy axis for CeAgSb₂ in zero field. The peak at ~ 10 K corresponds to the magnetic transition, whilst the feature at low temperature is due to the superconducting transition of the aluminium cradle holding the coil. Inset: The imaginary part χ''_{\parallel} .

Figure 4.20 shows the real part of the easy-axis susceptibility χ'_{\parallel} , in zero applied transverse field. A clear feature can be seen at $T_C = 9.6$ K, which corresponds to the magnetic transition. Also visible at lower temperatures is a feature due to the aluminium bracket becoming superconducting¹⁴. The inset shows the imaginary part of the susceptibility χ''_{\parallel} , which also shows a strong feature growing out of T_C .

¹⁴This had been considered when designing the assembly, but given the relatively low critical field of aluminium (10 mT) [102], was not considered important.

The response of the imaginary part corresponds to dissipative processes which take place within the sample.

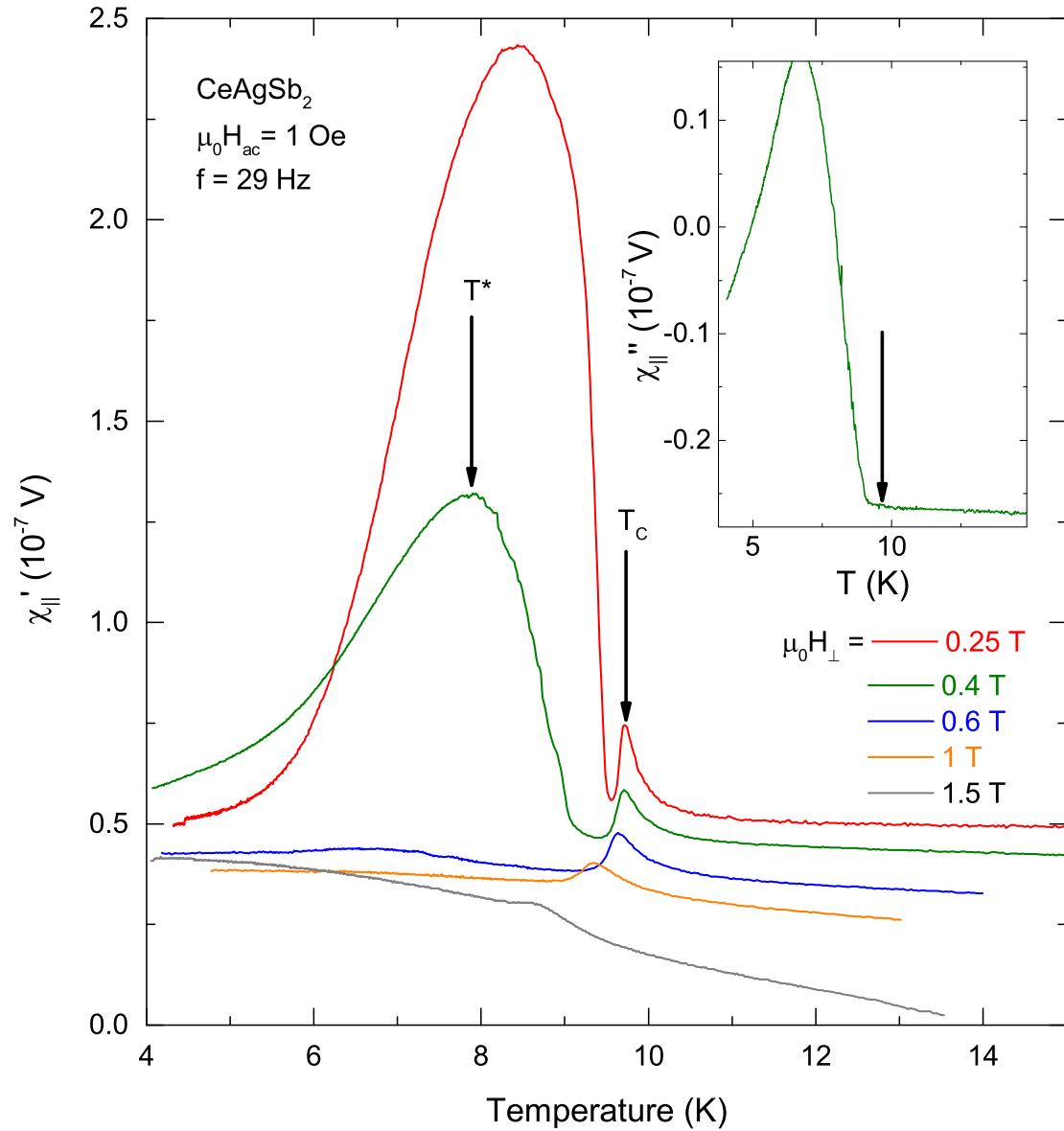


Figure 4.21: AC-susceptibility of CeAgSb₂ in zero field, inset shows the imaginary part $\chi''_{||}$.

Figure 4.21 shows the evolution of $\chi'_{||}$ under the influence of a finite transverse field. As the field is increased, the main peak appearing at T_C is rapidly suppressed in both magnitude and temperature. Strikingly, as this feature shifts to lower

temperatures, a second peak is revealed beneath the main one, pinned near 9.6 K, much smaller in magnitude. By transverse fields of around 0.25 T the peaks have separated totally, resulting in two very distinct features appearing in χ'_{\parallel} - the higher temperature kink appearing at around 9.5 K still, and a stronger, broader maximum which appears at a lower temperature T^* . As the field is increased further, the more pronounced hump at T^* broadens, and disappears by 0.5 T, whereas the higher temperature kink seems to track the phase boundary found from our magnetisation data. It was not possible to resolve this feature at fields beyond 1.75 T.

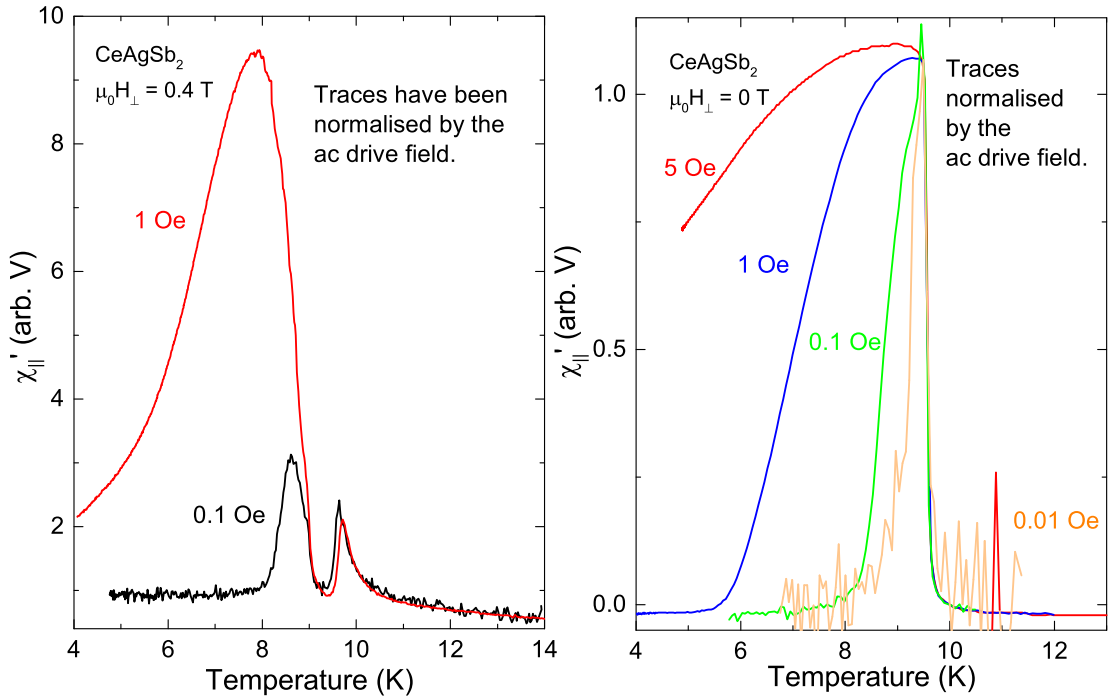


Figure 4.22: Comparison of the real part of the susceptibility χ^{\parallel} in different ac excitation fields.

The field dependence of both of these features is plot on the HT phase diagram given in fig. 4.23. Immediate inspection would suggest that the higher temperature kink ought to correspond to the ferromagnetic transition, as it does seem to trace the boundary described by other measurements, although this then begs the question of what the other feature should correspond to, as there is no report in the literature of a second transition. The imaginary part of the susceptibility χ''_{\parallel} is

far more sensitive to the feature at T^* than the one at T_C . This is shown in the inset of figure 4.21, where the arrow gives the location of T_C taken from $\chi'_{||}$. The trace appears to be flat as we move through T_C , not showing any response at all, but seems to grow significantly at the onset of the anomalous transition at T^* ¹⁵.

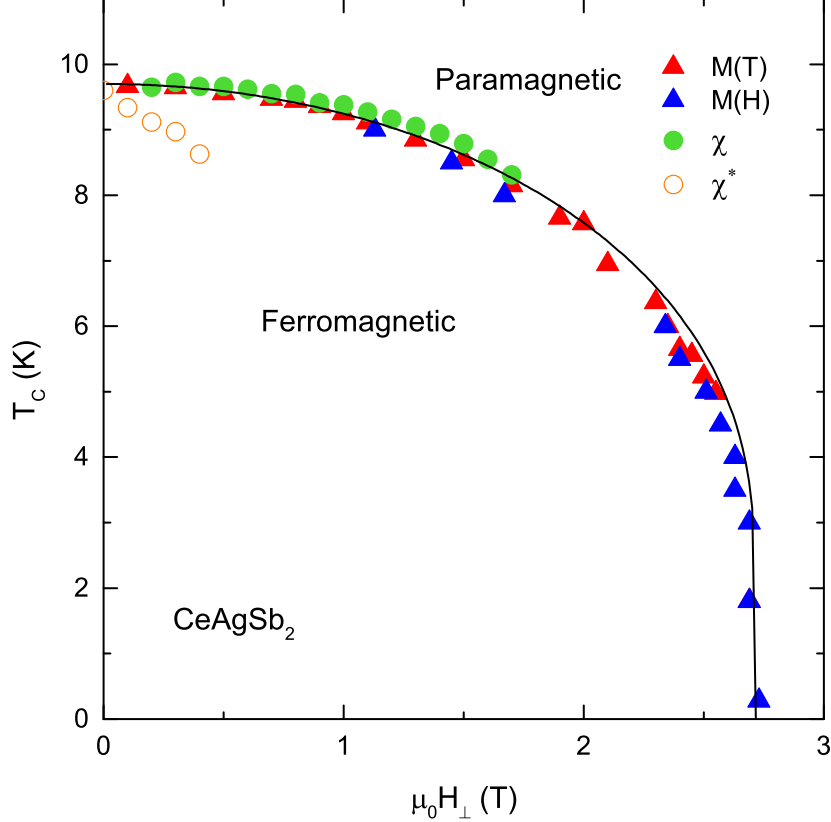


Figure 4.23: HT phase diagram for CeAgSb₂ showing the phase boundary extracted from $M(T)$, $M(H)$ and the small upper anomaly $\chi'_{||}$, separating the ferromagnetic and paramagnetic ground states. The solid line is a fit to $\tanh(h/t) = h$, with h and t the reduced field and temperature, corresponding to a $J = 1/2$ mean-field Ising model [103].

Unlike the kink at T_C , the anomalous hump shows a strong dependence on the magnitude of the driving field. The left hand plot of figure 4.22 shows $\chi'_{||}$ for AC-fields of 1 Oe and 0.1 Oe, in a transverse field of 0.4 T, with the traces normalised by the AC-field and overlaid. Clearly, whilst the anomalous feature is significantly

¹⁵It may be that the transition at T^* is related to a skin-depth effect. A proper study of the frequency dependence of the broad peak would be required to investigate this further.

broadened and enhanced in 1 Oe compared to 0.1 Oe, the other feature at T_C remains unchanged. This is consistent at amplitude of driving field we choose – increasing the amplitude of the AC signal enhances the signal-to-noise ratio of our data, but does not affect the width or location of the feature. The right hand plot shows the data in four different excitation currents in zero transverse field – the peak becomes increasingly narrowed as the driving amplitude is reduced.

4.5 Discussion

Our study of the pressure dependence of the magnetism in CeAgSb₂ found that 35 kbar is sufficient to destroy the low-pressure magnetic order. According to Doniach's interpretation of the Kondo lattice [104], the magnitude of the itinerant/local-state exchange coupling \mathcal{J} determines the outcome of the competition between the RKKY and Kondo energy scales, dictating whether or not the ground state is magnetic. In applying pressure to a system, there is an increase in the overlap between neighbouring states, which increases the magnitude of \mathcal{J} . For sufficiently large \mathcal{J} , the Kondo effect will always dominate and drive the system non-magnetic.

We cannot be certain that CeAgSb₂ is not driven antiferromagnetic in the region where T_C seems to drop to zero, as it is likely that our high pressure magnetisation measurements are not sensitive enough to resolve the signature of an AFM transition. This could be probed more carefully via a microcoil measurement in an anvil cell, which may be able to better detect the AFM [56], as the induced voltage couples to the magnitude of dM/dH rather than M .

In a transverse field, FM is destroyed by in-plane fields exceeding 2.8 T. In the ferromagnetic regime the resistivity follows a higher than quadratic temperature dependence at elevated $T > 1$ K, which is consistent with scattering from gapped magnetic excitations. Near the critical field, the Fermi-liquid A coefficient from the electrical resistivity is enhanced. This is often taken as a hallmark of increased scattering due to the presence of critical fluctuations [105]. Here, the increase is relatively modest with an enhancement of around a factor two, rather than the order of magnitude increase often found near strong quantum fluctuations. It is likely that the increase in A is related to the reduction in the anisotropy gap Δ , which can be seen in figure 4.18. As Δ is lessened, excited magnons persist to lower and lower temperatures, meaning that ρ remains superquadratic to lower and lower temperatures.

For $H > H_c$ we do not recover a Fermi-liquid T^2 dependence over an extended T -range as we may expect, but maintain a superquadratic dependence for $T > 1$

K with increased field. In fact, the quality of the fit to the FM spin wave given in equation 4.9 seems to be better above H_c than below it. The existence of an exponential T -dependence of ρ above H_c means that the anisotropic exchange interactions detailed in [76] are still present above H_c . The T^2 behaviour survives to higher and higher temperatures as the field is increased, reflected in the field-induced dampening of the electron-magnon coupling coefficient given in figure 4.18.

Measurements of $\chi_{||}$ revealed the existence of two field dependent features. One was strongly dependent on the driving field and disappeared rapidly with an increased transverse field, whereas the other appeared to trace the phase boundary given by other probes. If H_c marked the location of a FMQCP we would expect to find an enhancement of $\chi_{||}$ in the vicinity of H_c , due to the strong magnetic fluctuations. This can be seen in the YbNi₄P₂ data from the beginning of the chapter (figure 4.2) where χ grows by many orders of magnitude. In CeAgSb₂, rather than $\chi'_{||}$ becoming enhanced as $H \rightarrow H_c$, we cannot even resolve the signature of the transition at the critical field. The origin of the anomalous hump remains a mystery.

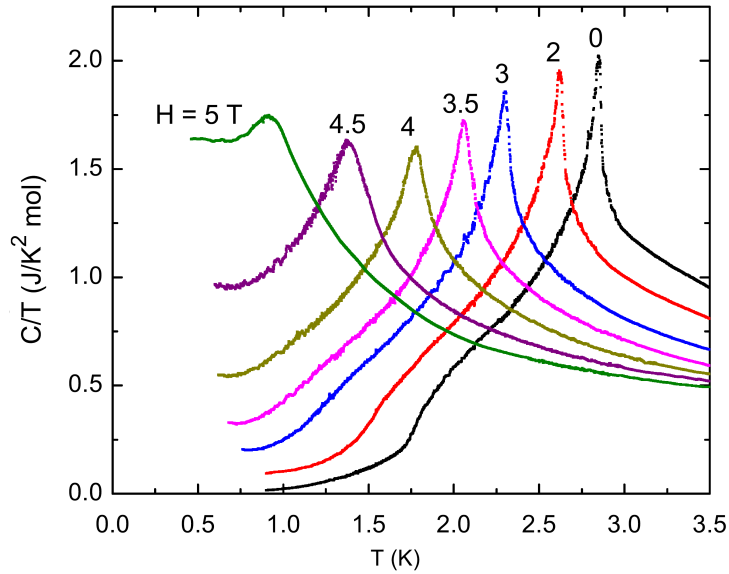


Figure 4.24: Specific-heat data for the Ising-like ferromagnet CoNb₂O₆ in a transverse field, from [106].

CeAgSb₂ has not shown behaviour strongly consistent with the presence of critical fluctuations at H_c . Perhaps, this could be due to sample misalignment? Maybe

we are not probing the true “critical region” around H_c , and some finite field-component along the easy-axis is pushing us away from the sheet of supposedly second-order transitions found along the line $H_z = 0$. This, however, seems unlikely. Firstly, the agreement of the phase boundary between different probes shown on figure 4.23 would be hard to explain if one of the measurements had a badly aligned sample, as any field parallel to the easy-axis *promotes* T_C to higher temperatures [77]. Secondly, even if the sample was slightly misaligned, we would expect to feel the extended influence of the FMQCP from our position in the phase diagram, even though we are not sitting on top of it exactly.

It is likely that the absence of critical behaviour is intrinsic to this system, and in applying a transverse field we are not inducing increasingly strong quantum tunnelling between up and down FM states, but perhaps simply gradually rotating the spins toward the direction of the applied field. Looking back at the specific heat data shown in figure 4.15, the evolution of C/T in the transverse field is certainly very different to that seen in other field-tuned quantum critical systems – see figure 4.24. The character of the anomaly is not consistent as it suppressed to lower- T with field, but rather it becomes “smeared out” as H is increased; the character of the FM transition is changed when the transverse field is applied. If the transition turned first order on the approach to H_c we would find a “sharpening” of the feature in the specific heat - see the schematics given in chapter 2 of the Ehrenfest scheme. Presumably in CeAgSb₂, in the presence of a finite transverse field, the “ferromagnetic” transition no longer corresponds to a true second-order phase boundary, but some sort of *crossover* into the spin-polarised state instead. It is for this reason that we do not find superconductivity in the region that T_C goes to zero.

Chapter 5

YFe₂Ge₂

YFe₂Ge₂ is a paramagnetic metal with anomalous low temperature behaviour: a $T^{3/2}$ dependence of the electrical resistivity $\rho(T)$ is seen up to 10 K, as well as a heat capacity with an unusually high Sommerfeld coefficient ($\gamma \sim 100$ mJ/K²), which shows an upturn as $T \rightarrow 0$ K. It is closely related to LuFe₂Ge₂ which orders antiferromagnetically at $T_N = 9$ K. In the Lu system, the ordering temperature T_N may be *promoted* via hydrostatic pressure - or *suppressed* by doping. In the doping series Y_xLu_{1-x}Fe₂Ge₂ a critical doping level x_c is sufficient to drive the ordering temperature to 0 K [107].

Our measurements have found that at around $T_c = 1.5$ K, the electrical resistivity of YFe₂Ge₂ drops to zero, consistent with a hitherto unseen superconducting phase. This chapter describes a series of low-temperature magnetic measurements which were made on YFe₂Ge₂.

The results shown here constitute the first evidence of a diamagnetic response in this system below T_c .

5.1 Fe-based superconductivity

Following the discovery of superconductivity at $T_c = 26$ K in a layered system containing iron [108] there has been an explosion of study in other Fe-based inter-

metallics. The interest in these systems stems from their apparent analogy with the ceramic cuprate high-temperature superconductors (HTSC) [8], along with the integral role iron appears to play in governing the low-temperature electronic state. In classical phonon-mediated superconductors, magnetic impurities are anathema to the superfluid state as they break the time-reversal symmetry of the Cooper pair, which rapidly kills off T_c . This makes the appearance of *iron-based* families of superconductors all the more surprising.

The iron-based systems found so far can be split into groups based on their structures and composition¹ [9]:

- “11” - FeSe
- “111” - LiFeAs, NaFeAs,
- “122” - BaFe₂As₂, CaFe₂As₂, SrFe₂As₂ ...
- “1111” - LaFeAsO, LaFePO, CeFeAsO ...

Despite appearing very different, there are many commonalities shared between them, such as quasi two-dimensional electronic structures and the presence of magnetism/strong magnetic fluctuations associated with the moment on the Fe site [9].

¹This list is of the parent systems, whereas in reality hole- or electron-doping may be necessary to induce superconductivity.

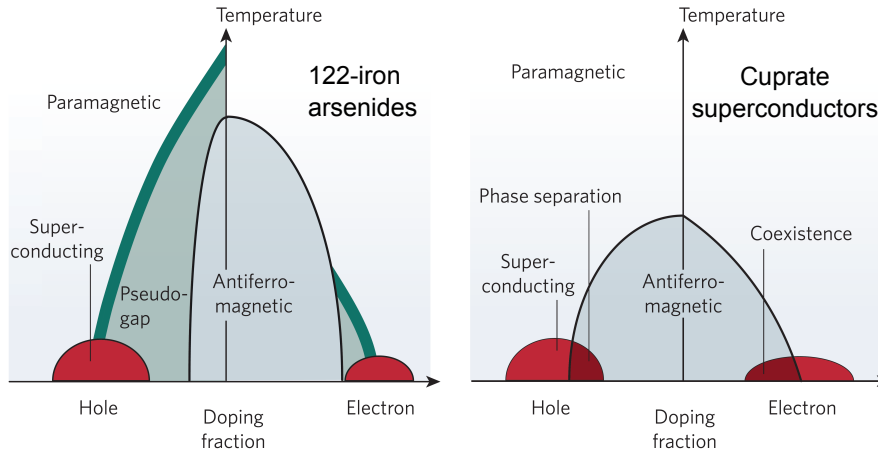


Figure 5.1: Generic phase diagram for the 122-iron arsenides and the high-temperature cuprate superconductors, [109].

In the 122 systems, a high-temperature semi-metallic spin density-wave (SDW) phase is suppressed with doping, either with holes or electrons, and at a critical doping x_c , a low-temperature superconducting state forms. The transition temperature T_c may then be boosted by further doping, and at the point it reaches a maximum the system is said to be “optimally doped”. A schematic of the generic phase diagram is given in figure 5.1 along with that of the ceramic HTSCs for comparison.

As in the $4f$ AF heavy fermion superconductors from the previous chapter, it is thought that the appearance of a bubble of superconductivity in the phase diagram at low temperatures is related to the strong AF fluctuations associated with the zero-temperature magnetic phase transition [110]. To identify and investigate other systems which may belong to this class, it would then be reasonable to focus attention on those which order antiferromagnetically, in particular those whose order may be suppressed with an external tuning parameter.

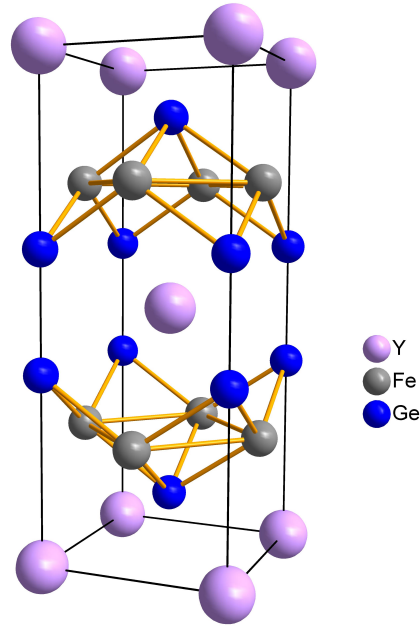


Figure 5.2: ThCr₂Si₂ (I4/mmm) type structure shared by LuFe₂Ge₂ and YFe₂Ge₂.

With all of these things in mind, our attention turns to the ternary Fe-based compounds LuFe₂Ge₂ and YFe₂Ge₂. Both compounds crystallise in the ThCr₂Si₂-type (I4/mmm) structure (shown in figure 5.2), and given that Lu is isovalent to Y but with fewer core states, LuFe₂Ge₂ can be considered a high pressure analogue of YFe₂Ge₂. Magnetically, however, the two systems differ. Whilst YFe₂Ge₂ is paramagnetic, LuFe₂Ge₂ has been shown to order antiferromagnetically below a Néel temperature of $T_N = 9$ K [111]. Through neutron scattering measurements [112], the order has been shown to be short-range at ambient pressure, and long-range as the pressure is increased. At 0 kbar, local moments situated on the Fe sites order antiferromagnetically along the \vec{c} -axis.

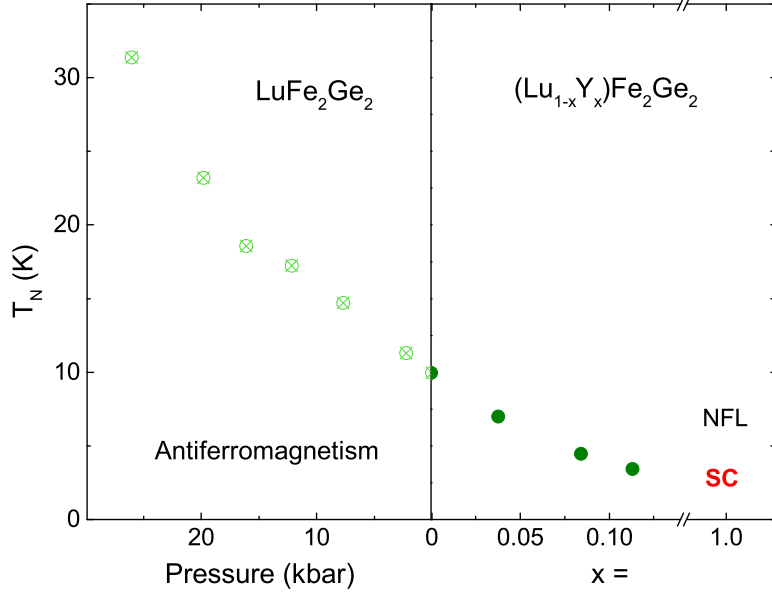


Figure 5.3: Composite doping and pressure phase diagram of YFe₂Ge₂ and LuFe₂Ge₂ from [107] and [112].

Hydrostatic pressure [112] promotes T_N to higher temperatures, whereas negative chemical pressure [107] - by doping on the Lu site with Y - depresses T_N . A composite phase diagram showing the combined effects of chemical and physical pressure is shown in figure 5.3. At a critical concentration $x_c \approx 0.2$ the transition to magnetic order can no longer be identified from the electrical resistivity or magnetic susceptibility. Stoichiometric YFe₂Ge₂ sits some way out to the right-hand side of this phase diagram at $x = 1$.

Both compounds have large Sommerfeld coefficients ($\gamma \approx 100 \text{ mJ}\cdot\text{mol}^{-1}\cdot\text{K}^{-2}$) in their heat capacities [113], as shown in figure 5.4. The Sommerfeld term is given by the linear-in- T contribution to $C(T)$, and can be determined by the residual C/T value at low temperatures. γ is a useful quantity as it gives a direct measure of the density of states at the Fermi level [114] -

$$\gamma = \frac{\pi^2 k_B^2}{3} g(\epsilon_F). \quad (5.1)$$

Systems with large $g(\epsilon_F)$ are more prone to electronic instability, such as mag-

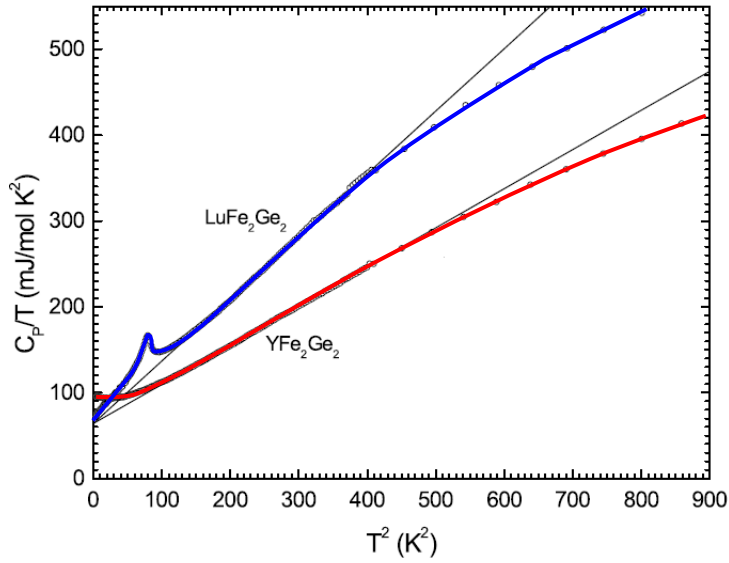


Figure 5.4: Heat capacity of LuFe₂Ge₂ and YFe₂Ge₂ from [113].

netism or superconductivity. The iron-pnictide superconductor KFe₂As₂ displays a similarly high value [115]. Band structure calculations estimate $\gamma = 10 \text{ mJ}\cdot\text{mol}^{-1}\cdot\text{K}^{-2}$ [116], meaning that the enhancement of γ seen experimentally may be due to the effects of correlation, which are not taken into account in the calculation.

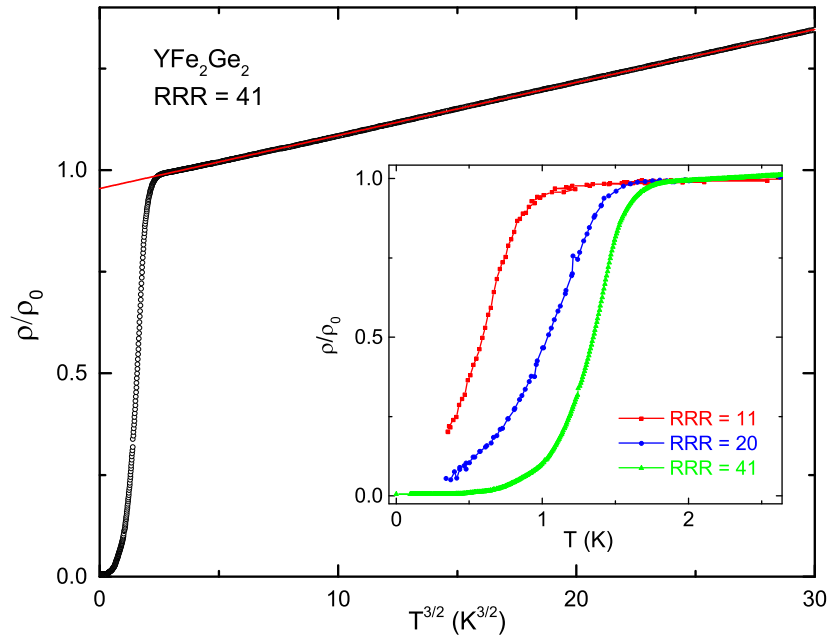
Previous work within the group by Zhuo Feng and Yang Zou [2, 93, 117] has revealed a number of anomalous low temperature behaviours in YFe₂Ge₂. At temperatures below 15 K, the electrical resistivity $\rho(T)$ shows a subquadratic temperature dependence: $\rho - \rho_0 = AT^x$ with $x \approx 1.6$, shown in figure 5.5 (a). Non-Fermi liquid (NFL) exponents such as these are often taken as hallmarks of enhanced quasiparticle scattering due to quantum critical fluctuations [73]. The low- T heat capacity - shown in figure 5.5 (b) - shows an upturn below 10 K, also characteristic of NFL behaviour.

Most strikingly, $\rho(T)$ shows a transition to zero resistance below a critical temperature of around 1.5 K (figure 5.5), suggesting that the sample may become a superconductor at low- T . This would be akin to the SC which appears in the related compounds SrPd₂Ge₂ [118, 119] and SrPt₂Ge₂ [120] with critical temperatures of 2.6 and 10.2 K, respectively.

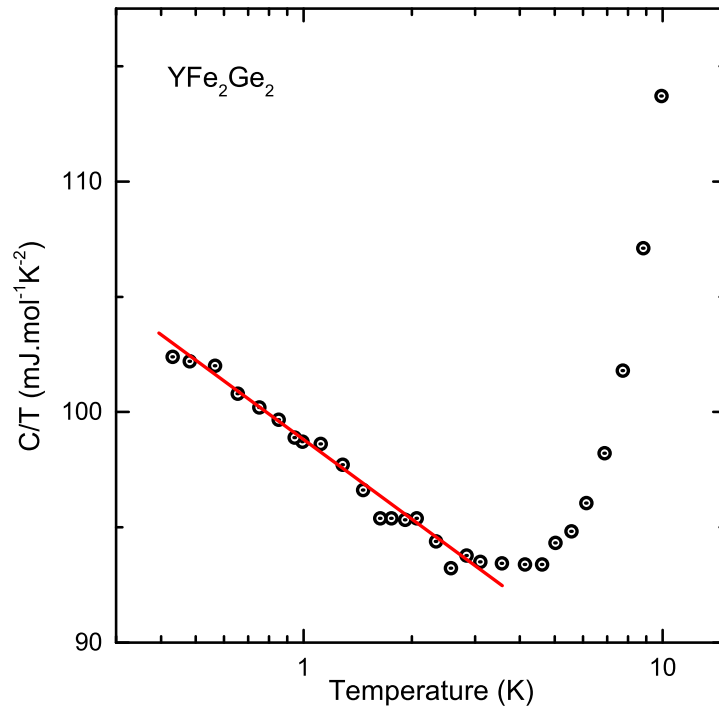
Clear correlation is found between the RRR and the transition temperature T_c , implying that the resistive anomaly may be due to a bulk, as opposed to an impurity, phase. However, electrical resistivity is not useful as a bulk measurement as a superconducting surface layer will short-circuit the bulk. An infinitesimally small amount of surface contamination could result in a partial or even full transition to zero resistance if there existed a “dirty” pathway between the electrical contacts. DC-magnetisation or specific heat measurements detect bulk properties, and as such are more suited to confirming a SC phase.

Our aims for this study are as follows:

1. Perform DC-magnetisation measurements on YFe₂Ge₂ to investigate its magnetic properties down to 280 mK.
2. If a diamagnetic signal consistent with SC is found to be present, determine the nature of the phase: whether the superconductivity is of type-I or II, the associated critical fields and the likely gap structure.



(a) Superconducting anomaly and $T^{3/2}$ dependence of $\rho(T)$. Inset shows the enhancement of the T_c as the purity increases.



(b) Semilog plot of C/T . Straight line is a guide to the eye to highlight anomalous upturn down to the lowest temperatures.

Figure 5.5: Non-Fermi liquid signatures appearing in the electrical resistivity and the heat capacity of YFe₂Ge₂.

5.2 Synthesis and characterisation

The samples measured in this chapter were grown by previous PhD students of the Quantum Matter group, Zhuo Feng and Yang Zou, and an undergraduate, Jiasheng Chen. Both single and polycrystalline samples have been grown, via flux growth and RF induction respectively, although this chapter focusses mainly on magnetic measurements of the polycrystals.

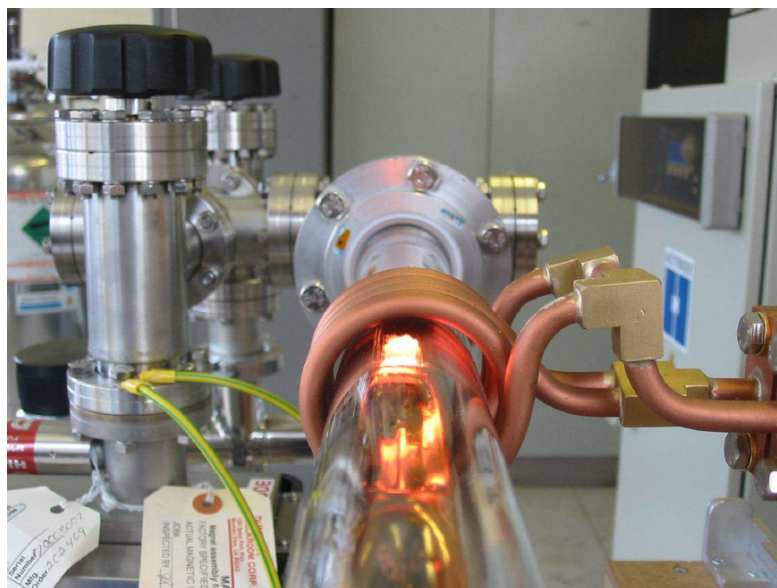


Figure 5.6: RF induction furnace.

The ingredients for the melt are placed in a water-cooled copper boat housed within an evacuated (or Argon loaded) quartz tube. This sits in the centre of coil through which a high-power RF signal ($f = 50 - 120$ kHz) is driven. The induced AC-magnetic field induces eddy currents within the sample, resulting in ohmic heating, causing the constituents to eventually melt together. Samples produced by this technique are typically polycrystalline, and it can be difficult to achieve good homogeneity on growths due to the thermal gradients in the melt-zone and the variation in coupling to the EM field between different melt-components. In the present case, the samples were melted together in the correct stoichiometry, before being annealed under high vacuum at 800 °C. The length of the annealing

stage varied for different growths, which had a great influence on the quality of the samples produced. In particular, it was found that samples which had been annealed for the longest showed the lowest amount of magnetic background, attributed to unreacted iron. This is seen in the magnetisation as the presence of a finite (and sometimes large) saturated moment - M_{sat} - at low fields and at all temperatures. The summary table at the end of this section shows the variation in M_{sat} across a number of different growths and samples.

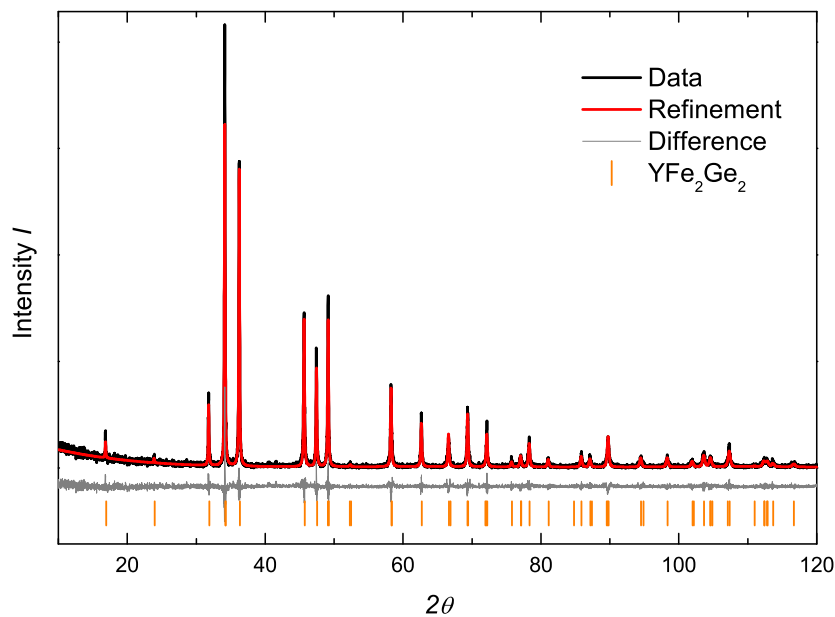


Figure 5.7: Powder XRD spectra from a typical sample of YFe₂Ge₂.

The best samples produced so far (those with the lowest M_{sat} , or the largest superconducting volume fractions) came from RF batches which had been annealed for 9 and 14 days. For the 9 day anneal, a section of the ingot is placed into a quartz tube which is then pumped down to a low vacuum. It is then placed in the normal furnace and heated to 800 °C in one hour, kept at this temperature for 9 days, and then cooled back to room temperature also an hour. For the 14 day anneal the process was identical, except that the sample was heated to 800 °C

over six hours and then held there for 14 days, before being cooled back to room temperature over 20 hours.

The samples grown were characterised via a combination of transport, magnetic, SEM and diffractive measurements. The powder XRD measurements were performed by Yang Zou and Giulio Lampronti of the Earth Sciences department in Cambridge. Generally, samples were found to have a phase purity of around 98-99%, with some samples showing inclusions of elemental iron, or a hexagonal phase of Y-Fe-Ge with stoichiometric ratio 0.5-3-3. Figure shows a typical spectrum. Energy Dispersive X-Ray Spectroscopy (EDAX) was performed on the surfaces of the samples using a Scanning Electron Microscope (SEM) in the microscopy suite of the Cavendish Laboratory. This probe bombards the sample surface with electrons, resulting in the emission of x-rays. By analysing the characteristics of the x-ray emissions, the likely stoichiometry of the region of the sample being bombarded can be determined. Various spots across the surface of the sample were looked at, and whilst some darker spots on the surface were more Fe:Ge abundant, generally a good 1:2:2 ratio is found.

Magnetic characterisation measurements are shown in figure 5.8. Up to the presence of a finite ferromagnetic background - as a result of finite Fe inclusions - they agree with those in the literature [113]. Namely, a static magnetic susceptibility $\chi(T)$ which is only very weakly temperature dependent, and a totally paramagnetic magnetisation $M(H)$. The abundance of Fe impurities varied greatly across different growths, although it was found that samples which had been annealed the longest showed the lowest ferromagnetic background. A complete breakdown of all magnetic characterisation measurements is shown in table 5.1, which shows all samples measured which gave a diamagnetic response in the magnetisation.

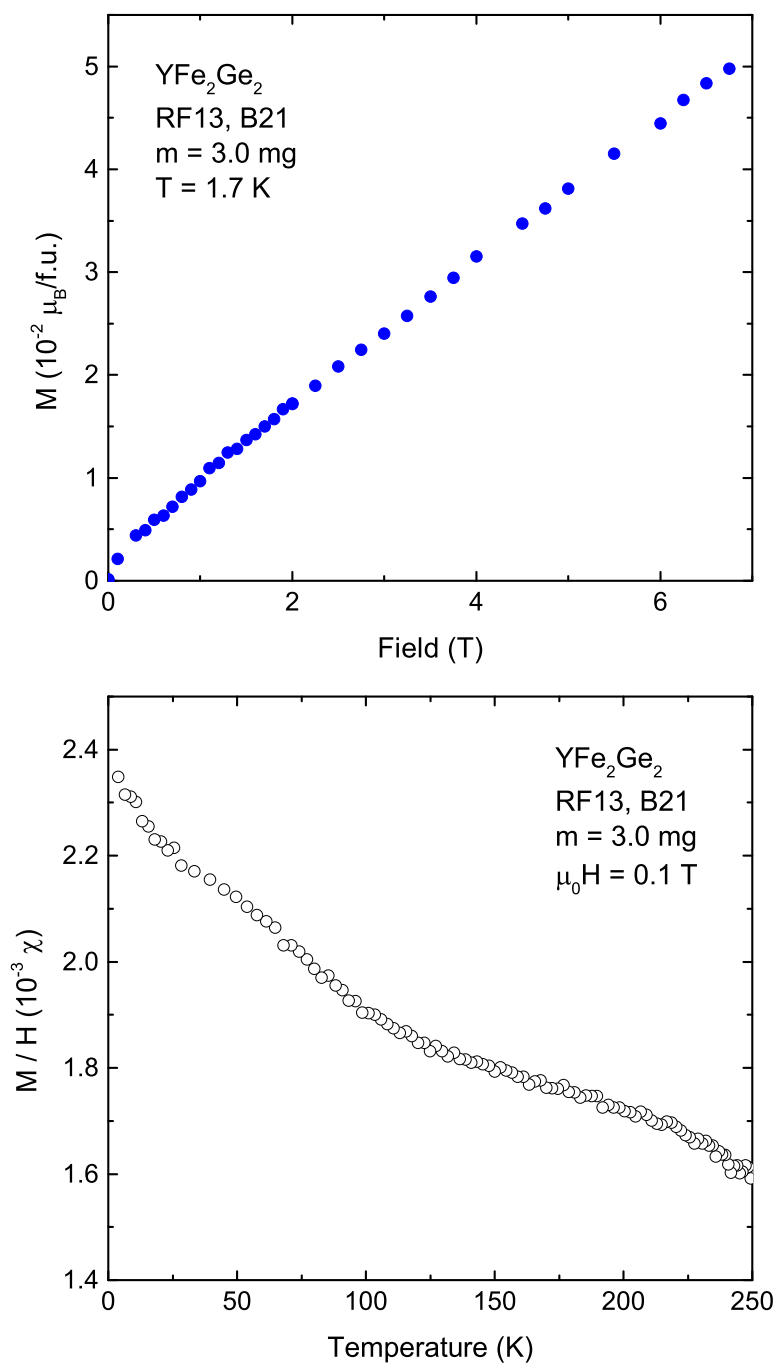


Figure 5.8: Temperature and field-dependent magnetisation measurements to characterise samples of YFe₂Ge₂.

Table 5.1: Summary of magnetic measurements

Batch	Sample	Annealed?	Mass (mg)	Bulk/Powder	M_{sat} ($10^{-2}\mu_B$ /f.u.)	% SC
<i>RF7</i>	a.1	–	1.7	Bulk	4	–
<i>RF7</i>	a.2.4	–	6.8	Bulk	2.4	6
<i>RF8</i>	a.1.2	Yes (2d)	3.8	Bulk	35	25
<i>RF8</i>	a.3.1	Yes (2d)	24.9	Bulk	20	–
<i>RF9</i>	D01	No	21	Bulk	30	–
<i>RF9</i>	D01	Yes (14d)	21	Bulk	20	–
<i>RF9</i>	E02	Yes (9d)	3.5	Bulk	0.1	1
<i>RF9</i>	E03	Yes (9d)	3.3	Bulk	0.3	3
<i>RF10</i>	B01	No	9.1	Bulk	8	0.3
<i>RF13</i>	B01	Yes (14d)	38.8	Bulk	2.5	80
<i>RF13</i>	B01	Yes (14d)	19	Powder	0.7	15
<i>RF13</i>	B01	Yes (14d)	10.6	Bulk	3	55
<i>RF13</i>	B19	Yes (14d)	15.7	Bulk	0.1	30
<i>RF13</i>	B20	Yes (14d)	12	Bulk	–	15
<i>RF13</i>	B21	Yes (14d)	12	Bulk	0.25	20
<i>FZ</i>	–	–	262.2	Bulk	0.2	–
<i>FZ</i>	e1	–	10.6	Bulk	0.4	0

5.3 Diamagnetism in the magnetisation

5.3.1 Temperature dependence

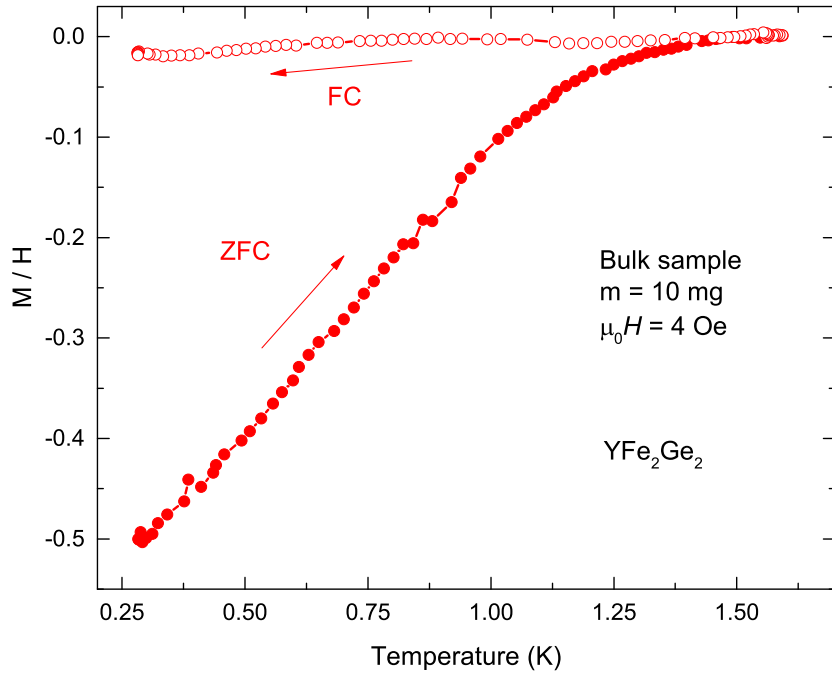
Figure 5.9a shows a typical $M(T)$ curve, in this case for sample *RF13, B01*². The measurement is made by zero-field cooling (ZFC) the sample down to low- T , applying a field and then sweeping the temperature up and then back down. The data collected on cooling the sample is known as a *field-cooled* measurement (FC) as the sample is fully penetrated by the field before it goes through the transition.

A clear diamagnetic feature is found in $M(T)$ which sets in at a temperature $T_c \approx 1.5$ K. This is in good agreement with the critical temperature seen in the electrical resistivity. The full dots in figure 5.9a correspond to the ZFC data obtained on warming the sample, whilst the open dots show data when cooling from above T_c , where the sample is initially fully penetrated by the field. The hysteresis found between the ZFC and FC runs is a generic feature of type-II superconductivity, where flux-pinning is present within the sample [121–123].

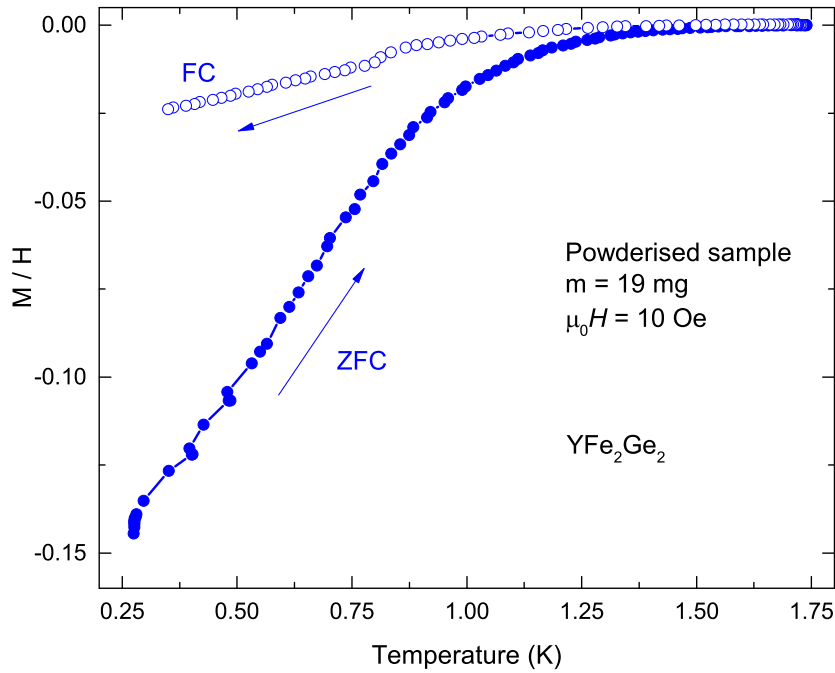
The traces shown in these plots have been offset to the $M/H = 0$ axis for temperatures above T_c , such that only the diamagnetic response is shown - the raw data sits upon a finite positive signal from the ferromagnetic iron inclusions within the sample. For figure 5.9a an offset of 6.43 was subtracted from the raw data, and for figure 5.9b an offset of 0.58 was subtracted. The temperature dependence of the susceptibility of iron in this temperature regime has been taken as approximately constant. The enormous variation in the magnetic background between different samples reflects their inhomogeneity, which is reflected also in the broadness of the anomaly at T_c .

The trace given in fig. 5.9a shows a volume fraction of 50 % at 275 mK, although we have found a very wide variation in this value across our samples. This can be seen in the summary table from the previous section. No sample has so far shown a full transition in the magnetisation, i.e. $M(T)$ has not saturated at the lowest temperatures. Some samples show a slight “plateauing” of $M(T)$ on approaching

²The *RF*- labels the radio-frequency growth number and the *B*- labels the individual sample.



(a)



(b)

Figure 5.9: Comparison of $M(T)$ for bulk (a) and powdered (b) YFe₂Ge₂. Clear flux exclusion is seen beneath a critical temperature $T_c \approx 1.5$ K. M and H are both expressed in SI units such that full diamagnetism would give $M/H = -1$.

base- T , but most show a linear-in- T downturn at all $T < T_c$. To calculate the volume of the sample, and consequently the magnetisation ($M = \mu/V$) we use the mass of the sample as measured in the lab, and the density determined by XRD measurements.

The temperature dependent magnetisation $M(T)$ reflects the temperature dependence of the penetration depth $\lambda(T)$, which in turn - as described in chapter 2 - is determined by the gap structure $\Delta(\vec{k})$. Consequently, the linearity of $M(T)$ in YFe₂Ge₂ could be due to an unusual pairing symmetry.

For example, d -wave superconductors such as the ceramic HTSC's show a linear-in- T dependence of $\lambda(T)$ [124] due to the closing of the gap along the line-nodes of the Fermi surface. However, the broad transition in $M(T)$ could also be a result of T_c varying across the sample, perhaps due to inhomogeneity within the polycrystal.

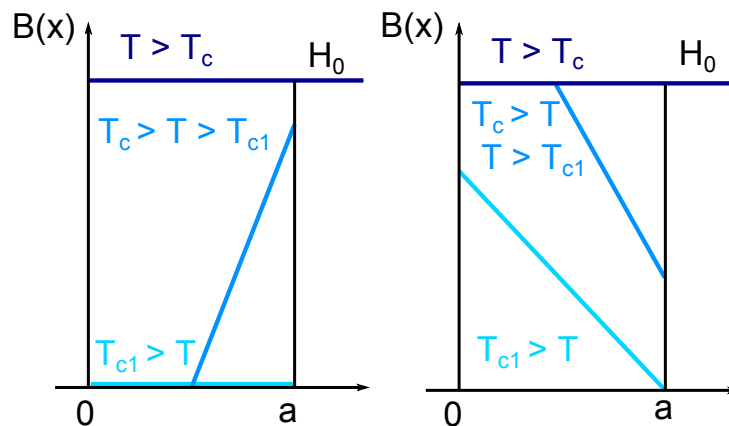


Figure 5.10: Schematic showing the spatial variation in the flux density $B(x)$ as the temperature is changed. Left: warming (ZFC). Right: cooling (FC). unimpeded, and by $T = T_{c1}$ we recover the Meissner condition $B = 0$ and

As for the difference between the field-cooled and zero-field cooled signal, Clem et al [125] have given a complete pedagogical explanation of such curves, in which they show that when there is flux-pinning present within the sample, the field-cooled volume fraction is *necessarily* less than the zero-field-cooled volume fraction. This is detailed more fully in the appendix, although we will address some key points here.

A sample which has been zero-field cooled through T_c will completely shield the flux from any applied field $H_0 < H_{c1}(T = 0)$. Turning on the field sets up persistent supercurrents flowing within λ_L of the surface, such that $B = 0$ throughout the interior. Upon warming, this continues up to the temperature T_{c1} where the field H_0 becomes equal to the lower-critical field - $H_0 = H_{c1}(T_{c1})$. Here, flux-lines begin to enter the bulk, nucleating from the sample surface. In the absence of pinning, these flux lines would move freely, distributing themselves homogeneously throughout the sample. However, in a real system, impurities and defects act as impediments, tending to “hold on” to the flux lines. As shown in figure 5.10, this causes a “build-up” of B near the sample edges as flux-lines gradually “leak” into the sample. The spatial gradient in $B(x)$ is proportional to the strength of the pinning forces, as weakly pinned flux lines are more able to move to the sample interior, reducing the “build-up”, meaning that a sample which pins weakly will become fully penetrated by the field more rapidly, as there is less of a “build up” at the edges.

Above the critical temperature the sample is fully penetrated by the applied field. As the sample is field-cooled back through T_c , flux is gradually expelled from the sample edges. However, as when warming, the variation in the flux profile across the sample is dictated by the strength of the pinning forces. At the sample exterior - where the pinning forces are effectively zero - the flux lines can leave unimpeded, and by $T = T_{c1}$ we recover the Meissner condition $B = 0$ and $M = -H$. However, throughout the rest of the sample, the presence of the pinning forces puts a restriction on how rapidly $B(x)$ may decay away to the sample surface, meaning that by $T = T_{c1}$ whilst $B = 0$ at the exterior, if pinning is present $B(x)$ has to be finite on the sample interior. The flux which still threads the sample by T_{c1} becomes “frozen-in” as T is lowered further, and as a result the FCC fraction - when flux-pinning is present - will *never* be as large as the ZFC fraction. This is shown in figure 5.11 (b), taken from [125], which shows the dependence on the ratio between the ZFC/FC fractions on the pinning strength. When the pinning forces go to zero, B will always take its equilibrium value within the sample, and the ZFC/FC runs become totally identical.

It is feasible that a sample whose surface was contaminated with a superconducting

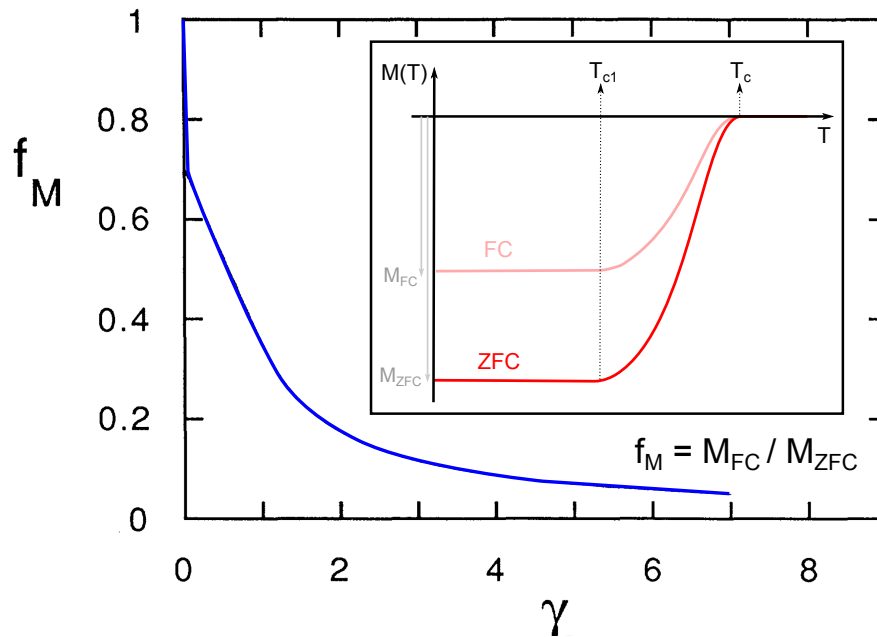
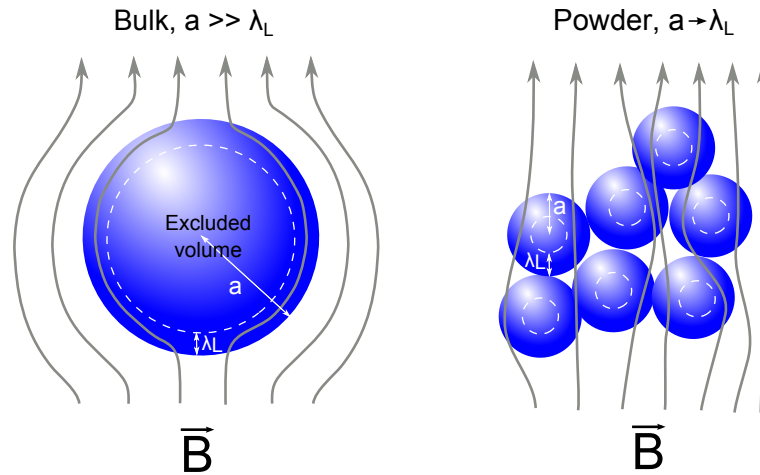


Figure 5.11: From [125] - the anisotropy between FC and ZFC sweeps - f_M - as a function of the pinning strength - γ .

impurity could still shield some amount of flux, although the effect should be destroyed if the sample is powderised. To eliminate this possibility in our study, a sample showing a large volume fraction was powderised in a pestle and mortar before being remeasured in the magnetometer - figure 5.9b shows the corresponding $M(T)$ curve. Whilst the volume fraction is reduced, the diamagnetic signature remains, indicating that the SC phase corresponds to a bulk, rather than a surface phase.



(a) Schematic showing bulk and powdered samples in a magnetic field.

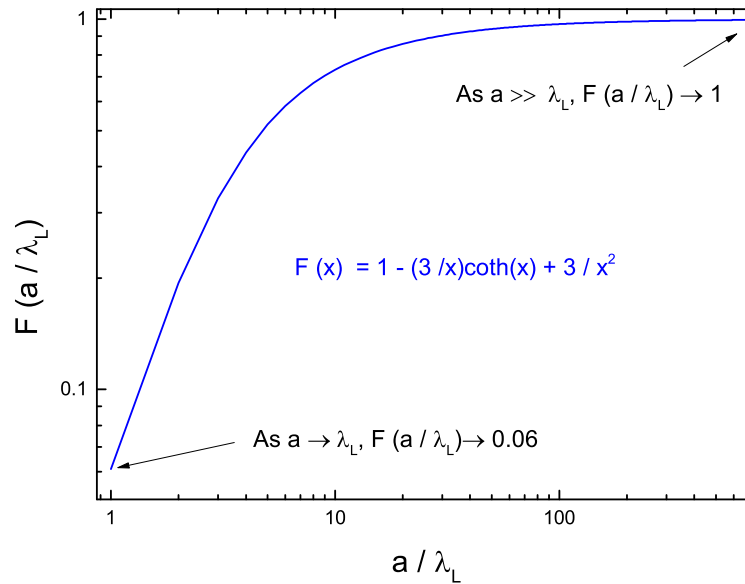
(b) Functional form of $F(a)$ as given in equation 5.3.

Figure 5.12: Effects of sample size on magnetic response.

It was found that the volume fraction in the powder reduced to about 15% from the 60% seen in the bulk parent sample. This reduction is understood to be a necessary consequence of the sample dimensions moving closer to the London penetration depth λ_L . As shown in figure 5.12a, for a fixed λ_L , smaller samples have proportionally less volume where $B = 0$, as the thickness of the shell where $B \neq 0$,

is the same. This means that a smaller volume is shielded. For superconductive particles of size a , the following expression [126,127] describes reduction of the magnetic moment μ as $a \rightarrow \lambda_L$

$$\mu = \tilde{\mu} F\left(\frac{a}{\lambda_L}\right) \quad (5.2)$$

where

$$F(x) = 1 - \frac{3}{x} \coth(x) + \frac{3}{x^2} \quad (5.3)$$

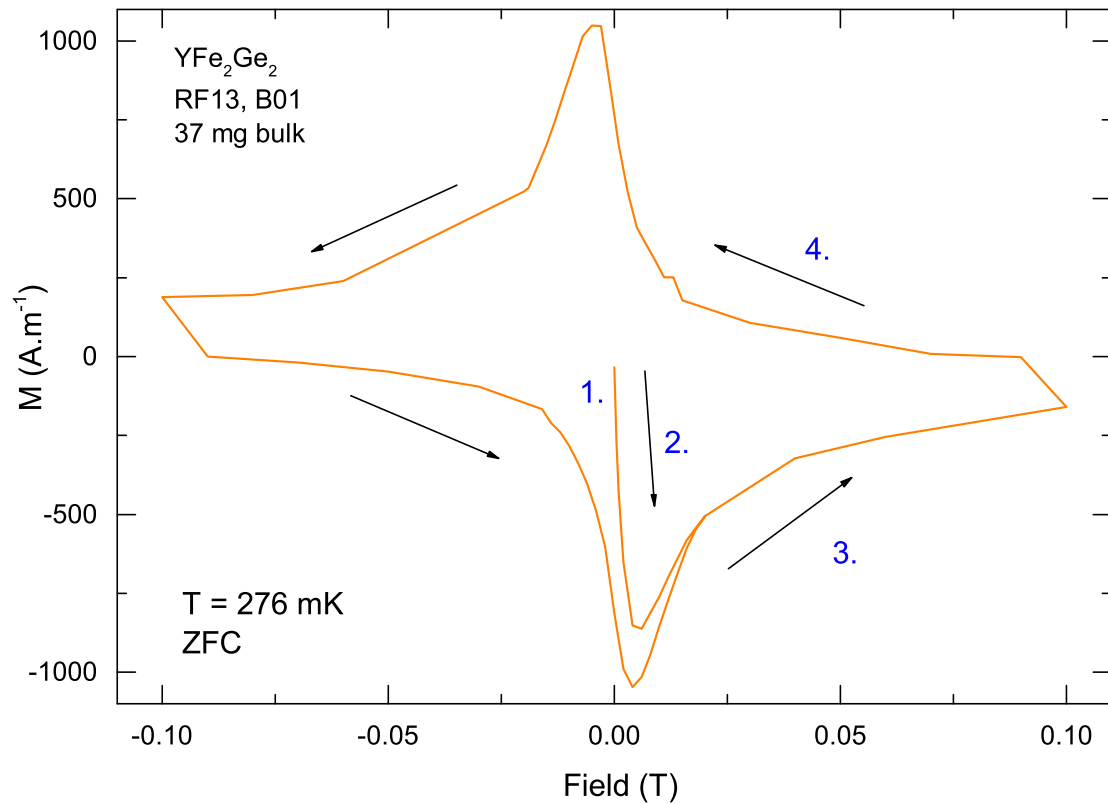
and $\tilde{\mu}$ is the limiting magnetic moment when $a \gg \lambda_L$. The form of $F(a)$ is shown in the log-log plot figure 5.12b demonstrating the reduction of the moment as $a \rightarrow \lambda_L$. This expression can be used to estimate the size of particles in a powderised sample, by comparing the reduction in the measured moment to the corresponding value of a/λ_L .

5.3.2 Field dependence

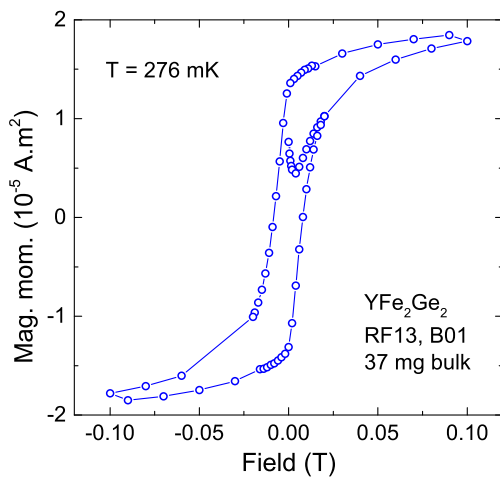
To extract the upper and lower critical fields we need to look at the field-dependent magnetisation $M(H)$, taken at a constant temperature. An isothermal field sweep at $T = 276$ mK is given in figure 5.13a. As has been mentioned already, the samples grown so far have all shown some amount of ferromagnetic background due to the presence of residual unreacted iron in the final ingot. This was not an issue for the temperature dependent measurements shown in figure 5.9 as the variation in the magnetic susceptibility of pure iron in this temperature regime is negligible. However, the iron does show FM hysteresis during the low-field loop, which must be subtracted from the raw data to reveal the response of the superconducting YFe₂Ge₂.

Figures 5.13b and 5.13c show the raw signal as measured by the SQUID at temperatures above and below the diamagnetic transition. As has already been reported in the literature [113], the magnetic response of YFe₂Ge₂ in its normal state is that of a weak paramagnet. The strong ferromagnetic hysteresis we measure at $T = 1.7$ K should then be attributed to the Fe with the sample. To extract the field dependence of the diamagnetic phase in YFe₂Ge₂, identical field sweeps were performed at temperatures above and below T_c . The high-temperature sweep was then subtracted from the low-temperature sweep - point-by-point - to reveal the hysteresis loop shown in figure 5.13a. Again, this approach assumes that the magnetic response of the Fe inclusions has no significant temperature dependence³.

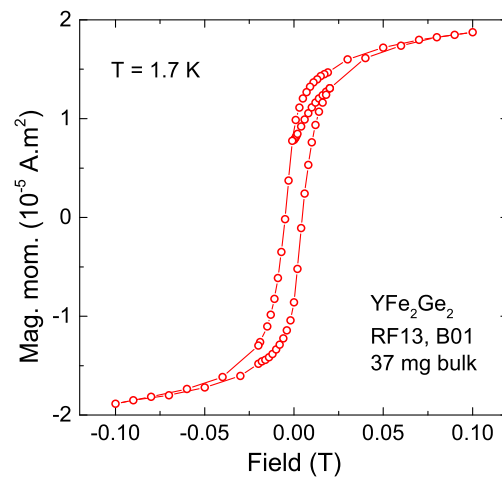
³Samples have been measured which show clear the superconducting hysteresis clearly even without the background subtraction, but the data from this sample as it produced a particularly convincing loop - even with a significant magnetic background present - due to its large superconducting volume fraction (80%).



(a) Isothermal magnetic field sweep for the superconducting YFe₂Ge₂. Arrows show direction of loop.



(b) Raw magnetisation data taken at $T = 276$ mK ($T < T_c$).



(c) Raw magnetisation data taken at $T = 1.7$ K ($T > T_c$).

Figure 5.13

Such a curve identifies YFe₂Ge₂ immediately as a type-II superconductor with pinning present [18]. As before, a more thorough description of these hysteretic effects is given in the appendix, although we will explain the main features of the loop here. For each of the regions 1-4 shown in figure 5.13a:

1. Along the virgin curve exists a totally reversible portion of $M(H)$, extending from $H = 0$ to $H = H_{c1}$. In this region, persistent shielding supercurrents are contained within λ_L of the surface, such that $B = 0$ in the bulk.
2. Quantised flux lines enter bulk from sample exterior. The rate at which the sample is penetrated by the field is governed by the ability of the pinning sites to hold the flux-lattice fixed against the destabilising Lorentz forces. M reaches a minimum when the flux-fronts meet in the sample centre - the field has penetrated the sample fully.
3. Increasing the field further continues to strengthen the Lorentz forces, whilst the strength of the pinning forces remains constant. Consequently, an ever-smaller critical current can be maintained, which reduces the magnitude of M .
4. Reducing the field induces currents in the opposite direction. By $H = 0$ the sample retains a finite magnetisation due to the persistent supercurrents still threading the sample.

We now look to try and extract $H_{c1}(T)$ and $H_{c2}(T)$ from our data. In the first place, we focus on the low-field region of our isotherms to identify the boundary of the Meissner and Abrikosov states, the first field at which $M \neq -H$. More detail on the various ways to extract H_{c1} is given in the appendix. Figure 5.14 shows a selection of low-field isotherms at various temperatures.

All methods of extracting H_{c1} given in the appendix fail here. At the finest field-resolution available (0.5 Oe) there is no appreciable field range in which $M(H)$ is linear in H , as can be seen in the derivative dM/dH , shown in the inset of figure 5.14. For fields $H < H_{c1}$ traces at all temperatures should overlap each other (have the same gradient). In figure 5.14 no two $M(H)$ sweeps coincide in any field range or at any temperature.

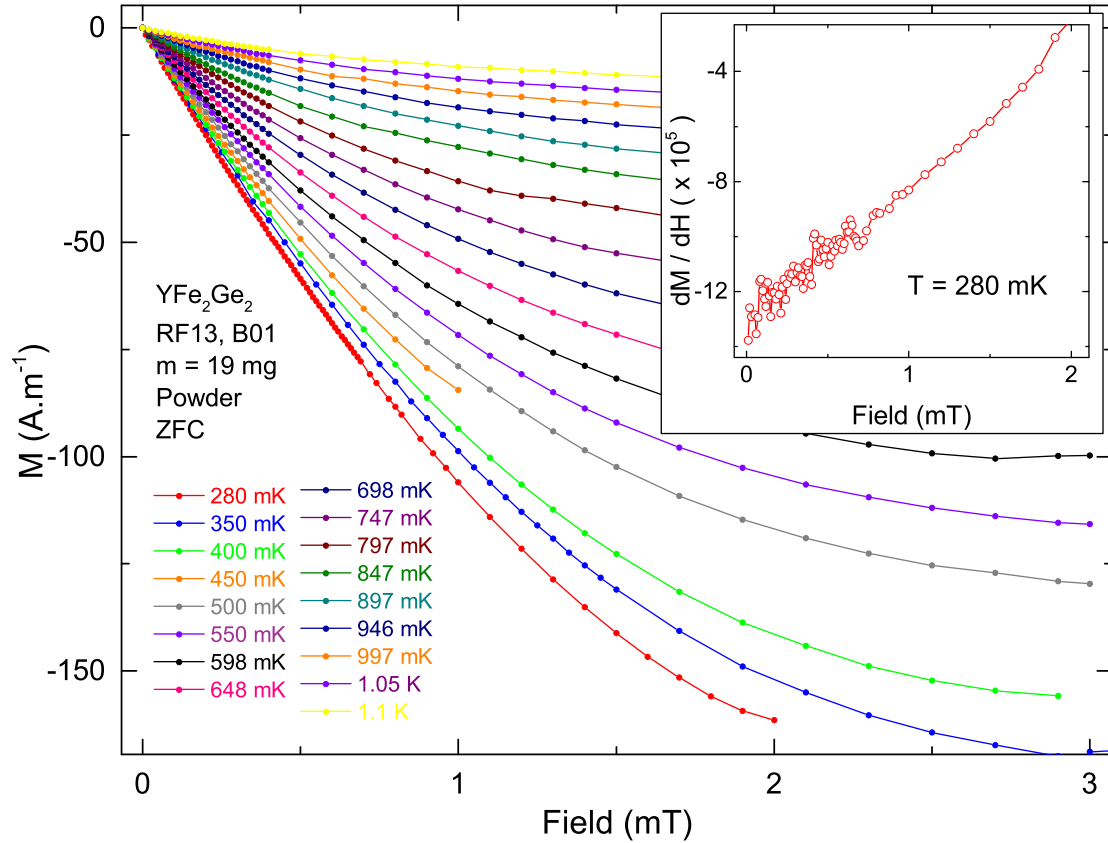


Figure 5.14: Low field $M(H)$ curves at various temperatures.

Whilst the FM background has been removed from these traces (by subtracting a field sweep taken at $T > T_c$) it may be that the peculiar behaviour of $M(H)$ at low- H is not intrinsic but due to a background effect not properly accounted for. It may not be possible to investigate the lower critical field properly until better quality samples have been grown.

The combined ferromagnetic background and less-than-100% volume fraction, makes it difficult to resolve the superconducting component of the signal at high fields. Instead, H_{c2} is determined from a series of resistive measurements made by Yang Zou. The phase boundary described by her data is shown in figure 5.15 from which data we can extract the limiting upper critical field at zero temperature as $H_{c2}(0) = 1.75$ T, and the value of the gradient⁴ $dH_{c2}/dT_c|_{H=0} = 2.3$ T.K⁻¹.

⁴This is an important parameter which enters into the WHH theory of the upper critical field

As in the theory chapter, we can evaluate the hypothetical critical fields associated with various pair-breaking mechanisms such as the Pauli limiting field, along with the orbital-limit for clean and dirty samples. From equation 2.23, where we use the BCS expression for the gap $\Delta_0 = 1.764k_B T_c$ and taking $T_c = 1.6$ K - gives the Pauli limited field $H_P = 2.97$ T, whilst from equation 2.22, the orbital limit field in the clean and dirty limits give 2.61 T and 2.49 T, respectively.

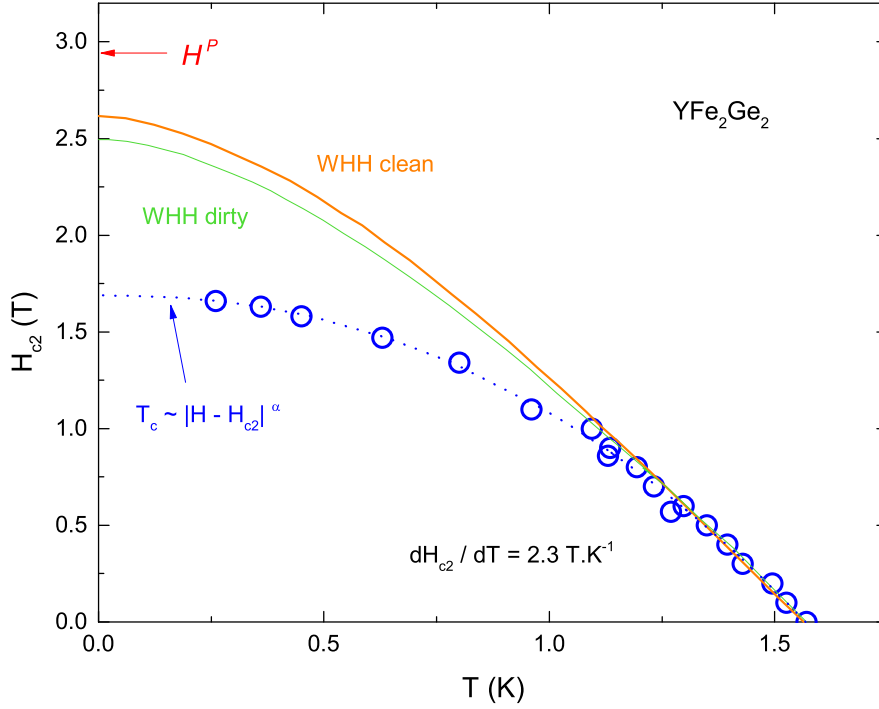


Figure 5.15: $H_{c2}(T)$ for YFe₂Ge₂ as determined from resistivity measurements [2]. The orange and green curves show the WHH result in the clean and dirty limits, and the blue dotted line is a fit to $T \sim |H - H_{c2}|^\alpha$, with $\alpha=0.64$. The Pauli-limited field H_P is also shown.

That both the orbital *and* the Pauli limiting fields exceed the experimental upper critical field leaves some ambiguity as to the dominant pair-breaking mechanism. In Fe-based systems it is often the case that the Pauli effect is more important than the orbital one, and so it is likely that our estimate of H_P is too high. This may be due to our selection of the BCS value of the gap Δ_0 in the expression for [23].

H_P :

$$H_{c2}^P = \frac{\Delta_0}{\sqrt{2}\mu_B}. \quad (5.4)$$

As will be detailed in the discussion, it is possible that the gap is highly suppressed from its BCS value in YFe₂Ge₂ due to the presence of magnetic impurities. This is evident in the heat capacity data - figure 5.5 - which shows no anomaly at T_c .

5.3.3 Derived quantities

We can estimate the Ginzburg-Landau coherence length ξ_{GL} from the upper critical field by [20]

$$B_{c2} = \frac{\Phi_0}{2\pi\xi^2} \quad (5.5)$$

where $\Phi_0 = h/2e$ is the flux quantum. With $B_{c2} = 1.7$ T we find $\xi = 140$ Å. This can be put into some context by evaluating the mean-free-path, using an expression given in an exhaustive list of BCS parameters made by Orlando et al [128]:

$$l = 9 \times 10^{11} \hbar (3\pi^2)^{\frac{1}{3}} (e^2 \rho_0 4\pi k_F^2)^{-1}, \quad (5.6)$$

where k_F is the Fermi wavevector and ρ_0 is the residual resistivity. k_F may be estimated by assuming a spherical Fermi surface which fills the Brillouin zone, which given the volume of the unit cell $V = 164$ Å³ [113] results in $k_F = 0.6$ Å⁻¹. For the most high purity sample we found $\rho_0 = 4$ μΩcm, resulting in a mean-free-path $l = 700$ Å. As $l > \xi$, YFe₂Ge₂ can be considered to be closer to the clean limit, and as such the possibility remains that the superconductivity in YFe₂Ge₂ may be unconventional. Whilst Anderson's theorem [129] protects the superconducting state against the influence of scattering from non-magnetic impurities in a conventional superconductor, in a *p*- or *d*-wave system impurity scattering mixes together states with *opposite* gap parameters, which may force Δ to zero, reducing T_c [18, 130].

Similar expressions for the London penetration depth gives $\lambda_L = 0.21$ μm, from

which we can deduce the Ginzburg-Landau parameter -

$$\kappa = \frac{\lambda}{\xi} \quad (5.7)$$

as $\kappa = 15$, which consistent with the type-II superconductivity we see in the magnetisation.

Also from [128] the expression for the Fermi velocity $\langle v_F \rangle$ is given by -

$$\langle v_F \rangle = \frac{k_B^2}{\hbar} \left(\frac{\pi^4}{3} \right)^{\frac{1}{3}} \frac{4\pi k_F^2}{\gamma} \quad (5.8)$$

where γ is the Sommerfeld coefficient from the heat capacity - 100 mJ.mol⁻¹K⁻². The corresponding Fermi velocity is $\langle v_F \rangle = 1.2 \times 10^4$ m.s⁻¹, which results in a quasiparticle mass of:

$$m^* = \frac{\hbar k_F}{v_F} = 58m_e. \quad (5.9)$$

5.4 Discussion

A diamagnetic transition consistent with a bulk low-temperature superconducting phase was found in both bulk and powderised samples, whose critical temperature agreed well with that seen in the electrical resistivity. A wide range of superconducting volume fractions were obtained, with a maximum in the ZFC runs of 80%, and typical FC fractions of around 5%. As described in section 5.3, the discrepancy between FC and ZFC signal is an ubiquitous property of type-II superconductors in the presence of flux pinning. Similar data from other systems is shown in figure 5.16

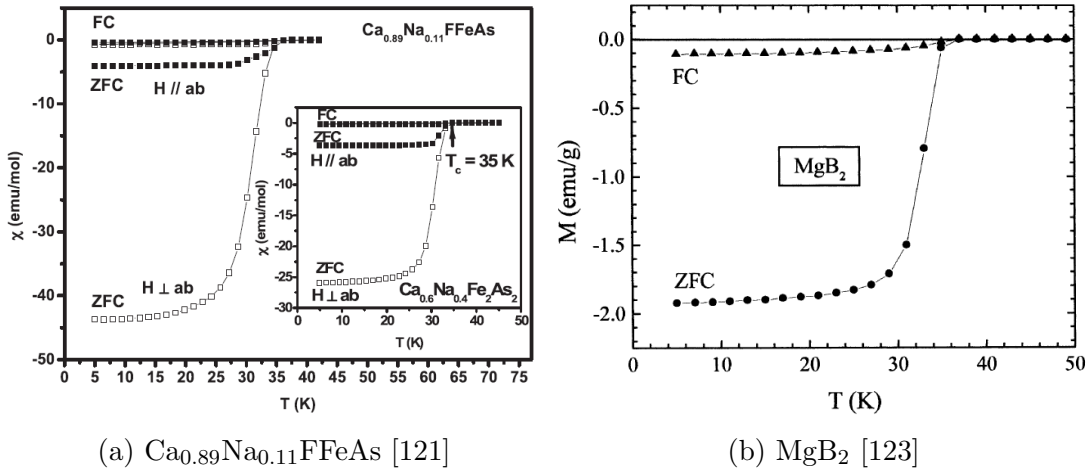


Figure 5.16: Examples of ZFC/FC anisotropy appearing in the DC magnetisation a 1111 compound and MgB_2 .

Strong pinning within the sample is also shown in the strongly hysteretic features which appear in the $M(H)$ curves - see figure 5.13a - revealing YFe_2Ge_2 to be a type-II superconductor. A series of resistivity measurements gave H_{c2} in the zero-temperature limit to be around 1.75 T, and whilst a complete analysis of $H_{c1}(T)$ from $M(H)$ was not possible, it is likely that the lower critical field is of the order $H_{c1} \approx 1$ mT.

The height of the specific heat anomaly at a superconducting transition is proportional to the magnitude of the gap Δ in the density-of-states (DOS) [18]. Our

specific heat data do not show a feature at T_c , pointing towards a suppression of Δ . This may be as a result of magnetic impurities within the sample. Anderson's theorem [129] shows that whilst non-magnetic impurities leave T_c and Δ unchanged, the presence of magnetic impurities has a profoundly deleterious effect upon the formation of Cooper pairs, by breaking the time-reversal symmetry of the up/down spin state. In chapter 2 we saw how the presence of magnetic impurities within the superconductor could – above a critical concentration – totally suppress the gap in the density-of-states, whilst a supercurrent could still be supported.

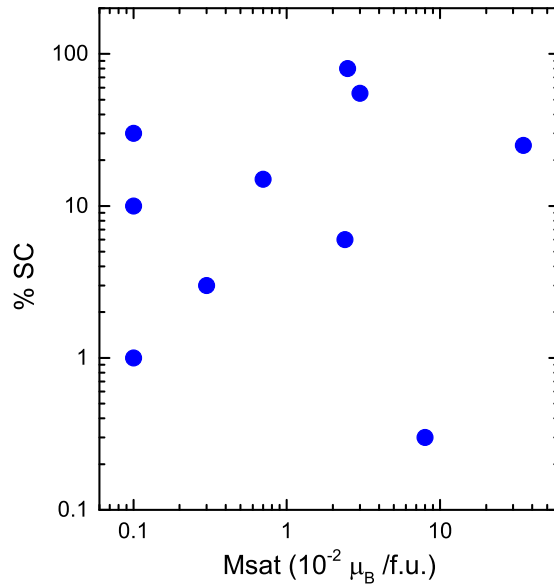


Figure 5.17: Plot of the superconducting volume fraction against the ferromagnetic impurity level for YFe₂Ge₂.

Our samples contain ferromagnetic impurities, and the XRD data suggest that they are likely to be inclusions of unreacted iron. Table 5.1 shows that the samples which were annealed the longest gave the lowest magnetic backgrounds⁵. This is a common issue for crystal growth with strongly magnetic constituents, for example the nickel inclusions in the growth of YbNi₄P₂ crystals [69]. The presence of these

⁵We can perform a straightforward “reality check” on our impurity background we measure using the literature reported magnetisation of elemental iron - $M \approx 200$ emu/g [131], to see that the FM signal we see corresponds to a reasonable amount of Fe. The bulk 10 mg sample *RF13*, *B01*, for example, gave a FM background of $2.5 \times 10^{-2} \mu_B / \text{f.u.}$ - corresponding to 0.74% of unreacted Fe: this seems plausible.

pair-breaking impurities and the absence of a specific-heat anomaly at T_c could be related to one another.

However, if it were the case that a fortuitously critical magnetic impurity concentration was killing off the gap in the density-of-states, we would also expect a correlation between the robustness of the superconducting state and the presence of magnetic impurities. Namely, that samples with the highest backgrounds should show a weakening of the diamagnetic signal or transition temperature T_c . Figure 5.17 shows a log-log plot of the superconducting volume fraction plot against the magnetic background - there is no correlation. Furthermore, all samples gave generally the same transition temperature. Given that the magnetic background spans many orders of magnitude, we would expect that - were the Abrikosov-Gor'kov (AG) "gapless" mechanism responsible - we would at some point exceed the critical concentration n_c at which $T_c = 0$ K. It is more likely that rather than the magnetic impurities existing as dilute pair-breakers immersed in the YFe₂Ge₂ lattice, the unreacted iron sits as larger lumps embedded in-between grains of YFe₂Ge₂, and that the AG mechanism is not at work.

It is then likely that the lack of a specific-heat anomaly is due to the quality of our crystals. The broadness of the transition in $M(T)$ suggests a distribution in T_c across the sample, which then broadens the jump ΔC . Similar problems were found in the early studies of CeCu₂Si₂ [132], or more recently in the seminal compound LaFePO [133]. A new batch of crystals, hopefully of higher quality, are currently are currently being grown which will go some way in resolving this issue.

Having established that YFe₂Ge₂ is a superconductor at low temperatures, the most pertinent question is the origin and nature of the superconductivity. The application of hydrostatic pressure to YFe₂Ge₂ should drive it back towards the doping induced quantum phase transition, said to occur in Y_xLu_{1-x}Fe₂Ge₂ at x_c [107]. High pressure AC-susceptibility measurements from within the group, by Hui Chang and Yang Zou [2] suggest that T_c becomes suppressed fully by 22 kbar, with a maximum in T_c at 10-15 kbar. A miniature anvil cell was also set up for a SQUID measurement, although no diamagnetic signature were found down to 1.8 K in the pressure range up to 60 kbar. That the superconductivity is suppressed

fully by 22 kbar is somewhat at odds with the estimate that the doping-induced QCP should exist at 28 kbar [2]. As regards the symmetry of the superconducting order parameter, careful measurement of $H_{c1}(T)$ can be very revealing [21, 22, 134], although the quality of our data is not sufficiently high that we can perform such analysis. Again, better quality samples may help to resolve this.

System	T_c/K	$\mu_0 H_{c1}/\text{mT}$	$\mu_0 H_{c2}/\text{T}$	$H'_{c2}/\text{T.K}^{-1}$	κ	
YFe ₂ Ge ₂	1.7	-	1.75	2.4	30	[117]
SrPd ₂ Ge ₂	2.7	4.4	0.7	0.27	13.5	[118, 119]
CaPd ₂ Ge ₂	1.7	3.1	0.134	0.115	6.3	[135]
SrPt ₂ Ge ₂	10.2	-	-	-	-	[120]
KFe ₂ As ₂	3.4	-	5(\vec{a}), 1.5(\vec{c})	3.7, 0.6	87, 15	[136]
CeCu ₂ Si ₂	0.6	1.8	1.7	5.8	22	[137]
LaFePO	6.6		6($\parallel\vec{ab}$), 1($\perp\vec{ab}$)	0.9, 0.15	-	[133]
LiFeAs	17.5	20	26(\vec{ab}), 16(\vec{c})	4, 1.4	26, 20	[134, 138]
β -FeSe	9.8	75	18	2.7	11	[22, 139]

Table 5.2: Critical fields and κ values for other type-II superconductors.

Postscript

Since the completion of this thesis, a new batch of YFe₂Ge₂ samples has been grown which show a distinct anomaly in the heat capacity at low temperature. Preliminary data is shown in figure 5.18.

The zero-field data shows a clear anomaly which sets in below 2 K. The overall character of the anomaly is reminiscent of that which would be expected at a superconducting transition [18]. The anomaly disappears when a magnetic field of 1 T is applied, also consistent with it being associated with the onset of superconductivity. The inset shows the feature more closely, and the temperature at which the resistive transition occurs is also marked.

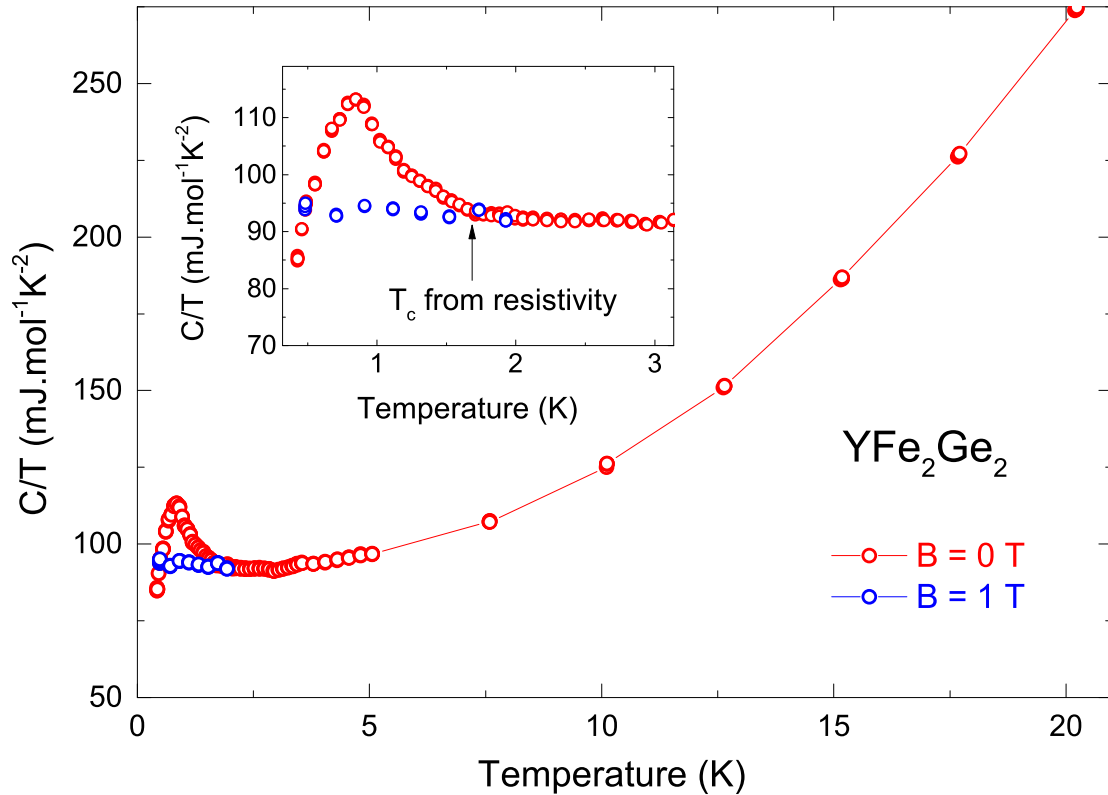


Figure 5.18: Heat capacity of YFe₂Ge₂ from a new batch of flux-grown samples. A clear anomaly can be seen below $T = 2$ K which disappears in the presence of a magnetic field.

This supports the conclusions drawn from the magnetisation measurements in this chapter. A more complete study of this new set of samples is currently underway, which will hopefully reveal more about the nature of the low temperature superconducting phase.

Chapter 6

$\mathbf{R}_3\mathbf{T}_4\mathbf{Sn}_{13}$

The ternary stannide doping series $(\text{Ca}_x, \text{Sr}_{1-x})_3\text{Ir}_4\text{Sn}_{13}$ has been shown [38] to undergo a high-temperature structural transition at temperature T^* . This *superlattice* structure consists of a deformation of the tin icosahedra found at the cell corners and centre, causing a doubling of the size of the unit cell. T^* may be suppressed by doping on the Sr site with isovalent Ca – effective chemical pressure – or by the application of hydrostatic physical pressure. Beyond a critical pressure P_c , T^* extrapolates to zero temperature. A superconducting dome is found at low temperatures, which seems to peak in the vicinity of P_c , along with a quasi-linear temperature dependence in the electrical resistivity over a wide temperature range. The phase diagram then has the appearance of superconductivity being induced in the proximity of a *structural* quantum critical point.

In this chapter we investigate the aspects of the superconductivity in $\text{Ca}_3\text{Ir}_4\text{Sn}_{13}$ and $\text{Sr}_3\text{Ir}_4\text{Sn}_{13}$, along with the related compound $\text{Ca}_3\text{Co}_4\text{Sn}_{13}$.

6.1 Structural instability

A crystal lattice undergoes a *displacive* phase transition when, at a critical temperature T^* , a periodic distortion of its structure takes place, lowering its symmetry [140]. In the *soft mode theory* of displacive phase transition, this is a consequence

of one of the low-lying phonon modes going *soft* at the transition – one of the branches in the dispersion drops to zero energy¹. The softening of the mode corresponds to the frequency of the lattice vibration slowing down. At the point at which the mode goes to zero energy, the lattice undergoes a constant structural displacement - the mode becomes *frozen in* - which brings about a reduction in the symmetry of the structure, and a shrinking of the Brillouin zone.

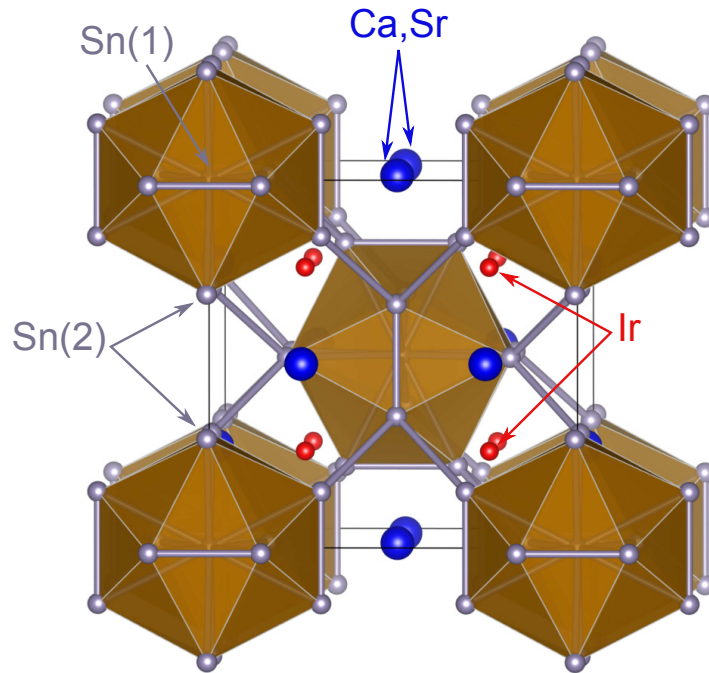


Figure 6.1: Crystal structure of $(Ca,Sr)_3Ir_4Sn_{13}$, taken from [141].

The ternary stannides $(Ca,Sr)_3Ir_4Sn_{13}$ belong to a broader catalogue of compounds which share the 3-4-13 stoichiometry, including heavy fermion materials [142, 143] and thermoelectrics [144]. At room temperature both compounds crystallise in a simple cubic structure - space group $Pm\bar{3}m$. In spite of the 40 atoms which are found within every unit cell, their arrangement can be understood relatively simply, as in figure 6.1. A distinction can be made between the two inequivalent tin positions – Sn(1) and Sn(2) – such that the chemical formula can be written as

¹For a mode to “soften” means that it there is less of an energy cost to excite it, as in a spring whose spring constant k - $m\ddot{x} = -kx$ - is reduced, resulting in the spring “softening” - becoming less stiff. When $k \rightarrow 0$, it costs zero energy to displace the system.

$Sn(1)Ca_3Ir_4Sn(2)_{12}$. Building the structure up from the bottom, the basis of the lattice is a body-centred cubic lattice formed of Sn(1) atoms at the vertices and centre, each surrounded by an icosahedral “cage” of Sn(2) atoms. The eight iridium atoms form a simple cubic structure within each cell, and the calcium/strontium atoms are found on the faces. The other atoms are arranged as shown in figure 6.1 - this is known as the I phase.

An extensive flux-growth study across the family of 3-4-13 stannides by Espinosa in 1980 [145] revealed both $Ca_3Ir_4Sn_{13}$ and $Sr_3Ir_4Sn_{13}$ (amongst many others) to be superconductors. More recently, focus has turned to an anomaly which appears at a higher temperature T^* in the electrical resistivity, magnetic susceptibility [146] and specific heat [147], which was initially attributed to the presence of ferromagnetic spin fluctuations [146]. However, following a comprehensive pressure study by Klintberg et al [38] of $Ca_3Ir_4Sn_{13}$, $Sr_3Ir_4Sn_{13}$ and the intermediate dopings $(Ca_x, Sr_{1-x})_3Ir_4Sn_{13}$, it was shown that the high temperature anomaly corresponds to a transition from the high-temperature I phase into the reduced symmetry, low temperature I' phase. The I' phase has space group $I\bar{4}3d$ [148] and corresponds to a slightly distorted version of the I phase, due to a slight “warping” of the Sn(2) icosahedra, which result in a doubling of the lattice constant.

The structural transition takes place at $T^* = 147$ K and 45 K in the Ca and Sr systems, respectively, and it is possible to move between the two by either applying hydrostatic pressure, or – given the isovalency of Ca and Sr – effective chemical pressure through doping within the unit cell. In the Klintberg study, dopings at $x = 0, 0.5, 0.75$ and 1 were investigated through electrical resistivity and AC susceptibility under pressure. They were able to determine the point of overlap between each successive doping² The full phase diagram of this work is given in figure 6.2.

Studies of the crystal structure showed that additional superlattice peaks appear below T^* , suggesting that the low temperature crystal structure has twice the lattice constant of the I -phase. Single crystal diffraction measurements have found that at T^* there is a distortion of the Sn “cages”, resulting in an increase in

²From looking at the value of T_c one can see that the $x = 0.5$ compound at ambient pressure corresponds to $x = 0$ under about 35 kbar of pressure.

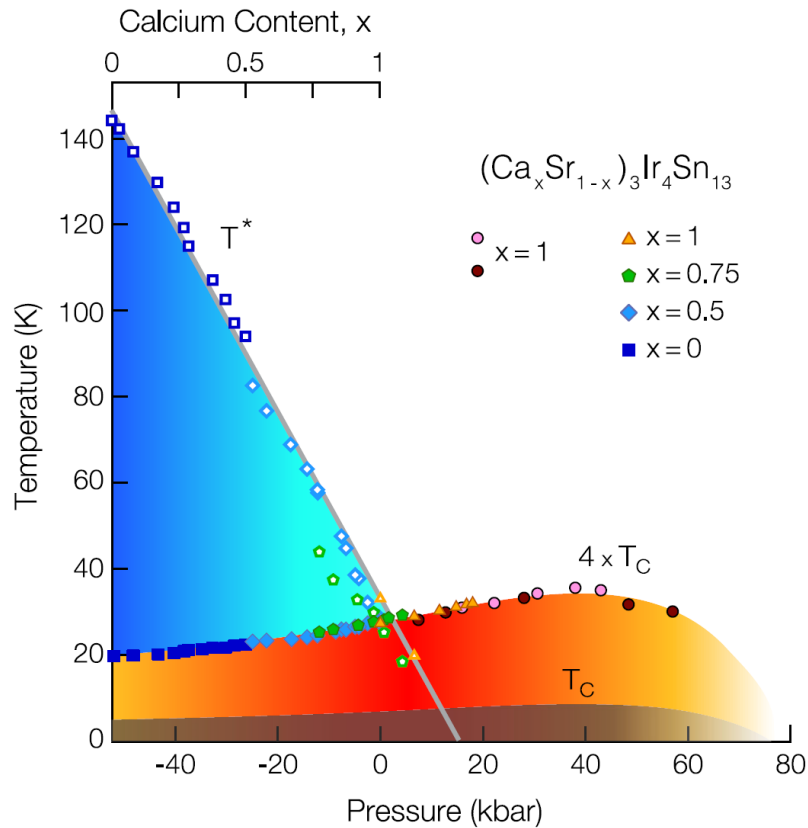


Figure 6.2: Doping and pressure phase diagram of the $(Ca_xSr_{1-x})_3Ir_4Sn_{13}$ series. My own contribution to this publication was to investigate the magnetic anisotropy in these compounds, in order to rule out the possibility that the phase transition taking place at T^* was a magnetic – rather than structural – one. Some of this data is shown in figure 6.4.

the number of inequivalent Sn sites [148]. The temperature dependence of the bond distances Sn(1)-Sn(2i) is shown in figure 6.3b for the strontium system. The new bond length formed at T^* seem to grow continuously out of the critical temperature, and there is nothing to forbid a continuous phase transition between the high and low-symmetry space groups [148]. The shape of the heat capacity anomaly at T^* - shown in figure - also suggests that the transition at T^* is second order.

Given the quasi-linear temperature dependence of $\rho(T)$ and the existence of a superconducting dome peaking near P_c , it would be tempting to consider this

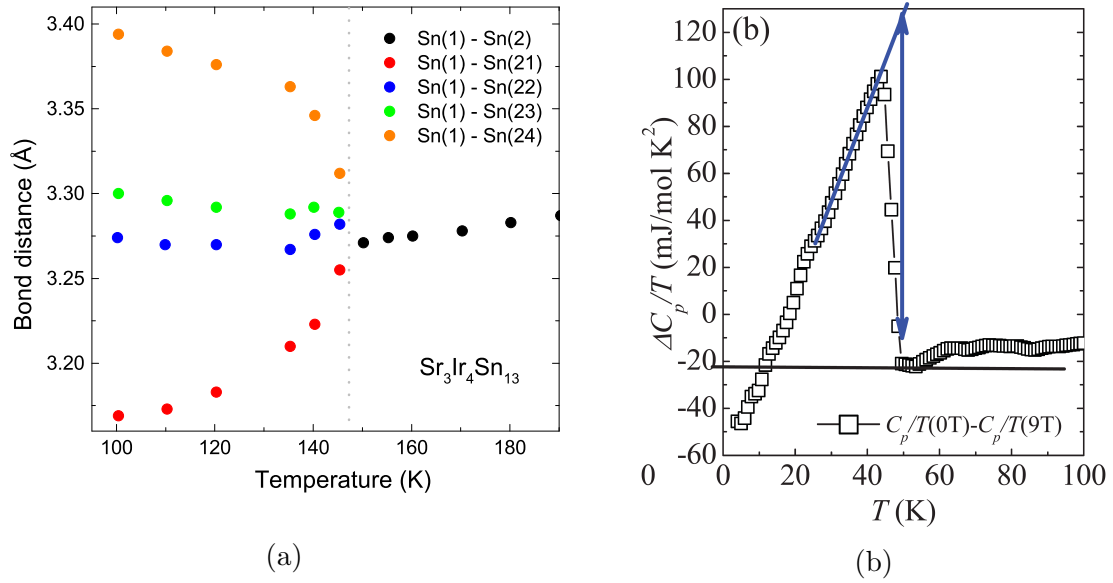


Figure 6.3: (a) Temperature evolution of the Sn(2) bond distances from the central Sn(1) site growing out of T^* , from [38]. (b) Heat capacity of $Ca_3Ir_4Sn_{13}$ from [149], which shows a clear anomaly at T^* .

system as being quantum critical on the border of magnetism. However, band-structure calculations do not support the existence of a magnetic moment [38].

My own study of the temperature dependence of the static magnetic susceptibility along a number of non-orthogonal orientations, *did not* reveal the presence of a significant magnetic anisotropy. This supports the view that the transition taking place at T^* is related to the structural, rather than the magnetic, degrees of freedom. Some of this data is shown in figure 6.4, where the DC response of both compounds is shown along a number of different crystallographic orientations.

A drop in the signal size takes place at the structural transition T^* ; as the real unit cell becomes doubled, the new Brillouin zone cuts through large portions of the high-symmetry Fermi surface, gapping large portions of it out. The resulting reduction in the density of states at the Fermi level $g(\epsilon_F)$ reduce the magnitude of the Pauli susceptibility, as $\chi_P \propto g(\epsilon_F)$. The drop seen experimentally is consistent with the prediction of band structure calculations [38].

Whilst the synthesis [145] and the structural determination [150] has been reported

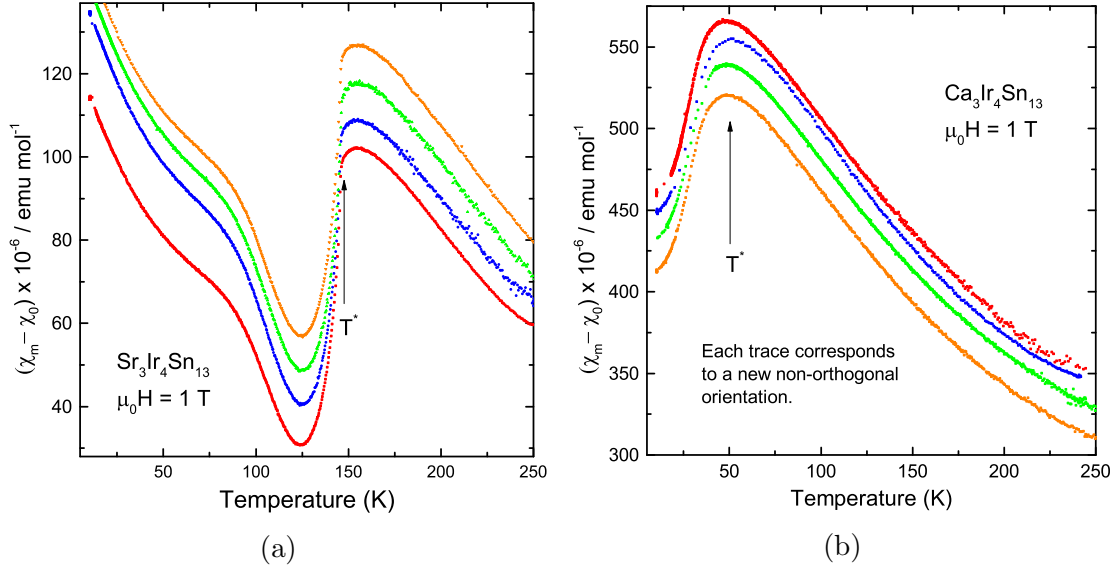


Figure 6.4: Magnetic susceptibility of $Sr_3Ir_4Sn_{13}$ and $Ca_3Ir_4Sn_{13}$ measured along a number of non-orthogonal orientations. There is a marked lack of magnetic anisotropy; the T^* transition is non-magnetic.

for $Ca_3Co_4Sn_{13}$ there has been very little reported otherwise. Upon immediate inspection, we might imagine that $Ca_3Co_4Sn_{13}$ should sit somewhere to the right of the phase diagram given in figure 6.2 owing to its lower transition temperature ($T_c = 6$ K), that it shares the undistorted high-temperature I -phase crystal structure, and that Co sits two above Ir in the periodic table.

Our aims for the study of the $A_3B_4Sn_{13}$ were as follows:

1. Using a miniature anvil SQUID cell, investigate the influence of pressure on the superconducting T_c in $Ca_3Ir_4Sn_{13}$, describing the “bubble” of superconductivity. Namely, showing T_c to go up, and then down as the hydrostatic pressure is increased.
2. Perform a similar anvil cell study on $Ca_3Co_4Sn_{13}$ to determine whether T_c increases or decreases with pressure. This will allow estimation of its likely position on the phase diagram given in 6.2.
3. Investigate the superconducting state of $Ca_3Ir_4Sn_{13}$ and $Sr_3Ir_4Sn_{13}$ through a series of DC magnetisation measurements. Determine the temperature

dependence of the critical fields $H_{c1}(T)$, $H_{c2}(T)$, such that the corresponding BCS parameters can be determined.

6.2 Pressure dependence of T_c

Firstly, we examine the pressure dependence of the superconducting transition in $Ca_3Ir_4Sn_{13}$ and $Ca_3Co_4Sn_{13}$.

6.2.1 $Ca_3Co_4Sn_{13}$

A miniature diamond anvil cell was set up by Dr Swee Goh of the Quantum Matter group, containing a sample of $Ca_3Co_4Sn_{13}$, along with a ruby chip for pressure determination. The samples were grown by Professor Yoshimura's group at Kyoto university.

The cell used for this study was a different one to that used for the $CeAgSb_2$ data in the previous chapter, although the experimental procedure was identical. The raw data at a number of pressures is shown in figure 6.5, where in each case the cell has been zero-field cooled, before a small positive field was applied at the lowest temperature. Data was then collected upon warming and then cooling.

The maximum pressure measured was 25.7 kbar. As the primary motive in this study was to determine whether T_c increased or decreased with pressure, it seemed unnecessarily risky to move to higher pressures once it was clear that T_c was coming down with P . Moreover, due to the overall form of the cell background (top left of figure 6.5, the superconducting drop in the magnetisation at T_c would begin to overlap with the temperature regime where the cell background rapidly increases in magnitude. It is likely that the quality of the data would reduce at higher pressures due to the "step" coinciding with the strongly temperature dependent background.

Figure 6.6 shows the background-subtracted traces taken at a series of pressures. As in the YFe_2Ge_2 measurements, a large anisotropy between the field-cooled and zero-field cooled runs is apparent (not shown), revealing the presence of pinning within the sample bulk. Upon warming, the superconducting transition appears as a step-like feature in $M(T)$ at T_c .

As can be seen in figure 6.6, the application of hydrostatic pressure in $Ca_3Co_4Sn_{13}$ *re-*

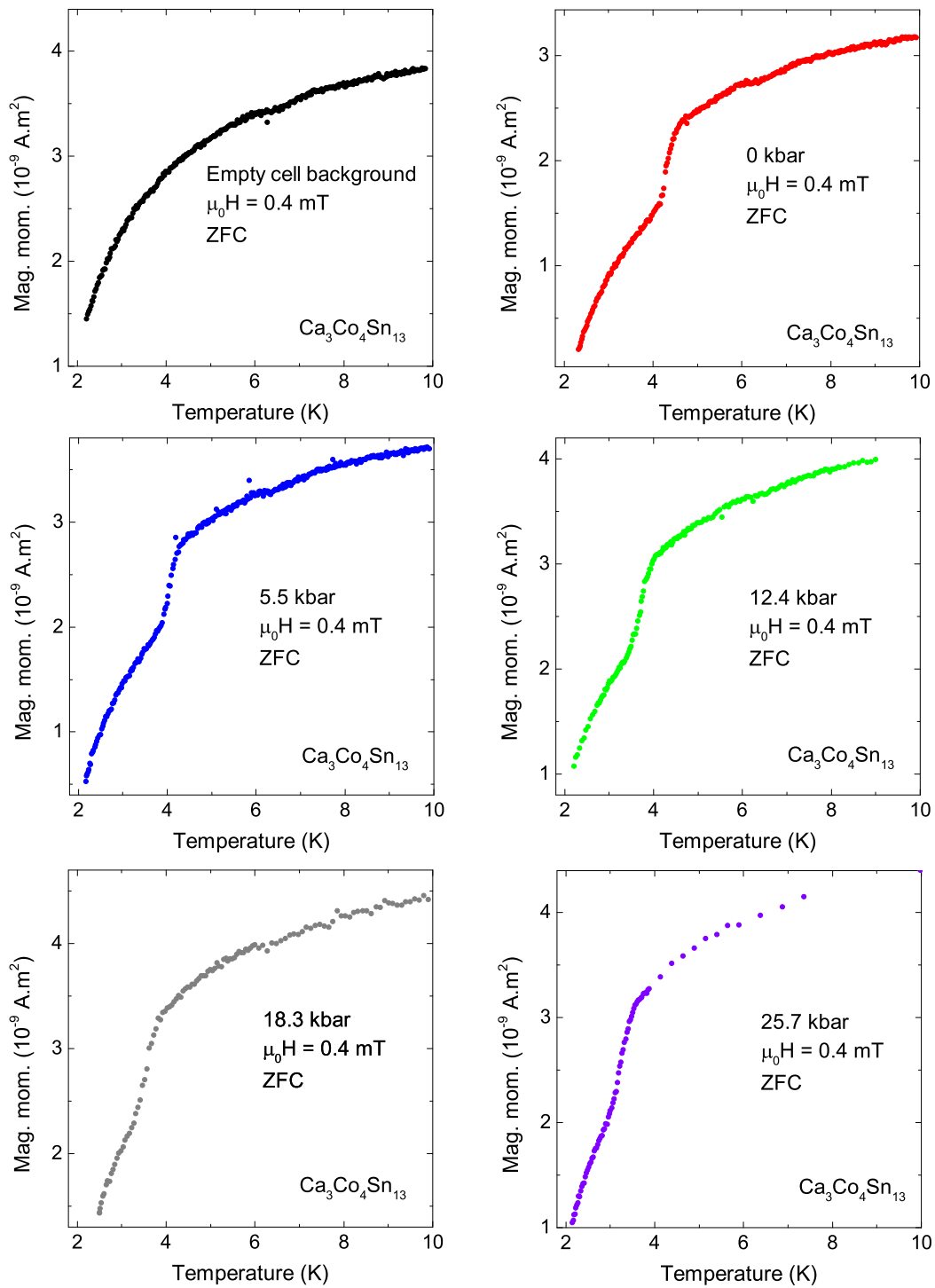


Figure 6.5: Raw data from the study of $\text{Ca}_3\text{Co}_4\text{Sn}_{13}$ in a miniature anvil squid cell. All traces shown have been zero-field-cooled, and then warmed in 0.4 mT of applied field. The top left figure shows the empty cell background run after the sample had been removed.

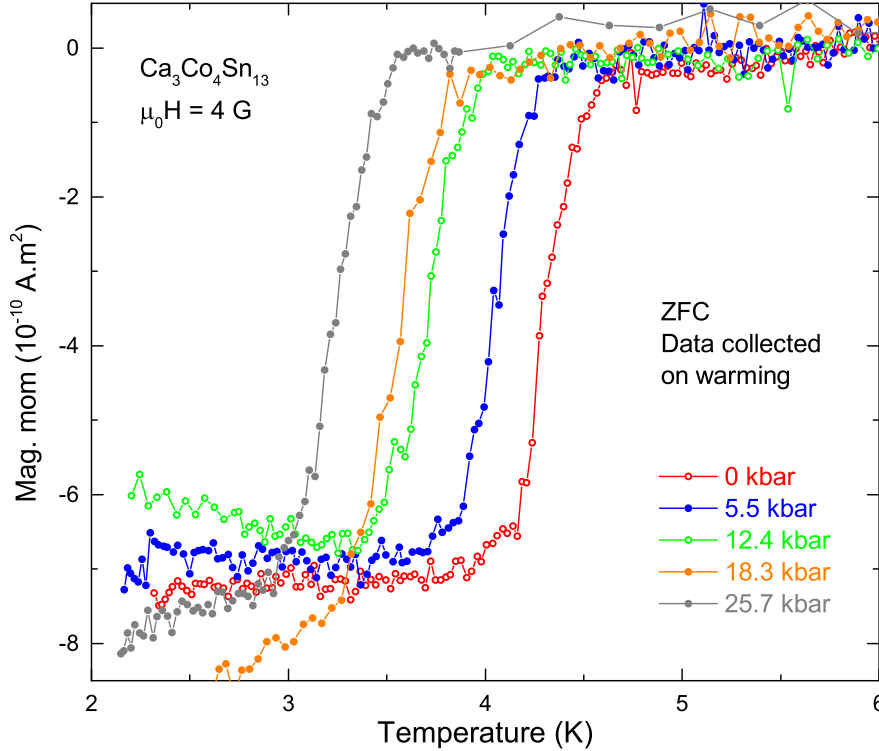


Figure 6.6: $M(T)$ data from $\text{Ca}_3\text{Co}_4\text{Sn}_{13}$ taken at various pressures in miniature anvil SQUID cell. Background has been subtracted. Glycerin used as pressure medium. Solid (open) symbols show points collected on pressuring (depressurising).

duces the transition temperature. This is consistent with our initial guess of its location on the phase diagram in fig. 6.2.

Figure 6.7 shows a PT phase diagram, with the pressure points taken from the traces in fig. 6.6. As shown in the inset, the transition temperature is determined from the mid-point of the “step”, where the error bars reflect the width of the transition ($\Delta T = T_{high} - T_{low}$).

To check for any hysteretic effects, pressure points were taken both upon increasing (the solid points on the phase diagram) *and* decreasing the pressure (the hollow points). Hysteresis is totally absent, with all points appearing to fall on a common straight line. Extrapolating this line to zero temperature puts an upper bound on the critical pressure required to drive the transition to zero temperature, giving

$T_c = 0$ K by around 110 kbar. In reality, the superconducting dome may well curve to $T = 0$ K more rapidly than this.

Superconductivity is suppressed with pressure in $Ca_3Co_4Sn_{13}$: $dT_c/dP < 0$. Provided that the underlying physics in this system is the same as that which is present in the $(Ca_x, Sr_{1-x})_3Ir_4Sn_{13}$ doping series, $Ca_3Co_4Sn_{13}$ at ambient pressure should be found out to the right-hand side of figure 6.2.

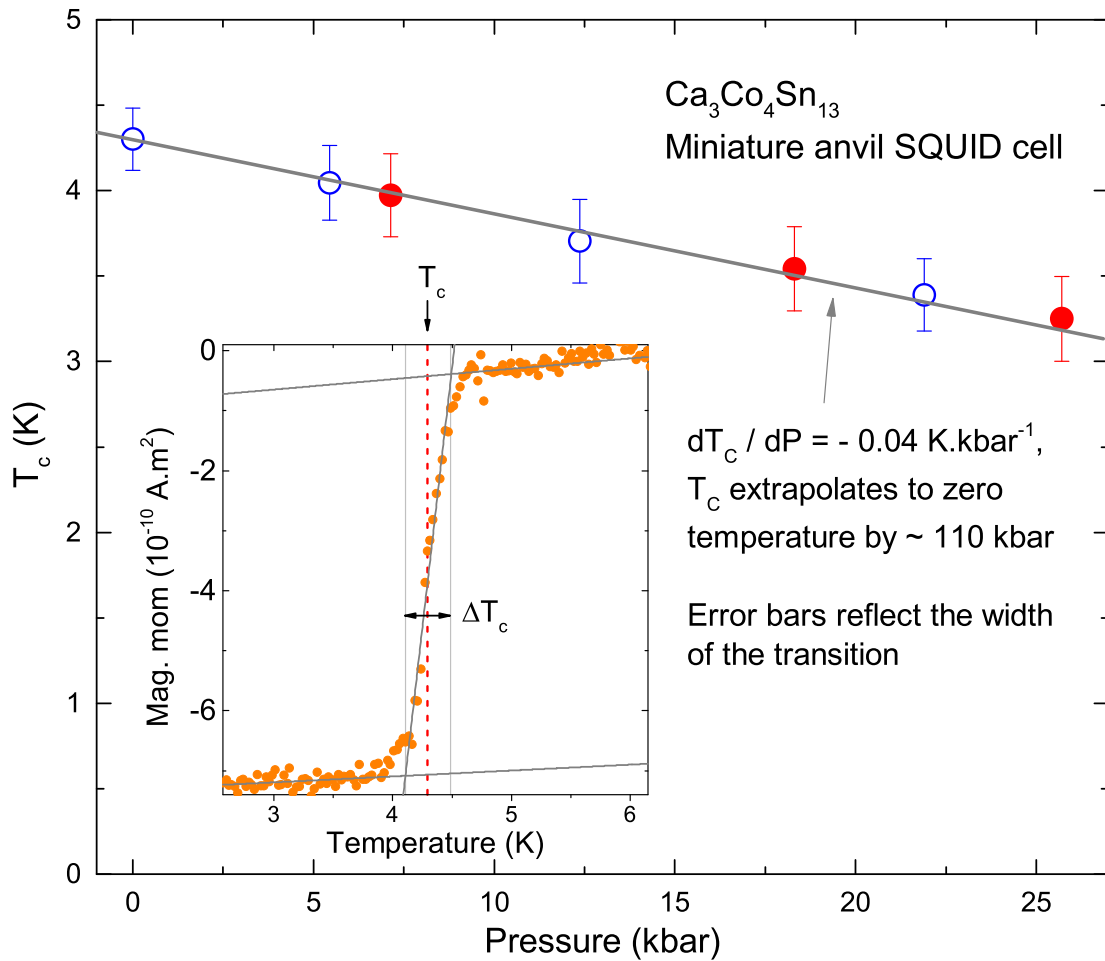


Figure 6.7: Phase diagram showing the pressure dependence of T_{sc} in $Ca_3Co_4Sn_{13}$, with the pressure determined by the ruby fluorescence technique. Solid (open) symbols show points collected on pressuring (depressurising). Error bars reflect the width of the transition appearing in $M(T)$.

6.2.2 $Ca_3Ir_4Sn_{13}$

Proceeding in exactly the same manner as with $Ca_3Co_4Sn_{13}$, a miniature anvil SQUID cell was set up with a sample of $Ca_3Ir_4Sn_{13}$, also containing a ruby chip for pressure determination, and glycerin as the pressure medium. Here, the aim was to examine the *domed* nature of the superconducting bubble, using magnetisation to determine $T_c(P)$.

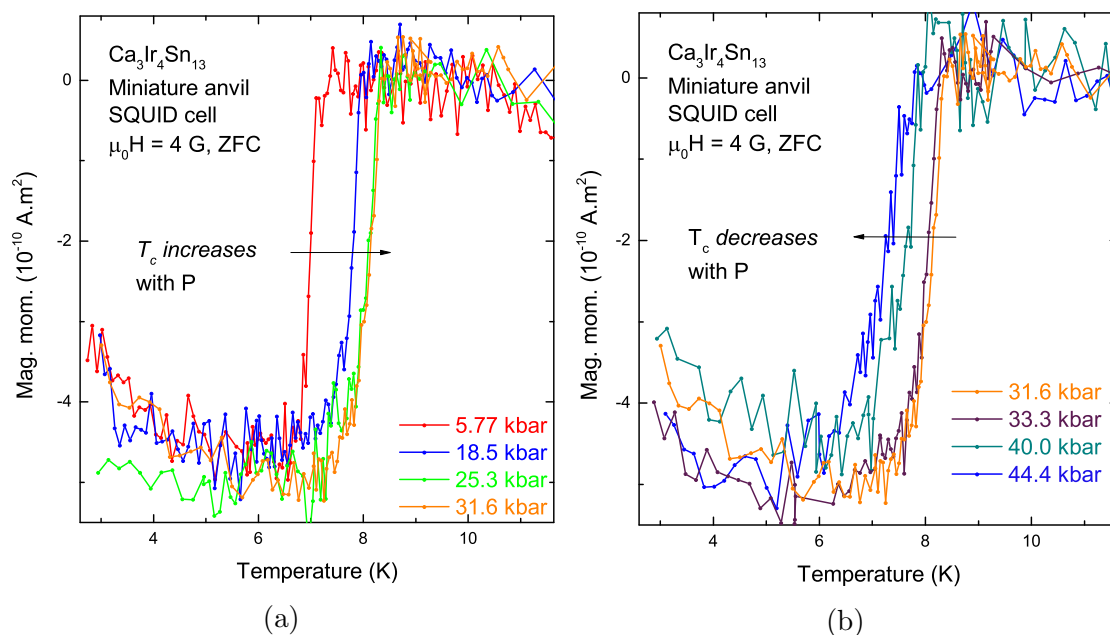


Figure 6.8: $M(T)$ data of $Ca_3Ir_4Sn_{13}$ at various pressures in a miniature anvil SQUID cell. The left figure shows the transition temperature *increasing* as the pressure is increased, whereas the right figure shows it *decreasing* with an increased P .

$M(T)$ curves at various pressure are shown in figure 6.9. As before, the cell was zero-field cooled, a small positive field was applied, and then the sample was warmed through the transition. Also, as in the previous section (and in the previous chapter) a notable anisotropy was found between the zero-field cooled and the field cooled data, in that the size of the step is much more pronounced during the ZFC run than the FC one. The traces shown in figure 6.9 contain a little more noise than those shown for the $Ca_3Co_4Sn_{13}$ runs, due to the fact that

the signal associated with the transition is slightly smaller, and that not as many scans were taken per point.

The data which is shown in figure 6.9 is the raw signal from the cell and sample. No background was subtracted from these runs, as the influence of the cell (a different cell to the $Ca_3Co_4Sn_{13}$ data) was not as significant in the temperature range being investigated in this study.

The left and right hand sides of figure 6.9 show the changing influence of pressure on T_c . Initially, the build-up of P results in an *increase* of the transition temperature, as shown in the left hand figure. This persists up to around 32 kbar, beyond which the further increase of P results in a *decrease* in T_c . Extracting

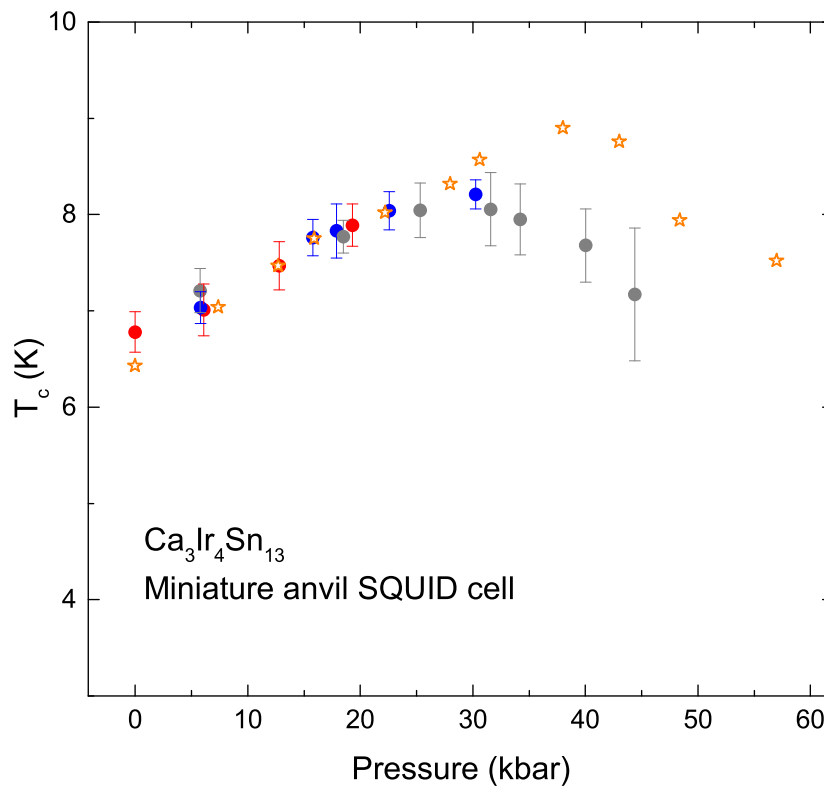


Figure 6.9: PT phase diagram of $Ca_3Ir_4Sn_{13}$, constructed from a series of miniature anvil SQUID cell runs. Different coloured dots represent different cell runs, whilst the stars are taken from [38]. The size of the error bars reflect the width of the transition as shown in the inset of 6.7.

the transition temperature from each of the $M(T)$ curves, we may construct the corresponding PT phase diagram, as shown in figure 6.9. Also included are the points corresponding to the phase boundary in [38], from AC-susceptibility and resistivity measurements.

The phase diagram contains points taken from a few different cell runs, shown as different coloured dots. It is clear from the shape of the boundary that the pressure ~ 32 kbar corresponds to the apex of the superconducting dome, beyond which increasing P suppresses T_c . There is mutual agreement between the different cell runs, and broad agreement with the phase boundary in the literature. Clearly, the shapes of our domes do not match exactly, as the reported dome does not peak until around 40 kbar, whilst for our data T_c is already well on its way down by this point. Unfortunately, it was not possible to extend the study to higher pressures as the pressure cell used was prone to gasket failure at $\approx 50 - 60$ kbar, owing to slight imperfections in its construction. This is reflected in the transitions becoming more broad as the pressure is increased, due to the reduction in hydrostaticity.

6.3 Upper critical field and the peak effect

Here we evaluate the upper critical field $H_{c2}(T)$ from isothermal field sweeps. At H_{c2} , the magnetic signal associated with the persistent supercurrents should go to zero. Figure 6.11 shows a series of field sweeps taken with the Ca and Sr systems which we can use to extract the critical field.

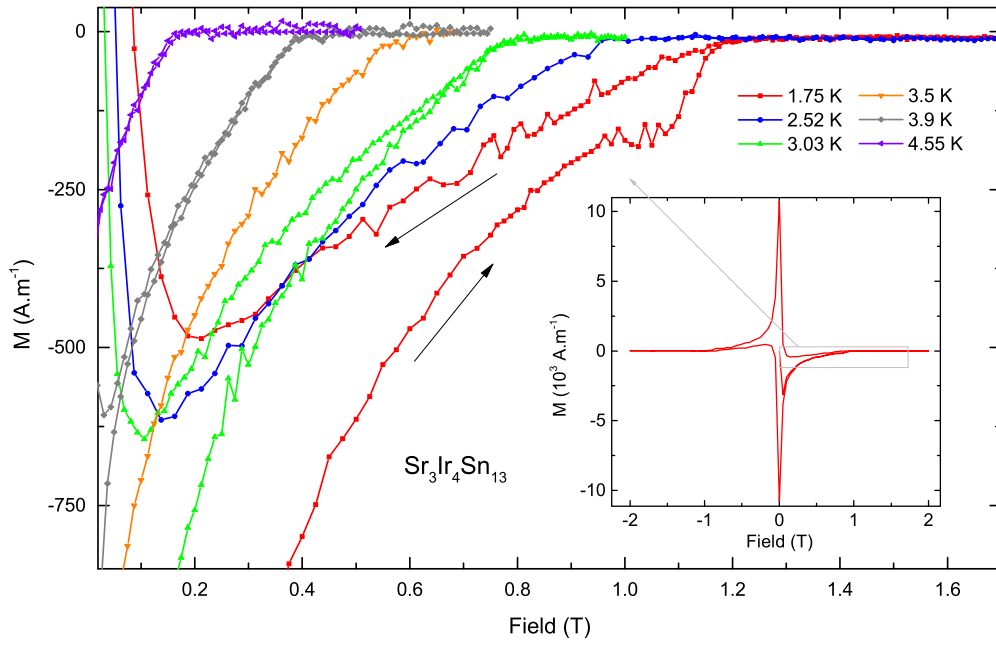
The inset of figure 6.10a shows a full field-swept loop, starting at $H = 0$. As in YFe_2Ge_2 , the presence of hysteresis demonstrates the existence of pinning centres within the sample. However, the loop shown in this data is not as wide as that shown in figure 5.13a - this loop looks *less* hysteretic, or *more reversible*. This corresponds to a difference in the level of pinning between the two systems. In an ideal type-II superconductor, with a total absence of pins, up and down field sweeps should be totally reversible. As the magnitude of the pinning forces increase, the field does more work against them and consequently the width of the loop increases - it becomes less and less reversible.

The critical field H_{c2} is extracted from $M(H)$ as shown in the inset of figure 6.10b. The corresponding phase boundary $H_{c2}(T)$ is given in figure 6.11, with the lines of fit given by the WHH theory of the upper critical field in the clean limit with the spin-orbit coupling parameter $\alpha = 0$. At zero-temperature, the upper critical field extrapolates to 7.4 T in the calcium-based system, and 1.45 T in the strontium one.

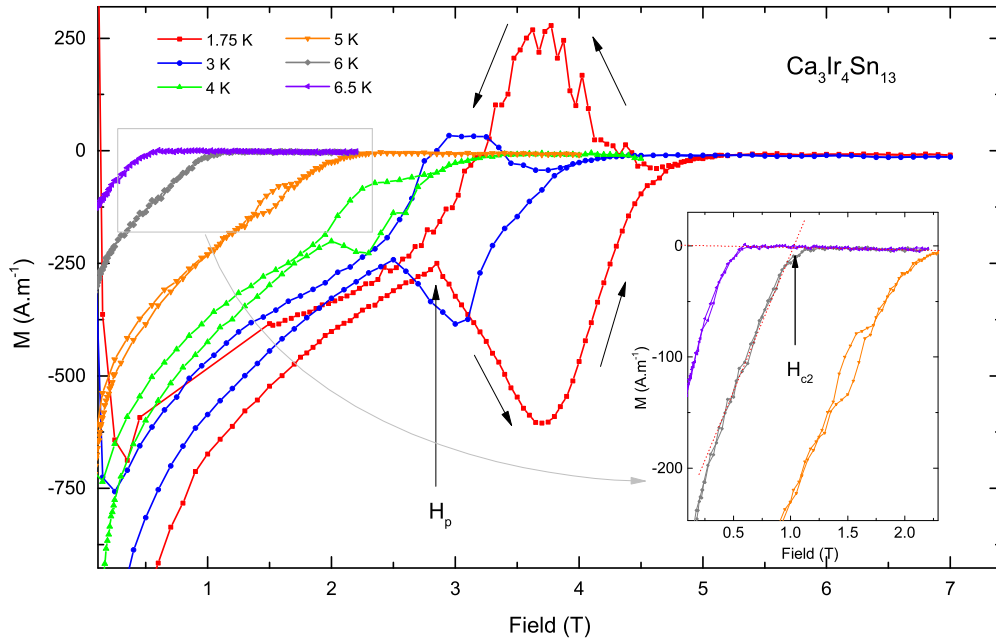
In both $Ca_3Ir_4Sn_{13}$ and $Sr_3Ir_4Sn_{13}$ we find that at a particular field H_p (shown on figure 6.10b), rather than monotonically approaching zero at H_{c2} , $M(H)$ dips unexpectedly to more negative values then increases, describing a sort of semi-circle. Upon ramping the field back down, this procedure is repeated in reverse, such that overall the trace contains something a little like a “bubble”, beginning at H_p .

Similar magnetic anomalies were found in the related stannide-superconductor $Ca_3Rh_4Sn_{13}$ [151, 152]³. There, the features were attributed to a flux-line lattice

³At the moment it is unclear what correspondence this system has to the phase diagram shown in figure 6.2. Given that and that Rh has less core states than Ir would suggest that



(a) Inset shows $M(H)$ for a complete field loop. Such a loop corresponds to *weak* pinning within the sample.



(b) Fishtail-type [151] feature highlighted at H_p associated with the onset of the peak effect. Inset shows the method used to determine H_{c2} .

Figure 6.10: $M(H)$ data for $Sr_3Ir_4Sn_{13}$ and $Ca_3Ir_4Sn_{13}$ to determine the upper critical field $H_{c2}(T)$. Arrows show the direction of the field sweep.

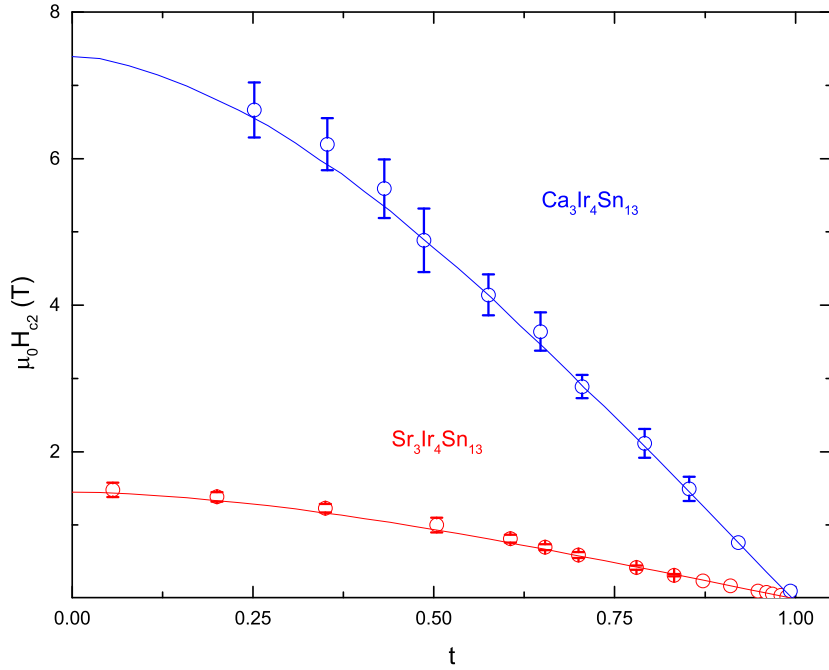


Figure 6.11: Magnetic phase diagram for $(Ca,Sr)_3Ir_4Sn_{13}$ showing the temperature dependence of the upper critical field $H_{c2}(T)$. The lines of fit correspond to the WHH theory of the upper critical field in the clean limit.

(FLL) phenomenon known as the *peak effect* [18, 20]. The name “peak effect” arises due to the sudden increase in the critical current density $J_c(H)$ which is found in the vicinity of H_p , the same field range as the “fishtail” which appears in the magnetisation.

Brian Pippard [153] was one of the first to provide a mechanism which could account for such an effect. He suggested that the features found in the vicinity of H_p corresponded to a “reorganisation” of the FLL, which may become energetically favourable at fields near H_{c2} .

The FLL is not totally rigid; for a particular lattice arrangement, each fluxoid is able to be held at a position (say, at a pinning centre) slightly away from its equilibrium position, at an energy cost associated with the *elasticity* of every flux-

it ought to correspond to some high-pressure analogue of the $(Ca,Sr)_3Ir_4Sn_{13}$ system. Looking at its critical temperature $T_c = 8.2$ K [151], and our phase diagram in fig. 6.14 shows that the rhodium system could be equivalent to $Ca_3Ir_4Sn_{13}$ under 30 kbar of hydrostatic pressure.

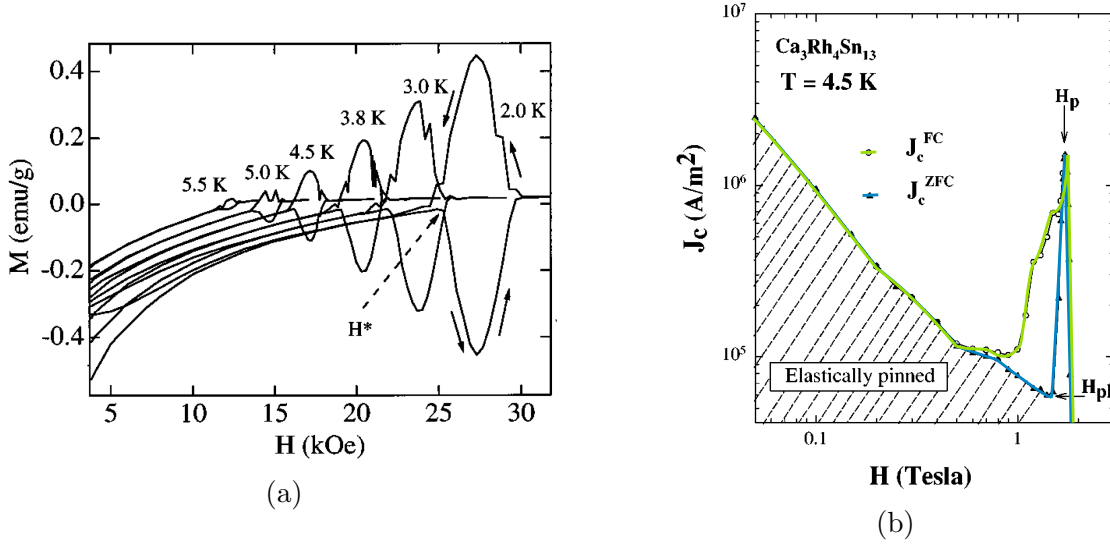


Figure 6.12: Similar “fishtail”-type features appearing in the magnetisation of $\text{Ca}_3\text{Rh}_4\text{Sn}_{13}$ [151], along with the “peak” in the critical current J_c [152].

line position. The energy cost due to the slight deformation of the lattice must be matched against the reduction in energy due to more and more flux-lines becoming pinned, which helps stabilise the lattice. The FLL has a certain *rigidity* which parameterises its ability to undergo these elastic distortions. Pippard showed that near H_{c2} , the shear modulus of the lattice is strongly reduced, such that the FLL *softens* and is able to rearrange itself to better match the location of the pinning centres. The periodicity of the newly reorganised lattice approaches the defect concentration of the bulk (see figure 6.13). Although the lattice in this state is now totally fluid it is able to support a higher supercurrent density, owing to the improved level of pinning. As a result, the bulk can maintain a larger supercurrent, which is seen experimentally as an increase in J_c and consequently the magnetisation.

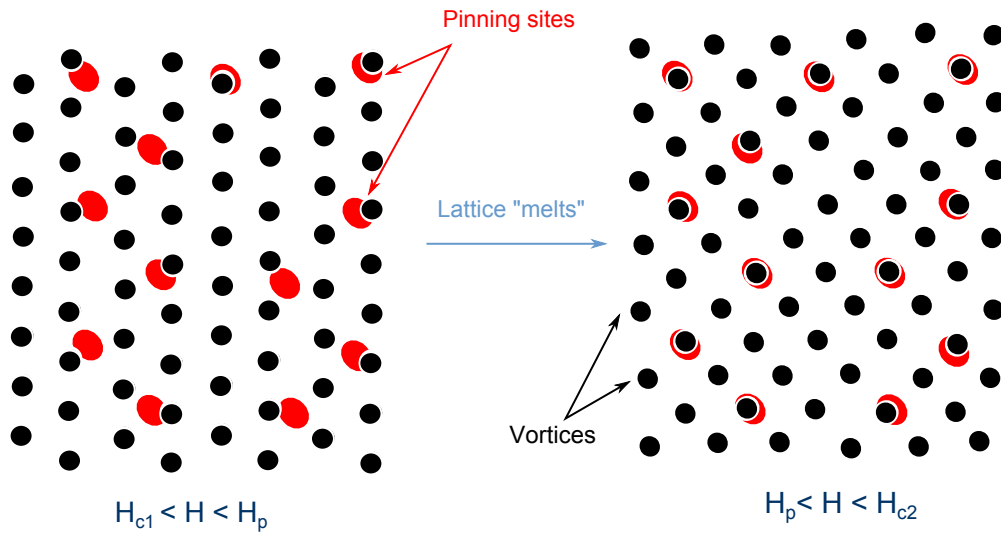


Figure 6.13: Schematic of the FLL reorganisation which takes place at H_p .

6.4 Discussion

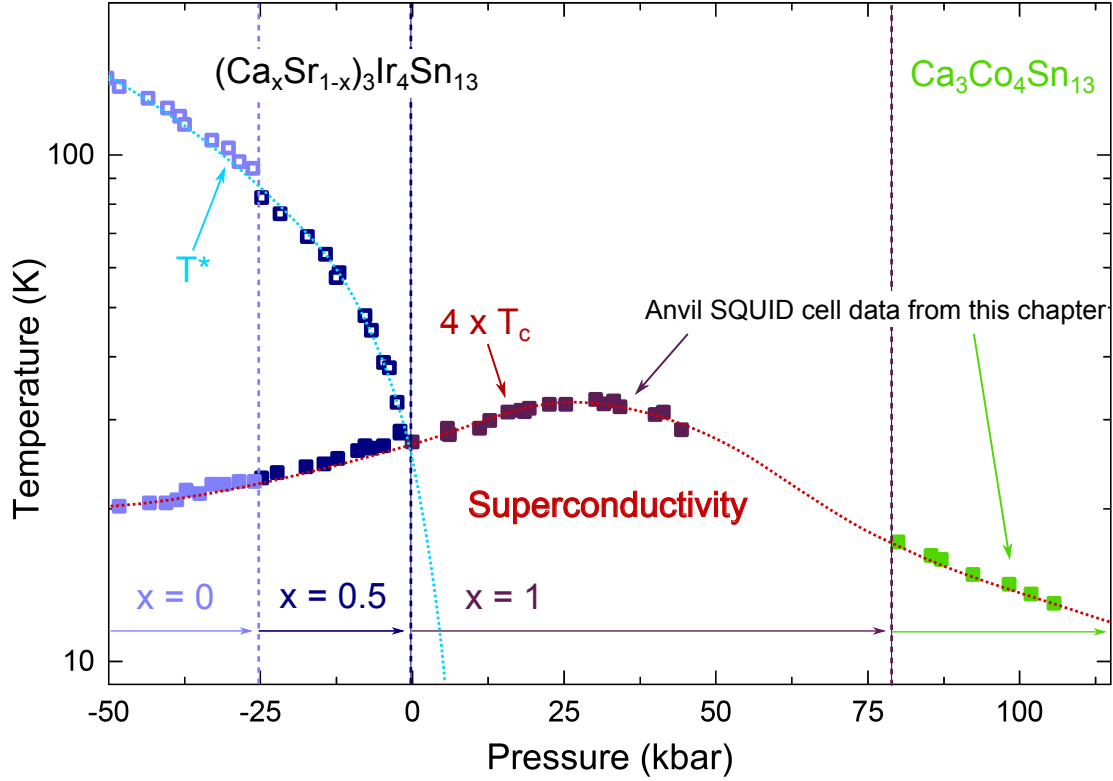


Figure 6.14: Composite phase diagram of the $A_3B_4Sn_{13}$ series, showing the $(Ca,Sr)_3Ir_4Sn_{13}$ series and data from $Ca_3Co_4Sn_{13}$. $x = 0$ and $x = 0.5$ data reproduced from [38].

Figure 6.14 shows all the points from the pressure studies of $Ca_3Ir_4Sn_{13}$ and $Ca_3Co_4Sn_{13}$ presented in this chapter, along with the $x = 0$ and $x = 0.5$ doping points of the $(Ca,Sr)_3Ir_4Sn_{13}$ series from [38], describing the total extent of the superconducting dome. Based on its transition temperature at ambient pressure, and the pressure points determined for $Ca_3Ir_4Sn_{13}$, we estimate that $Ca_3Co_4Sn_{13}$ corresponds to $Ca_3Ir_4Sn_{13}$ under about 80 kbar of pressure. The critical temperature does not become maximum at the point at which T^* appears to extrapolate to zero temperature, but at a pressure beyond it. This has been accounted for in the literature [38] as due to the transition temperature T_c having a complicated dependence on the frequency of the soft mode, whereby competition between different

mechanisms means that T_c may not necessarily peak where the mode frequency goes to zero.

Given the combinatorial advantage the system offers of being able to dope on both the A and the B site, *and* the application of physical pressure, it should be possible to fill out this phase diagram more completely. In particular, more study of materials which can be driven to the region around which $T^* \rightarrow 0$ K, will help relate the density-wave transition to the low-temperature superconducting state, and possibly identify fluctuations in the critical region.

For $Sr_3Ir_4Sn_{13}$, the magnitude of our upper critical field - 1.45 T - is somewhat less than the 3.45 T which was initially reported in the literature [147], whilst it is strongly in agreement with a recent as-yet unpublished μ SR/magnetisation study [154], which found $H_{c2} = 1.44$ T. For $Ca_3Ir_4Sn_{13}$, our estimate of the upper critical field 7.4 T is in accord with resistivity measurements [146] which produced a similar value.

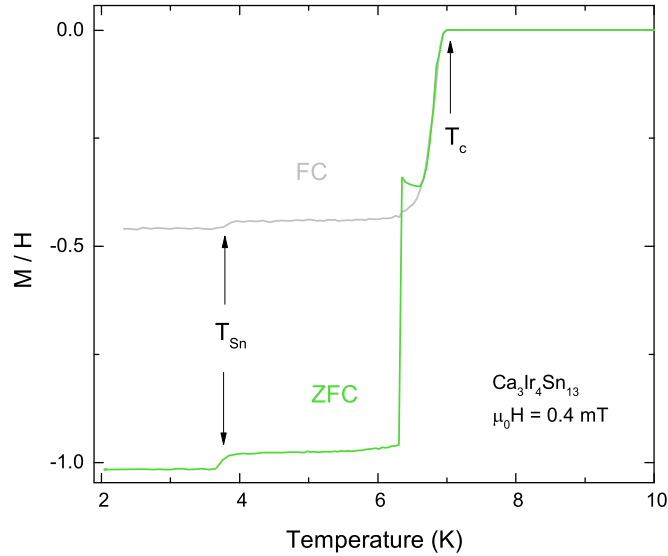


Figure 6.15: Temperature dependent magnetisation $M(T)$ for $Ca_3Ir_4Sn_{13}$ showing the bulk superconducting transition at $T_c = 6.96$ K, along with the impurity phase transition at $T_{Sn} = 3.72$ K, with ZFC and FC traces shown.

Unfortunately, attempts to measure the lower critical field failed here, due to the presence of tin inclusions leftover from the flux-growth. The presence of the Sn

impurities can be seen in the temperature dependent magnetisation, as shown in figure 6.15, whereby a small step in $M(T)$ at $T = 3.72$ K marks the point at which impurities become superconducting. Consequently, it was not possible to extract $H_{c1}(T)$ from the field-dependent $M(H)$ sweeps due to the interplay between the bulk and impurity superconducting phases. This had no effect on the extraction of $H_{c2}(T)$, as the critical field of tin is significantly less than the upper critical fields of $Ca_3Ir_4Sn_{13}$ or $Sr_3Ir_4Sn_{13}$.

Appendix A

Determination of H_{c1}

In the Meissner state the magnetic induction B is zero within the sample, resulting in $M = -H$. At H_{c1} this condition is no longer satisfied and flux begins to enter into the bulk. Extracting H_{c1} from experimental data is non-trivial, and so we detail here four different methods to extract H_{c1} .

A.1 $dM/dH \neq -1$

In the Meissner phase $M = -H$; it follows that the magnetic susceptibility

$$\chi = \frac{dM}{dH} = -1. \quad (\text{A.1})$$

From an isotherm $M(H)$, at temperature $T < T_c$, it is possible to determine H_{c1} from the derivative dM/dH as the point at which $dM/dH \neq -1$. Figure A.1a shows the dM/dH for $\text{Ca}_3\text{Ir}_4\text{Sn}_{13}$ at $T = 1.8$ K. It is possible to identify two regions on the curve – one at low fields where dM/dH fluctuates around -1, and another at slightly elevated fields, where dM/dH begins to increase towards zero. Fitting straight lines through each region and finding their intersection gives the boundary between the two, yielding $H_{c1} = 5.8$ mT.

A.2 $\Delta M = H + M \neq 0$

Rewriting the Meissner condition $M = -H$ as

$$M + H = 0 \quad (\text{A.2})$$

and also defining $\Delta M = M + H$, we can identify the critical field H_{c1} as the field at which

$$\Delta M \neq 0. \quad (\text{A.3})$$

This taken as the point at which $\Delta M(H)$ exceeds zero by some fixed amount. Figure A.1b shows $\Delta M(H)$, where criterion $\Delta M = 200 \text{A.m}^{-1}$ is used to extract H_{c1} - found to be 8.5 mT.

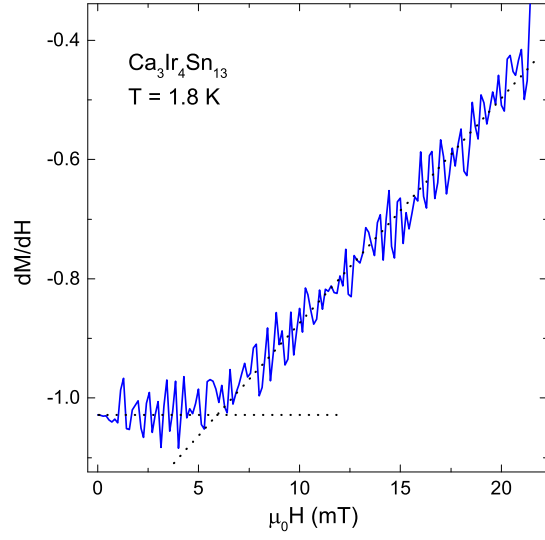
A.3 $\sqrt{\Delta M}$ I.

The quantity ΔM reflects the amount of flux admitted to the bulk after entering the mixed regime. It is expected to grow quadratically with the field for $H > H_{c1}$ [134, 155]. Plotting $(\Delta M)^{0.5}$ against H should yield straight lines growing out of the lower critical field H_{c1} , as shown in figure A.1b, giving $H_{c1} = 6.9$ mT at $T = 1.8$ K.

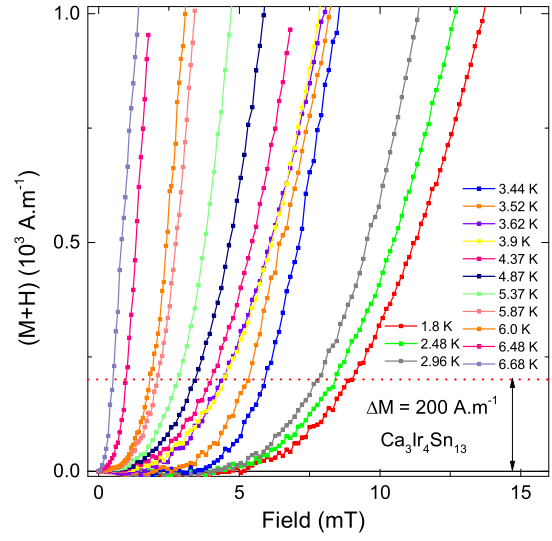
A.4 $\sqrt{\Delta M}$ II.

The flux entering the sample above H_{c1} becomes trapped due to the presence pinning forces. We can measure the onset of the trapped flux by zero-field cooling the sample to a temperature T and applying a small positive field H , before setting the field back to zero and then making a measuring the moment on the sample. If the applied field H is less than the lower critical field H_{c1} the sample will not have acquired a moment. As we have remained within the reversible Meissner regime found along the virgin curve, the shielding supercurrents simply die once the field is turned off. However, if the applied field H was *greater* than H_{c1} , some amount of

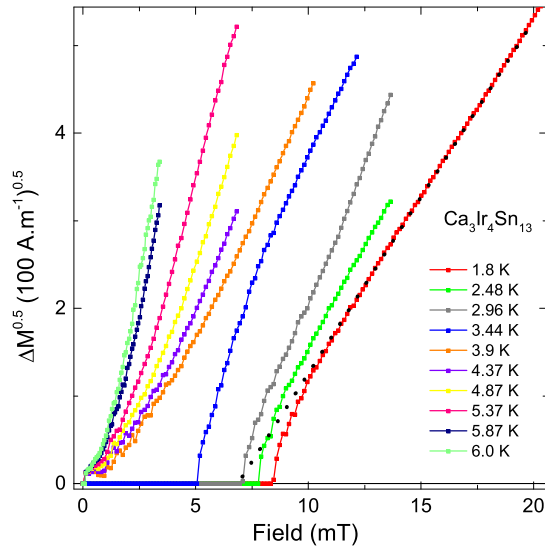
flux will have entered the bulk and, due to the pinning forces, will remain trapped even after the field has been reduced to zero. In this case, a measurement of the moment will show that the sample has acquired a finite trapped magnetisation M_t . Repeating this at various H , the trapped moment grows quadratically with the field above H_{c1} [22], so – like in method 3 – extrapolating a straight line through $M_t^{0.5}$ yields an estimate of the lower critical field H_{c1} . This can be repeated at various temperatures to obtain the full $H_{c1}(T)$ profile. See figure A.1d.



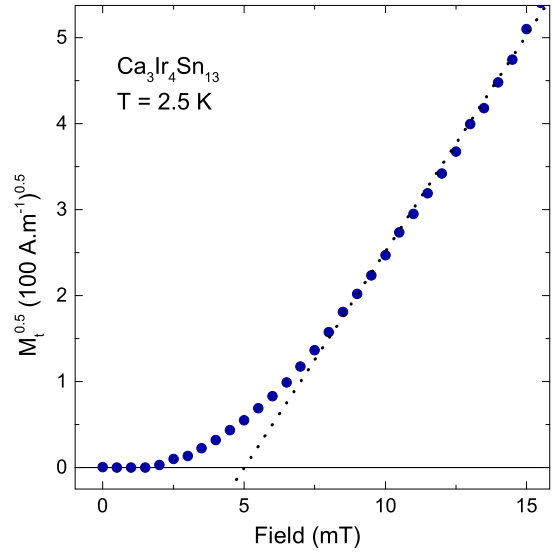
(a) Method 1.



(b) Method 2.



(c) Method 3.



(d) Method 4.

Figure A.1: Means of extracting H_{c1} from isothermal field sweeps.

Appendix B

Pinning and irreversibility

A perfect, defect-free type-II superconductor has a magnetisation curve $M(H)$ like one of those given in figure 2.5. In the mixed state, the quantised fluxoids are able to move freely throughout the sample and the flux density profile within the bulk is totally homogeneous – their mutual repulsive interactions making them spread evenly across the sample. The equilibrium relation between B and H is described by a constitutive equation like the one shown in the inset of figure 2.5. $M(H)$ in the pinning-free case is totally reversible, as the vortices enter and leave the sample in a totally reversible manner.

The origin of the irreversibility seen in real type-II superconductors is due to the presence of pinning centres – defects, impurities and so on. The flux profile cannot “relax” homogeneously throughout the interior, as the impedance caused by imperfections results in a *build-up* of flux at the sample edges. By Faraday’s law

$$\vec{\nabla} \times \vec{B} = \vec{J}, \quad (\text{B.1})$$

the spatial variation of the magnetic induction in the sample results in the presence of a finite current density \vec{J} . A finite supercurrent within the bulk imparts a Lorentz force

$$f_l = \vec{J} \times \vec{B} \quad (\text{B.2})$$

on the flux-line lattice (FLL), which tries to set it in motion, resulting in insta-

bility. These Lorentz forces act in opposition to the pinning forces, which try to hold the lattice still. Consequently, when pinning centres are present within a superconductor, the FLL is robust against the destabilising force, and a finite \vec{J} can be supported within the bulk. Counterintuitively, the presence of defects and impurities within a superconducting material actually proves to be useful if we wish to pass a current through it! This can also be seen from equation B.1, as for a totally homogeneous magnetic induction \vec{B} – which we would find in an ideal, perfect superconductor – the curl $\vec{\nabla} \times \vec{B}$ goes to zero, along with the supercurrent density $\vec{J} = 0$.

A number of phenomenological models, known as “critical state models”, can describe the shapes of magnetic measurements by considering the competition between the pinning and Lorentz forces. The central idea is that the pinning forces which hold the FLL in place *exactly match* the Lorentz forces trying to destabilise them. Consequently, the current density J_c is always at its maximum possible value, and the FLL is always *just* on the point of slipping. If the current density was slightly higher, the Lorentz forces would win, and the FLL would collapse. A key point is that whilst the strength of the pinning forces are *independent* of the applied field – an increased field doesn’t make a grain boundary pin flux more strongly – the strength of the Lorentz forces scale up with an increased field (see equation B.2). In real systems, at sufficiently high fields, the Lorentz forces will always win.

The starting point of the critical state model is to assume the form of the critical current density $J_c(H, T)$. With $J_c(H, T)$, all other relevant quantities may be constructed – the magnetisation, say, is given by

$$\vec{M} = \frac{1}{2V} \int (\vec{r} \times \vec{J}) dV, \quad (\text{B.3})$$

such that $M(H)$ is then determined solely by the field dependence of the current density $J_c(H)$ along with boundary conditions due to the magnetic history.

The original and most simple of these is the *Bean model*. Whilst the Bean model is not able to account for the reduction seen in the magnetisation as H approaches H_{c2} , it is useful as a starting point to describe the hysteresis. In the Bean model,

the pinning forces are assumed to scale with field exactly with the Lorentz forces. As a result, the current density \vec{J} can only take the values $\pm J$ or zero, which means – due to equation B.1 – that the flux profile which leaks into (or out of) the bulk must have a constant gradient [18].

Figure B.1 shows the Bean model applied to a superconducting slab (shown in grey) of length a in the x direction, and infinite along y , the field applied parallel to the slab. The upper two plots show how, above the lower critical field H_{c1} , flux lines leak into the sample. The solid blue line in the bottom figure shows the hysteresis loop which can be determined from equation B.1 and equation B.3, in the Bean approximation. Whilst there is evidently hysteresis, the loop never closes, even at arbitrarily high fields. This is due to the finite and constant gradients in $B(x)$ which, in this approximation, never reduce.

The dotted line shows an isotherm which would be obtained by assuming a different field dependence of the current – $J_c \sim 1/(H + H_0)$. In this model, J_c tends to zero as H goes to infinity, such that the gradients in $B(x)$ will die out in a sufficiently high field, resulting in the magnetisation tending to zero. There are a number of more or less complicated models – the Kim model or the exponential model, for instance [156–158] – which assume more or less complicated functional forms for $J_c(H)$, and are able to account for more complicated phenomenology.

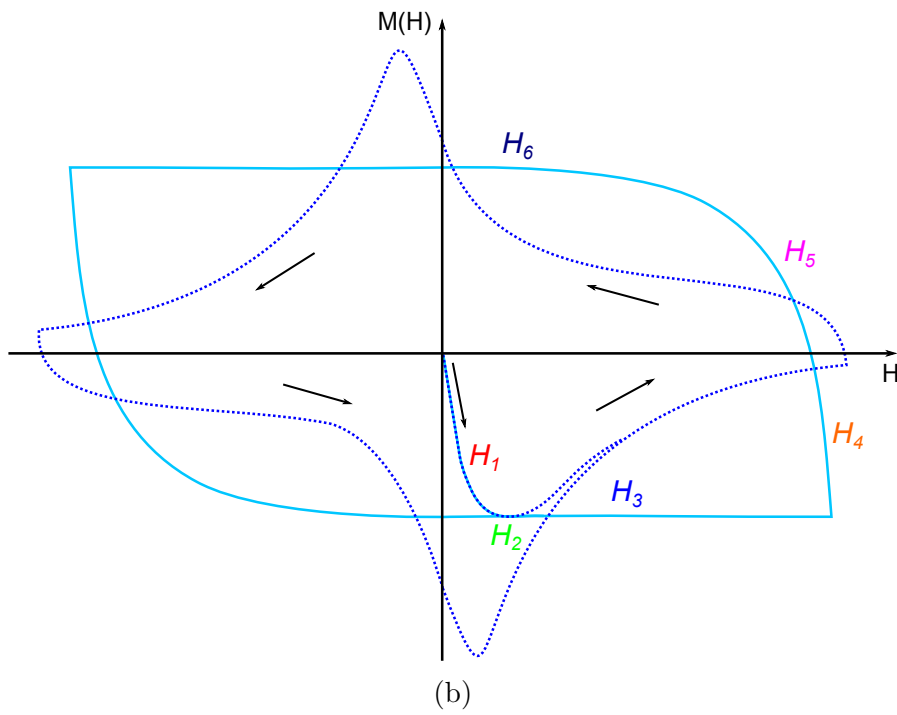
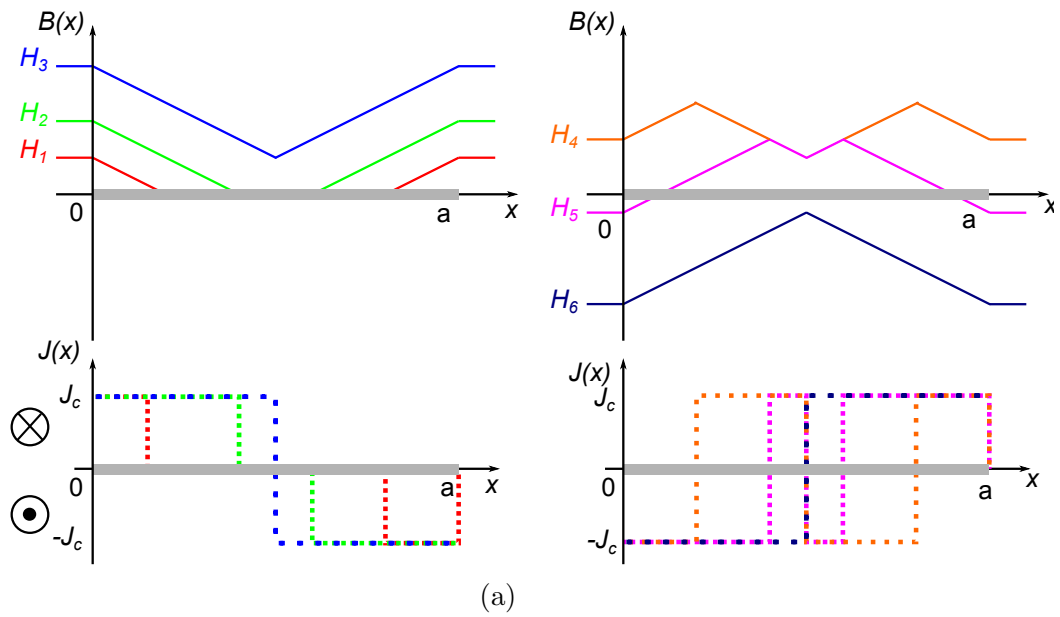


Figure B.1: Irreversibility in a type-II superconductor

Bibliography

- [1] *S700X SQUID Magnetometer User Manual v0.96 Cryogenic Ltd.*
- [2] Yang Zou. *Quantum Critical Phenomena in Intermetallic Compounds*. PhD thesis, University of Cambridge, 2014.
- [3] P. W. Anderson. Plasmons, Gauge Invariance, and Mass. *Phys. Rev.*, 130:439–442, Apr 1963.
- [4] P W Higgs. Broken Symmetries and the Masses of Gauge Bosons. *Phys. Rev. Lett.*, 13:508–509, Oct 1964.
- [5] L Landau. On the theory of phase transitions. *Zh. Eksp. Teor. Fiz.*, 7:19–32, 1937.
- [6] J Nagamatsu, N Nakagawa, T Muranaka, Y Zenitani, and J Akimitsu. Superconductivity at 39 K in magnesium diboride. *Nature*, 410:63–64, 2001.
- [7] J.G. Bednorz and K.A. Muller. Possible highT_c superconductivity in the Ba-La-Cu-O system. *Zeitschrift fr Physik B Condensed Matter*, 64(2):189–193, 1986.
- [8] M.R. Norman. Cuprates – An Overview. *Journal of Superconductivity and Novel Magnetism*, 25(7):2131–2134, 2012.
- [9] G. R. Stewart. Superconductivity in iron compounds. *Rev. Mod. Phys.*, 83:1589–1652, Dec 2011.
- [10] R P Feynman. “There’s plenty of room at the bottom”. http://www.pa.msu.edu/~yang/RFeynman_plentySpace.pdf.
- [11] T. Chattopadhyay, H.G.v. Schnering, and H.A. Graf. First order antiferromagnetic phase transition in MnS₂. *Solid State Communications*, 50(9):865 – 867, 1984.
- [12] K Kramer, G Meyer, P Fischer, A W Hewat, and H U Gdel. Neutron diffraction investigation of magnetic phase transitions to long-range antifer-

- romagnetic ordering in the free-electron praseodymium halides Pr_2X_5 ($\text{X} = \text{Br}, \text{I}$). *Journal of Solid State Chemistry*, 95(1):1 – 13, 1991.
- [13] B. D Simons. *Phase Transitions and Collective Phenomena*. Part III lecture notes, Cavendish Laboratory, 2014.
- [14] Thomas Vojta. *Physics 413 - Statistical Mechanics*. http://web.mst.edu/~vojta/class_413/class_413.html, 2014.
- [15] Leon N. Cooper. Bound Electron Pairs in a Degenerate Fermi Gas. *Phys. Rev.*, 104:1189–1190, Nov 1956.
- [16] E Maxwell. Isotope Effect in the Superconductivity of Mercury. *Phys. Rev.*, 78:477–477, May 1950.
- [17] J. Bardeen, L. N. Cooper, and J. R. Schrieffer. Theory of Superconductivity. *Phys. Rev.*, 108:1175–1204, Dec 1957.
- [18] J R Waldram. *Superconductivity of Metals and Cuprates*. Institute of Physics Publishing, 1996.
- [19] A.A. Abrikosov. The magnetic properties of superconducting alloys. *Journal of Physics and Chemistry of Solids*, 2(3):199 – 208, 1957.
- [20] M Tinkham. *Introduction to Superconductivity*. McGraw-Hill, 1996.
- [21] A. Carrington and F. Manzano. Magnetic penetration depth of MgB_2 . *Physica C: Superconductivity*, 385(1C2):205 – 214, 2003.
- [22] M. Abdel Hafiez, J. Ge, A. N. Vasiliev, D. A. Chareev, J. Van de Vondel, V. V. Moshchalkov, and A. V. Silhanek. Temperature dependence of lower critical field H_{c1} shows nodeless superconductivity in FeSe. *Phys. Rev. B*, 88:174512, Nov 2013.
- [23] N. R. Werthamer, E. Helfand, and P. C. Hohenberg. Temperature and Purity Dependence of the Superconducting Critical Field, H_{c2} . III: Electron Spin and Spin-Orbit Effects. *Phys. Rev.*, 147:295–302, Jul 1966.
- [24] S. Skalski, O. Betbeder Matibet, and P. R. Weiss. Properties of Superconducting Alloys Containing Paramagnetic Impurities. *Phys. Rev.*, 136:A1500–A1518, Dec 1964.
- [25] A A Abrikosov and L P Gor’kov. *Sov. Phys. - JETP*, 12:1243, 1960.
- [26] A Kopp and S Chakravarty. Criticality in correlated quantum matter. *Nature Physics*, 1:53–56, 2005.

- [27] Walter J Wild. Eulers three body problem. *American Journal of Physics*, 48:297, 1980.
- [28] Richard D Mattuck. *A Guide to Feynman Diagrams in the Many-Body Problem*. Dover, 1992.
- [29] K. Andres, J. E. Graebner, and H. R. Ott. $4f$ -Virtual-Bound-State Formation in CeAl_3 at Low Temperatures. *Phys. Rev. Lett.*, 35:1779–1782, Dec 1975.
- [30] M. Brando, W. J. Duncan, D. Moroni Klementowicz, C. Albrecht, D. Grüner, R. Ballou, and F. M. Grosche. Logarithmic Fermi-Liquid Breakdown in NbFe_2 . *Phys. Rev. Lett.*, 101:026401, Jul 2008.
- [31] J. Custers, P. Gegenwart, H. Wilhelm, K. Neumaier, Y. Tokiwa, O. Trovarelli, C. Geibel, F. Steglich, C. Ppin, and P. Coleman. The break-up of heavy electrons at a quantum critical point. *Nature*, 424:524–527, 2003.
- [32] F. M. Grosche. *Quantum Condensed Matter Physics*. Part II lecture notes, Cavendish Laboratory, 2014.
- [33] I.R. Walker, F.M. Grosche, D.M. Freye, and G.G. Lonzarich. The normal and superconducting states of CeIn_3 near the border of antiferromagnetic order. *Physica C*, 282C287(0):303 – 306, 1997. Materials and Mechanisms of Superconductivity High Temperature Superconductors V.
- [34] C Varma. Mind the Pseudogap. *Nature*, 468:184–185, 2010.
- [35] S. S. Saxena, P. Agarwal, K. Ahilan, F. M. Grosche, R. K. W. Haselwimmer, M. J. Steiner, E. Pugh, S. R. Julian I. R. Walke and, P. Monthoux, G. G. Lonzarich, A. Huxley, I. Sheikin, D. Braithwaite, and J. Flouquet. Superconductivity on the border of itinerant-electron ferromagnetism in UGe_2 . *Nature*, 406:587–592, 2000.
- [36] R M Fernandes, A V Chubukov, and J Schmalian. What drives nematic order in iron-based superconductors? *Nature Physics*, 10:97–104, 2014.
- [37] P L Alireza, F Nakamura, S K Goh, Y Maeno, S Nakatsuji, Y T C Ko, M Sutherland, S Julian, and G G Lonzarich. Evidence of superconductivity on the border of quasi-2D ferromagnetism in Ca_2RuO_4 at high pressure. *Journal of Physics: Condensed Matter*, 22(5):052202, 2010.
- [38] L E. Klintberg, S K Goh, P L A, P J Saines, D A Tompsett, P W Logg, J Yang, B Chen, K Yoshimura, and F. M Grosche. Pressure- and Composition-

- Induced Structural Quantum Phase Transition in the Cubic Superconductor $\text{Ca}_3\text{Ir}_4\text{Sn}_1\text{3}$. *Phys. Rev. Lett.*, 109:237008, Dec 2012.
- [39] F. Lévy, I. Sheikin, B. Grenier, and A. D. Huxley. Magnetic Field-Induced Superconductivity in the Ferromagnet URhGe. *Science*, 309(5739):1343–1346, 2005.
- [40] H Luetkens, H-H Klauss, M Kraken, F J Litterst, T Dellmann, R Klingeler, C Hess, R Khasanov, A Amato, C Baines, M Kosmala, O J Schumann, M Braden, J Hamann Borrero, N Leps, A Kondrat, G Behr, J Werner, and B Bchner. The electronic phase diagram of the $\text{LaO}_{1-x}\text{F}_x\text{FeAs}$ superconductor. *Nature Materials*, 8:305 – 309, 2009.
- [41] Y Matsumoto, S Nakatsuji, K Kuga, Y Karaki, N Horie, Y Shimura, T Sakakibara, A H Nevidomskyy, and Piers Coleman. Quantum Criticality Without Tuning in the Mixed Valence Compound $\beta\text{-YbAlB}_4$. *Science*, 331(6015):316–319, 2011.
- [42] D. Pines P. Monthoux and and G. G. Lonzarich. Superconductivity without phonons. *Nature*, 454:1177–1183, 2007.
- [43] N. D. Mathur, F. M. Grosche, S. R. Julian, I. R. Walker, D. M. Freye, R. K. W. Haselwimmer, and G. G. Lonzarich. Magnetically mediated superconductivity in heavy fermion compounds. *Nature*, 394:39–43, 1998.
- [44] A. Schilling, M. Cantoni, J. D. Guo, and H. R. Ott. Superconductivity above 130 K in the Hg-Ba-Ca-Cu-O system. *Nature*, 363:56–58, 1993.
- [45] *MPMS Application Note 1014-213 - “Subtracting the sample holder background from dilute sample”*.
- [46] U Ausserlechner, P Kasperkovitz, and W Steiner. A theoretical discussion of vector pick-up systems for SQUID magnetometers. *Measurement Science and Technology*, 9(6):989, 1998.
- [47] M. A. Garcia, E. Fernandez Pinel, J. de la Venta, A. Quesada, V. Bouzas, J. F. Fernndez, J. J. Romero, M. S. Martn Gonzalez, and J. L. Costa Kramer. Sources of experimental errors in the observation of nanoscale magnetism. *Journal of Applied Physics*, 105(1), 2009.
- [48] D. D. Osheroff, R. C. Richardson, and D. M. Lee. Evidence for a New Phase of Solid ^3He . *Phys. Rev. Lett.*, 28:885–888, Apr 1972.
- [49] *DMS User Manual (Dryogenic Ltd.)*.

- [50] P J W Moll, R Puzniak, F Balakirev, K Rogacki, J Karpinski, N D Zhigadlo, and B Batlogg. High magnetic-field scales and critical currents in SmFeAs(O, F) crystals. *Nature Materials*, 9:628–633, 2010.
- [51] M Nikolo. Superconductivity: A guide to alternating current susceptibility measurements and alternating current susceptometer design. *American Journal of Physics*, 63(1):57–65, 1995.
- [52] D. J. Dunstan. Theory of the gasket in diamond anvil high-pressure cells. *Review of Scientific Instruments*, 60(12):3789–3795, 1989.
- [53] D J Dunstan and I L Spain. Technology of diamond anvil high-pressure cells: I. Principles, design and construction. *Journal of Physics E: Scientific Instruments*, 22(11):913, 1989.
- [54] I L Spain and D J Dunstan. The technology of diamond anvil high pressure cells: II. Operation and use. *Journal of Physics E: Scientific Instruments*, 22(11):923, 1989.
- [55] P. Alireza and G. G Lonzarich. Miniature anvil cell for high-pressure measurements in a commercial superconducting quantum interference device magnetometer. *Rev. Sci. Instr.*, 80(2):023906, feb 2009.
- [56] P L Alireza and S R. Julian. Susceptibility measurements at high pressures using a microcoil system in an anvil cell. *Review of Scientific Instruments*, 74(11):4728–4731, 2003.
- [57] T Meissner, S K Goh, J Haase, G V M Williams, and P B Littlewood. High-pressure spin shifts in the pseudogap regime of superconducting YBa₂Cu₄O₈ as revealed by O¹⁷ NMR. *Phys. Rev. B*, 83:220517, Jun 2011.
- [58] P L Alireza, Y T C Ko, J Gillett, C M Petrone, J M Cole, G G Lonzarich, and S E Sebastian. Superconductivity up to 29 K in SrFe₂As₂ and BaFe₂As₂ at high pressures. *Journal of Physics: Condensed Matter*, 21(1):012208, 2009.
- [59] P Logg, Z Feng, T Ebihara, Y Zou, S Friedemann, P Alireza, S Goh, and F. Malte Grosche. Pressure and field tuning in the Kondo lattice ferromagnet CeAgSb₂. *Physica Status Solidi (b)*, 250(3):515–518, 2013.
- [60] J Xu, H-K Mao, R J Hemley, and E Hines. The moissanite anvil cell: a new tool for high-pressure research. *Journal of Physics: Condensed Matter*, 14(44):11543, 2002.
- [61] N Tateiwa and Y Haga. Appropriate pressure-transmitting media for cryogenic experiment in the diamond anvil cell up to 10 GPa. *Journal of Physics: Conference Series*, 215(1):012178, 2010.

- [62] You Shu Jie, Chen Liang Chen, and Jin Chang Qing. Hydrostaticity of Pressure Media in Diamond Anvil Cells. *Chinese Physics Letters*, 26(9):096202, 2009.
- [63] H. K. Mao, J. Xu, and P. M. Bell. Calibration of the ruby pressure gauge to 800 kbar under quasi-hydrostatic conditions. *Journal of Geophysical Research: Solid Earth*, 91(B5):4673–4676, 1986.
- [64] C. Pfleiderer, D. Reznik, L. Pintschovius, H. v. Lohneysen, M. Garst, and A. Rosch. Partial order in the non-Fermi-liquid phase of MnSi. *Nature*, 427:227–231, 2004.
- [65] M. Uhlarz, C. Pfleiderer, and S. M. Hayden. Quantum Phase Transitions in the Itinerant Ferromagnet ZrZn_2 . *Phys. Rev. Lett.*, 93:256404, Dec 2004.
- [66] D. Belitz, T. R. Kirkpatrick, and Jorg Rollbuhler. Tricritical Behavior in Itinerant Quantum Ferromagnets. *Phys. Rev. Lett.*, 94:247205, Jun 2005.
- [67] E. A. Yelland, J. M. Barraclough, W. Wang, K. V. Kamenev, and A. D. Huxley. High-field superconductivity at an electronic topological transition in URhGe. *Nature Physics*, 7:890C894, 2011.
- [68] D Aoki, A Huxley, Daniel Braithwaite Eric Ressouche and, J Flouquet, J-P Brison, E Lhotel, and C Paulsen. Coexistence of superconductivity and ferromagnetism in URhGe. *Nature*, 413:613–616, 2001.
- [69] C Krellner, S Lausberg, A Steppke, M Brando, L Pedrero, H Pfau, S Tenc, H Rosner, F Steglich, and C Geibel. Ferromagnetic quantum criticality in the quasi-one-dimensional heavy fermion metal YbNi_4P_2 . *New Journal of Physics*, 13(10):103014, 2011.
- [70] A Steppke, R Kchler, S Lausberg, E Lengyel, L Steinke, R Borth, T Lhmann, C Krellner, M Nicklas, C Geibel, F Steglich, and M Brando. Ferromagnetic Quantum Critical Point in the Heavy-Fermion Metal $\text{YbNi}_4(\text{P}_{1-x}\text{As}_x)_2$. *Science*, 339(6122):933–936, 2013.
- [71] George Gruner. *Density Waves in Solids*. Westview Press, 2000.
- [72] N. D. Mermin and H. Wagner. Absence of Ferromagnetism or Antiferromagnetism in One- or Two-Dimensional Isotropic Heisenberg Models. *Phys. Rev. Lett.*, 17:1133–1136, Nov 1966.
- [73] G. R. Stewart. Non-Fermi-liquid behavior in d- and f-electron metals. *Rev. Mod. Phys.*, 73:797–855, Oct 2001.

- [74] A Thamizhavel, T Takeuchi, T Okubo, M Yamada, R Asai, S Kirita, A Galatanu, E Yamamoto, T Ebihara, Y Inada, R Settai, and Y Onuki. Anisotropic electrical and magnetic properties of CeTSb₂ (T=Cu, Au, and Ni) single crystals. *Phys. Rev. B*, 68:054427, Aug 2003.
- [75] O. Sologub, H. Noel, A. Leithe Jasper, P. Rogl, and O. I. Bodak. Ternary Compounds REAgSb₂, RE = Y, La, Ce, Pr, Nd, Sm, Gd, Tb, Dy, Ho, Er, Tm: Magnetism and Crystal Structure. *J. Sol. St. Chem.*, 115(2):441 – 446, 1995.
- [76] S Araki, N Metoki, A Galatanu, E Yamamoto, A Thamizhavel, and Y Onuki. Crystal structure, magnetic ordering, and magnetic excitation in the 4f-localized ferromagnet CeAgSb₂. *Phys. Rev. B*, 68:024408, Jul 2003.
- [77] E. Jobilong, J. S. Brooks, E. S. Choi, H. Lee, and Z. Fisk. Magnetization and electrical-transport investigation of the dense Kondo system CeAgSb₂. *Phys. Rev. B*, 72(10):104428, Sep 2005.
- [78] T Takeuchi et al. Anisotropic, thermal, and magnetic properties of CeAgSb₂: Explanation via a crystalline electric field scheme. *Phys. Rev. B*, 67:064403, Feb 2003.
- [79] Y. Inada et al. An unusual hollow cylindrical Fermi surface of a quasi-two-dimensional compound CeAgSb₂. *Phil. Mag. B*, 82:1867–1892, 2002.
- [80] R Prozorov, M D. Vannette, G D. Samolyuk, S A. Law, S L. Bud’ko, and P C. Canfield. Contactless measurements of Shubnikov-de Haas oscillations in the magnetically ordered state of CeAgSb₂ and SmAgSb₂ single crystals. *Phys. Rev. B*, 75:014413, Jan 2007.
- [81] E D Mun, S L Budko, and P C Canfield. Thermoelectric power of RAgSb₂ (R = Y, La, Ce, and Dy) in zero and applied magnetic fields. *Journal of Physics: Condensed Matter*, 23(47):476001, 2011.
- [82] K. D. Myers, S. L. Bud’ko, I. R. Fisher, Z. Islam, H. Kleinke, A. H. Lacerda, and P. C. Canfield. Systematic study of anisotropic transport and magnetic properties of RAgSb₂ (R=Y, La-Nd, Sm, Gd-Tm). *J. Mag. Mag. Mat.*, 205(1):27 – 52, 1999.
- [83] P W Anderson. *Basic Notions of Condensed Matter Physics*. The Benjamin/Cummings Publishing Company, 1984.
- [84] V. A. Sidorov et al. Magnetic phase diagram of the ferromagnetic Kondo-lattice compound CeAgSb₂ up to 80 kbar. *Phys. Rev. B*, 67(22):224419, Jun 2003.

- [85] M J Thornton, J G M Armitage, G J Tomka, P C Riedi, R H Mitchell, M Houshiar, D T Adroja, B D Rainford, and D Fort. Low-temperature thermal and high-pressure studies of CePd and CeAgSb₂. *J. Phys. Cond. Mat.*, 10(42):9485, 1998.
- [86] M Nakashima, S Kirita, R Asai, T C Kobayashi, T Okubo, M Yamada, A Thamizhavel, Y Inada, R Settai, A Galatanu, E Yamamoto, T Ebihara, and Y Onuki. Huge residual resistivity in the quantum critical region of CeAgSb₂. *Journal of Physics: Condensed Matter*, 15(4):L111, 2003.
- [87] A.M. Strydom et al. Field-dependent tuning of the ferromagnetic ordering in CeAgSb₂. *J. Mag. Mag. Mat.*, 320(14):e453 – e456, 2008.
- [88] M. A. Ruderman and C. Kittel. Indirect Exchange Coupling of Nuclear Magnetic Moments by Conduction Electrons. *Phys. Rev.*, 96:99–102, Oct 1954.
- [89] N Ashcroft and D Mermin. *Solid State Physics*. Brooks/Cole, 1976.
- [90] S. Seo et al. Pressure effects on the heavy-fermion antiferromagnet CeAuSb₂. *Phys. Rev. B*, 85:205145, 2012.
- [91] K.-A. Lorenzer, A. M. Strydom, A. Thamizhavel, and S. Paschen. Temperature-field phase diagram of quantum critical CeAuSb₂. *physica status solidi (b)*, 250(3):464–467, 2013.
- [92] L. Balicas, S. Nakatsuji, H. Lee, P. Schlottmann, T. P. Murphy, and Z. Fisk. Magnetic field-tuned quantum critical point in CeAuSb₂. *Phys. Rev. B*, 72:064422, Aug 2005.
- [93] Zhuo Feng. *Sample Growth and High Pressure Studies of Novel Strongly Correlated Systems*. PhD thesis, University of Cambridge, 2012.
- [94] N. H. Andersen and H. Smith. Electron-magnon interaction and the electrical resistivity of Tb. *Phys. Rev. B*, 19:384–387, January 1979.
- [95] A Arrott. Criterion for Ferromagnetism from Observations of Magnetic Isotherms. *Phys. Rev.*, 108:1394–1396, Dec 1957.
- [96] D. Vollhardt. Characteristic Crossing Points in Specific Heat Curves of Correlated Systems. *Phys. Rev. Lett.*, 78:1307–1310, Feb 1997.
- [97] M. Greger, M. Kollar, and D. Vollhardt. Isosbestic points: How a narrow crossing region of curves determines their leading parameter dependence. *Phys. Rev. B*, 87:195140, May 2013.

- [98] H G Schlager et al. Magnetic ordering in $\text{CeCu}_{6-x}\text{Au}_x$ single crystals: Thermodynamic and transport properties. *J. Low Temp. Phys.*, 90:180–203, 1993.
- [99] G. E. Brodale, R. A. Fisher, Norman E. Phillips, and J. Floquet. Pressure dependence of the low-temperature specific heat of the heavy-fermion compound CeAl_3 . *Phys. Rev. Lett.*, 56:390–393, Jan 1986.
- [100] A. Bauer, M. Garst, and C. Pfleiderer. Specific Heat of the Skyrmion Lattice Phase and Field-Induced Tricritical Point in MnSi . *Phys. Rev. Lett.*, 110:177207, Apr 2013.
- [101] P. Payet Burin and C. Pfleiderer. Voltage controlled current source to avoid common mode interferences. *Review of Scientific Instruments*, 67(11):4023–4024, 1996.
- [102] Sandor Caplan and Gerald Chanin. Critical-Field Study of Superconducting Aluminum. *Phys. Rev.*, 138:A1428–A1433, May 1965.
- [103] G. V. Lecomte, M. Karnezos, and S. A. Friedberg. The uniaxial ferromagnet $\text{NiZrF}_6 \cdot 6\text{H}_2\text{O}$ in a transverse field. *Journal of Applied Physics*, 52(3):1935–1937, 1981.
- [104] S. Doniach. The Kondo lattice and weak antiferromagnetism. *Physica B+C*, 91(0):231 – 234, 1977.
- [105] C. Pfleiderer, G. J. McMullan, S. R. Julian, and G. G. Lonzarich. Magnetic quantum phase transition in MnSi under hydrostatic pressure. *Phys. Rev. B*, 55:8330–8338, Apr 1997.
- [106] T Liang, S.M. Koohpayeh, J. W. Krizan, T. M. McQueen, R. J. Cava, and N. P. Ong. Heat capacity anomaly at the quantum critical point of the Transverse Ising Magnet CoNb_2O_6 . arXiv:1405.4551.
- [107] S Ran, S L. Bud’ko, and P C. Canfield. Effects of substitution on low-temperature physical properties of LuFe_2Ge_2 . *Philosophical Magazine*, 91(34):4388–4400, 2011.
- [108] Y Kamihara, H Hiramatsu, M Hirano, R Kawamura, H Yanagi, T Kamiya, and H Hosono. Iron-Based Layered Superconductor? LaOFeP . *Journal of the American Chemical Society*, 128(31):10012–10013, 2006. PMID: 16881620.
- [109] I Mazin. Superconductivity gets a boost. *Nature*, 464:183–186, 2010.

- [110] T Moriya and K Ueda. Antiferromagnetic spin fluctuation and superconductivity. *Reports on Progress in Physics*, 66(8):1299, 2003.
- [111] J. Ferstl, H. Rosner, and C. Geibel. Evidence for fluctuating Fe-moments in RFe_2Ge_2 . *Physica B: Condensed Matter*, 378-380(0):744 – 745, 2006. Proceedings of the International Conference on Strongly Correlated Electron Systems {SCES} 2005 Proceedings of the International Conference on Strongly Correlated Electron Systems.
- [112] T Fujiwara, N Aso, H Yamamoto, M Hedo, Y Saiga, M Nishi, Y Uwatoko, and K Hirota. Pressure Effect on Magnetic Short Range Ordering of LuFe_2Ge_2 . *Journal of the Physical Society of Japan*, 76(Suppl.A):60–61, 2007.
- [113] M.A. Avila, S.L. Bud’ko, and P.C. Canfield. Anisotropic magnetization, specific heat and resistivity of RFe_2Ge_2 single crystals. *Journal of Magnetism and Magnetic Materials*, 270(12):51–76, 2004.
- [114] Peter Mohn. *Magnetism in the Solid State*. Springer, 2002.
- [115] H. Fukazawa, T. Saito, Y. Yamada, K. Kondo, M. Hirano, Y. Kohori, K. Kuga, A. Sakai, Y. Matsumoto, S. Nakatsuji, K. Kihou, A. Iyo, C. H. Lee, and H. Eisaki. NMR/NQR and Specific Heat Studies of Iron Pnictide Superconductor KFe_2As_2 . *Journal of the Physical Society of Japan*, 80(Suppl.A):SA118, 2011.
- [116] A Subedi. Unconventional sign-changing superconductivity near quantum criticality in YFe_2Ge_2 . *Phys. Rev. B*, 89:024504, Jan 2014.
- [117] Y. Zou, Z. Feng, P. W. Logg, J. Chen, G. I. Lampronti, and F. M. Grosche. Fermi liquid breakdown and evidence for superconductivity in YFe_2Ge_2 .
- [118] T Samuely, P Szab, Z Pribulov, N H Sung, B K Cho, T Klein, V Cambel, J G Rodrigo, and P Samuely. Type-II superconductivity in SrPd_2Ge_2 . *Superconductor Science and Technology*, 26(1):015010, 2013.
- [119] N. H. Sung, Jong-Soo Rhyee, and B. K. Cho. Superconductivity and anomalous transport in SrPd_2Ge_2 single crystals. *Phys. Rev. B*, 83:094511, Mar 2011.
- [120] H.C. Ku, I.A. Chen, C.H. Huang, C.W. Chen, Y.B. You, M.F. Tai, and Y.Y. Hsu. New superconductor SrPt_2Ge_2 with $T_c=10.2$ K. *Physica C: Superconductivity*, 493(0):93 – 95, 2013. New3SC-9.

- [121] L Shlyk, K K Wolff, M Bischoff, E Rose, Th Schleid, and R Niewa. Crystal structure and superconducting properties of hole-doped $\text{Ca}_{0.89}\text{Na}_{0.11}\text{FFeAs}$ single crystals. *Superconductor Science and Technology*, 27(4):044011, 2014.
- [122] M Xue, Cao T, Wang D, Wu Y, Yang H, Dong X, He J, Li F, and Chen G F. Superconductivity above 30 K in alkali-metal-doped hydrocarbon. *Scientific Reports*, 2:389, 2012.
- [123] Amish G. Joshi, C.G.S. Pillai, P. Raj, and S.K. Malik. Magnetization studies on superconducting MgB_2 c lower and upper critical fields and critical current density. *Solid State Communications*, 118(9):445 – 448, 2001.
- [124] O. M. Froehlich, A. Beck, R. Gross, H. Sato, and M. Naito. In-plane penetration depth of high-temperature superconductors with single and double CuO layers. *EPL (Europhysics Letters)*, 36(6):467, 1996.
- [125] John R. Clem and Zhidong Hao. Theory for the hysteretic properties of the low-field dc magnetization in type-II superconductors. *Phys. Rev. B*, 48:13774–13783, Nov 1993.
- [126] W. Anukool, S. Barakat, C. Panagopoulos, and J. R. Cooper. Effect of hole doping on the London penetration depth in $\text{Bi}_{2.15}\text{Sr}_{1.85}\text{CaCu}_2\text{O}_{8+\delta}$ and $\text{Bi}_{2.1}\text{Sr}_{1.9}\text{Ca}_{0.85}\text{Y}_{0.15}\text{Cu}_2\text{O}_{8+\delta}$. *Phys. Rev. B*, 80:024516, Jul 2009.
- [127] Fritz London. *Superfluids*. John Wiley & Sons, 1950.
- [128] T. P. Orlando, E. J. McNiff, S. Foner, and M. R. Beasley. Critical fields, Pauli paramagnetic limiting, and material parameters of Nb_3Sn and V_3Si . *Phys. Rev. B*, 19:4545–4561, May 1979.
- [129] P.W. Anderson. Theory of dirty superconductors. *Journal of Physics and Chemistry of Solids*, 11(1C2):26 – 30, 1959.
- [130] H Q Yuan, F M Grosche, M Deppe, C Geibel, G Sparn, and F Steglich. Effect of impurity scattering on the superconductivity of CeCu_2Si_2 . *New Journal of Physics*, 6(1):132, 2004.
- [131] J. Crangle and G. M. Goodman. The Magnetization of Pure Iron and Nickel. *Proceedings of the Royal Society of London. A. Mathematical and Physical Sciences*, 321(1547):477–491, 1971.
- [132] C.D. Bredl, H. Spille, U. Rauchschalbe, W. Lieke, F. Steglich, G. Cordier, W. Assmus, M. Herrmann, and J. Aarts. Gapless superconductivity and variation of T_c in the heavy-fermion system CeCu_2Si_2 . *Journal of Magnetism and Magnetic Materials*, 31C34, Part 1(0):373 – 376, 1983.

- [133] J J Hamlin, R E Baumbach, D A Zocco, T A Sayles, and M B Maple. Superconductivity in single crystals of LaFePO. *Journal of Physics: Condensed Matter*, 20(36):365220, 2008.
- [134] Y J Song, J S Ghim, J Hyun Yoon, K J Lee, M H Jung, H-S Ji, J H Shim, Y Bang, and Y S Kwon. Small anisotropy of the lower critical field and the s-wave two-gap feature in single-crystal LiFeAs. *EPL (Europhysics Letters)*, MISClifeas(5):57008, 2011.
- [135] V K Anand, H Kim, and M A Tanatar. Superconductivity and Physical Properties of CaPd₂Ge₂Ge₂ Single Crystals.
- [136] P. Burger, F. Hardy, D. Aoki, A. E. Böhmer, R. Eder, R. Heid, T. Wolf, P. Schweiss, R. Fromknecht, M. J. Jackson, C. Paulsen, and C. Meingast. Strong Pauli-limiting behavior of H_{c2} and uniaxial pressure dependencies in KFe₂As₂. *Phys. Rev. B*, 88:014517, Jul 2013.
- [137] U. Rauchschwalbe, W. Lieke, C. D. Bredl, F. Steglich, J. Aarts, K. M. Martini, and A. C. Mota. Critical Fields of the "Heavy-Fermion" Superconductor CeCu₂Si₂. *Phys. Rev. Lett.*, 49:1448–1451, Nov 1982.
- [138] N Kurita, K Kitagawa, K Matsubayashi, A Kismarahardja, E S Choi, J S Brooks, Y Uwatoko, S Uji, and T Terashima. Upper Critical Field of the Stoichiometric Fe-based Superconductor LiFeAs. *Journal of Physics: Conference Series*, 391(1):012133, 2012.
- [139] H Lei, R Hu, and C. Petrovic. Critical fields, thermally activated transport, and critical current density of β -FeSe single crystals. *Phys. Rev. B*, 84:014520, Jul 2011.
- [140] Martin T Dove. *Structure and Dynamics: An atomic view of materials*. Oxford University Press, 2003.
- [141] D. A. Tompsett. Electronic structure and phonon instabilities in the vicinity of the quantum phase transition and superconductivity of (Ca,Sr)₃Ir₄Sn₁₃. *Phys. Rev. B*, 89:075117, Feb 2014.
- [142] M Gamza, W Schnelle, Alebarski, U Burkhardt, R Gumeniuk, and H Rosner. Electronic structure and thermodynamic properties of Ce₃Rh₄Sn₁₃ and La₃Rh₄Sn₁₃. *Journal of Physics: Condensed Matter*, 20(39):395208, 2008.
- [143] A.D. Christianson, J.S. Gardner, H.J. Kang, J.-H. Chung, S. Bobev, J.L. Sarrao, and J.M. Lawrence. Low temperature behavior of the heavy fermion Ce₃Co₄Sn₁₃. *Journal of Magnetism and Magnetic Materials*, 310(2, Part

- 1):266 – 267, 2007. Proceedings of the 17th International Conference on Magnetism The International Conference on Magnetism.
- [144] A M Strydom. Thermal and transport properties of the cubic semimetal $\text{Y}_3\text{Ir}_4\text{Ge}_3$: on the metallic border of thermoelectric merit. *Journal of Physics: Condensed Matter*, 19(38):386205, 2007.
- [145] G.P. Espinosa. Crystal growth and crystal-chemical investigation of systems containing new superconducting and/or magnetic ternary stannides. *Materials Research Bulletin*, 15(6):791 – 798, 1980.
- [146] J Yang, B Chen, C Michioka, and K Yoshimura. Coexistence of Superconductivity and Ferromagnetic Spin-Fluctuation in $\text{Ca}_3\text{Ir}_4\text{Sn}_{13}$ Single Crystal. *Journal of the Physical Society of Japan*, 79(11):113705, 2010.
- [147] N. Kase, H. Hayamizu, and J. Akimitsu. Superconducting state in the ternary stannide superconductors $\text{R}_3\text{T}_4\text{Sn}_{13}$ ($\text{R} = \text{La}, \text{Sr}$; $\text{T} = \text{Rh}, \text{Ir}$) with a quaskutterudite structure. *Phys. Rev. B*, 83:184509, May 2011.
- [148] Lina E. Klintberg. *Fermi surface and lattice instabilities and their consequences for superconductivity*. PhD thesis, University of Cambridge, 2012.
- [149] Kefeng Wang and C. Petrovic. $\text{Ca}_3\text{Ir}_4\text{Sn}_{13}$: A weakly correlated nodeless superconductor. *Phys. Rev. B*, 86:024522, Jul 2012.
- [150] Martin Schreyer and Thomas F. Fassler. $\text{Ca}_7\text{Co}_8\text{Sn}_{25}$ and $\text{Ca}_3\text{Co}_4\text{Sn}_{13}$ revisited. *Solid State Sciences*, 8(7):793 – 797, 2006. Special issue in honour of H.G von Schnering.
- [151] C. V. Tomy, G. Balakrishnan, and D. McK. Paul. Observation of the peak effect in the superconductor $\text{Ca}_3\text{Rh}_4\text{Sn}_{13}$. *Phys. Rev. B*, 56:8346–8350, Oct 1997.
- [152] S. Sarkar, D. Pal, S. S. Banerjee, S. Ramakrishnan, A. K. Grover, C. V. Tomy, G. Ravikumar, P. K. Mishra, V. C. Sahni, G. Balakrishnan, D. McK. Paul, and S. Bhattacharya. Stepwise amorphization of the flux-line lattice in $\text{Ca}_3\text{Rh}_4\text{Sn}_{13}$: A peak-effect study. *Phys. Rev. B*, 61:12394–12403, May 2000.
- [153] B Pippard. A possible mechanism for the peak effect in type II superconductors. *Philosophical Magazine*, 19(158):217–220, 1969.
- [154] P K Biswas, A Amato, R Khasanov, H Luetkens, Kefeng Wang, C Petrovic, R M Cook, M R Lees, and E Morenzoni. Superconducting and magnetic properties of $\text{Sr}_3\text{Ir}_4\text{Sn}_{13}$. arXiv:1403.6379v1.

-
- [155] Anupam, Paulose P L, Ramakrishnan S, and Hossain Z. Doping dependent evolution of magnetism and superconductivity in $\text{Eu}_{1-x}\text{K}_x\text{Fe}_2\text{As}_2$ ($x = 0$ to 1) and temperature dependence of the lower critical field H_{c1} . *Journal of Physics*, 23, 2011.
- [156] Charles P. Bean. Magnetization of High-Field Superconductors. *Rev. Mod. Phys.*, 36:31–39, Jan 1964.
- [157] Y. B. Kim, C. F. Hempstead, and A. R. Strnad. Magnetization and Critical Supercurrents. *Phys. Rev.*, 129:528–535, Jan 1963.
- [158] D.-X. Chen, A. Sanchez, J. Nogues, and J. S. Muñoz. Beans, Kims, and exponential critical-state models for high- T_c superconductors. *Phys. Rev. B*, 41:9510–9512, May 1990.